INFORMATION TO USERS

This manuscript has been reproduced from the microfilm master. UMI films the text directly from the original or copy submitted. Thus, some thesis and dissertation copies are in typewriter face, while others may be from any type of computer printer.

The quality of this reproduction is dependent upon the quality of the copy submitted. Broken or indistinct print, colored or poor quality illustrations and photographs, print bleedthrough, substandard margins, and improper alignment can adversely affect reproduction.

In the unlikely event that the author did not send UMI a complete manuscript and there are missing pages, these will be noted. Also, if unauthorized copyright material had to be removed, a note will indicate the deletion.

Oversize materials (e.g., maps, drawings, charts) are reproduced by sectioning the original, beginning at the upper left-hand corner and continuing from left to right in equal sections with small overlaps. Each original is also photographed in one exposure and is included in reduced form at the back of the book.

Photographs included in the original manuscript have been reproduced xerographically in this copy. Higher quality 6" x 9" black and white photographic prints are available for any photographs or illustrations appearing in this copy for an additional charge. Contact UMI directly to order.

UMI®

Bell & Howell Information and Learning
300 North Zeeb Road, Ann Arbor, MI 48106-1346 USA
800-521-0600

MICROSCOPIC APPROACH TO CLOUD DROPLET GROWTH BY CONDENSATION

By

Paul Vaillancourt

SUBMITTED IN PARTIAL FULFILLMENT OF THE
REQUIREMENTS FOR THE DEGREE OF
DOCTOR OF PHILOSOPHY
AT
McGILL UNIVERSITY
MONTREAL, QUEBEC
FEBRUARY, 1998

Abstract

Traditionally, the diffusional growth of a cloud droplet population is calculated using values of the environmental conditions that represent averages over large volumes, the so called *macroscopic* conditions (Srivastava 1989). However, it is apparent that the growth rate of an individual droplet is a function of the temperature and the vapor pressure in its immediate environment. These quantities vary from droplet to droplet and with time in a turbulent medium such as a cumulus cloud. In most theoretical and numerical studies of clouds, the hypothesis is made that these variations are unimportant when calculating the growth of an ensemble of droplets. The objective of this work is to determine the validity of this hypothesis. In order to do so we use a 3D turbulence model coupled with a cloud droplet growth model which solves for the trajectories and growth of several tens of thousands of individual droplets as a function of their local conditions (*microscopic* approach).

A series of experiments with various initial size distributions were conducted using no turbulent flow conditions or one of three turbulent flows with increasing eddy dissipation rate. The results show that in the absence of any turbulent flow or sedimentation of droplets , the non-uniform distribution of cloud droplets in space results in significant variance of the distribution of the supersaturation perturbation over all droplets (DSP) and the distribution of the degree of growth(DDG), defined as the Lagrangian integral of the supersaturation perturbation along each droplet's trajectory. The variance of the DDG is directly responsible for the broadening of the *microscopic* size distribution relative to the *macroscopic* size distribution. However, in the presence of turbulence and sedimentation of droplets, the variance of the DSP is significantly reduced. Furthermore, the average, over all droplets, of the decorrelation time of the supersaturation perturbation decreases as a function of increasing level of turbulence. Consequently, the variance of the DDG is significantly reduced compared to the no turbulence and no sedimentation experiments and furthermore,

it decreases as a function of increasing level of turbulence.

We have found that for the typical levels of turbulence found in adiabatic cloud cores, the spatial distribution of the larger cloud droplets can significantly deviate from a Poisson distribution. The increasing preferential concentration as a function of increasing level of turbulence does contribute to an increase in the DSP as a function of increasing level of turbulence. However, the DDG decreases as a function of increasing level of turbulence.

These results are at odds with those in the idealized studies of Pinsky et al. (1996) and Shaw et al. (1998). These authors specified and maintained very significant preferential concentration artificially rather than obtaining it by solving explicitly the trajectories of the droplets.

Comparison of our results with the observations of Brenguier and Chaumat (1996) made in adiabatic cloud cores lead us to the conclusion that the *microscopic* approach, even under the most favorable condition of no turbulence, produces too little broadening to explain the observations.

Résumé

Traditionnellement, la croissance par diffusion de vapeur d'eau d'une population de gouttelettes se calcule en utilisant les valeurs des variables environnementales, que l'on nomme conditions macroscopiques (Srivastava 1989) et qui représentent des moyennes mesurées à partir d'importants volumes. Cependant, il appert que le taux de croissance de chaque gouttelette prise individuellement est fonction de la température et de la pression de vapeur dans son environnement immédiat. Ces facteurs varient d'une gouttelette à l'autre ainsi qu'en fonction du temps dans un milieu turbulent comme un cumulus. Dans la plupart des études théoriques et numériques des nuages on émet l'hypothèse que ces variations ne sont pas importantes dans le calcul de la croissance d'un ensemble de gouttelettes. Ce travail a pour objectif de vérifier la validité de cette hypothèse. Pour ce faire, nous avons utilisé un modèle de turbulence en trois dimensions jumelé à un modèle de croissance de gouttelettes qui tient compte des trajectoires et de la croissance de plusieurs dizaines de milliers de gouttelettes individuelles, en fonction de leurs conditions environnementales immédiates.

Nous avons mené une série d'expériences, comportant des distributions initiales de taille de gouttelette variées, en utilisant soit des conditions sans turbulence ou soit un de trois niveaux de turbulence. Les résultats nous montrent qu'en l'absence de toute turbulence ou de sédimentation de gouttelettes, la distribution non uniforme des gouttelettes dans l'espace se traduit par une variance significative dans la distribution (sur l'ensemble des gouttelettes) de la perturbation sursaturée (DPS) et la distribution du degré de croissance (DDC). Cette dernière distribution est le résultat de l'intégrale lagrangienne de la perturbation sursaturée le long de la trajectoire de chaque gouttelette. L'élargissement de la distribution de la taille par rapport à la distribution de la taille dans un cadre macroscopique est directement dépendante de la variance du DDC. Cependant, en présence de la turbulence et de la sédimentation des

gouttelettes, la variance du DPS diminue de façon significative. De plus, sur toutes les gouttelettes, le temps moyen de décorrelation de la perturbation sursaturée décroît en fonction de l'augmentation du niveau de turbulence. En conséquence, la variance du DDC diminue sensiblement en comparaison des expériences sans turbulence et sans sédimentation et, qui plus est, elle diminue aussi en fonction de l'augmentation du niveau de turbulence.

Nous avons découvert que, pour des niveaux types de turbulence mesurés au centre adiabatique des nuages, la distribution spatiale des plus grosses gouttelettes peut dévier sensiblement d'une distribution de Poisson. Le fait que la concentration préférentielle augmente en fonction de l'augmentation du niveau de turbulence accroît le DPS mais n'accroît pas le DDC.

Nos résultats contredisent ceux de Pinsky et al. (1996) et Shaw et al. (1998). Dans ces études, un forte concentration préférentielle est imposée et maintenue artificiellement, tandis que dans notre approche la concentration préférentielle résulte du calcul explicite des trajectoires des gouttelettes.

En comparant nos résultats avec les observations de Brenguier et Chaumat (1996) réalisées au centre adiabatique de nuages , nous parvenons à la conclusion que l'approche microscopique, même sous les conditions les plus favorables en l'absence de turbulence et de sédimentation , produit trop peu d'élargissement pour expliquer leurs observations.

Statement of originality

The following points describe the unique and original aspects of this work.

1. A direct numerical simulation approach (DNS) is used in the context of cloud droplet growth.

2. Clustering (preferential concentration) is explicitly estimated, for sedimenting and non-sedimenting particles with Stokes numbers characteristic of cloud droplets in cumulus clouds with low to moderate turbulence. We found that:

   - significant clustering can occur for cloud droplets
   - sedimentation of the cloud droplets significantly reduces the magnitude of the clustering

3. A *microscopic* model to calculate the growth and trajectories of a large number of cloud droplets as a function of conditions in their individual ambient environments is developed. The *microscopic* approach to cloud droplet growth is explicitly tested. We found that:

   - preferential concentration of droplets and the cooling term due to the variability in vertical velocity have a positive effect on spectral broadening
   - sedimentation of droplets has a negative effect on spectral broadening
   - the decorrelation time for Lagrangian supersaturation perturbation is shown to decrease as a function of increasing level of turbulence.
   - only when turbulence and sedimentation is absent can the *microscopic* approach lead to non-negligible differences in terms of spectral broadening relative to the *macroscopic* approach.

- even in the absence of turbulence and sedimentation the maximum spectral broadening obtained in our numerical experiments is significantly smaller than the broadening observed in adiabatic cloud cores (Brenguier and Chaumat 1996).

Acknowledgments

I would like to thank my thesis supervisor Dr. M. K. Yau for his constant support and his patient guidance throughout this work. I would also like to thank Dr. W. W. Grabowski for suggesting this line of work and for enthusiastically supporting me through the numerous constructive discussions we had. Also, Dr. P. Bartello who provided the code for the turbulence model and precious insights on the field of turbulence in fluids. Dr J.-L. Brenguier's input on observations in real clouds was also very helpful. This research was supported by grants from the U.S. Office of Naval Research, the Natural Sciences and Engineering Research Council and the Atmospheric Environment Service of Canada.

J'aimerais également remercier tous mes collègues et amis qui ont rendu mon court séjour à l'Université McGill très agréable. Un merci tout spécial à Gilles A., Halldor B., Fred D., Ramon de E., Sylvain L., Daniel L., Guy P., Ekaterina R., Gavin S., Rob S., David S., Sylvia V., Werner W., Ayrton Z. et bien d'autres. Enfin, comment ne pas souligner l'apport essentiel de mes amis Louis Bruno du Tremblay et de Pierrot Charron dont l'humour et l'intelligence m'ont permis de passer à travers.

Finalement, un immense bisou à Catherine Beaudry pour tout.

Contents

List of Figures

List of Tables

Chapter 1

Introduction

In the past 40 years, much research has been directed toward determining the important processes in the evolution of the microphysical properties of clouds. A long-standing problem, prompted especially by the observations of Warner (1969), is that the observed size distributions of cloud droplets in cumulus clouds are relatively broad and often multimodal. In contrast, simple calculations of the diffusional growth of cloud droplets yield narrow and nearly monodispersed distributions. In these calculations, it is generally assumed that cloud droplets are embedded in an air parcel with uniform properties and it rises with a constant updraft speed. Thus all droplets are submitted to the same supersaturation. Since the rate of growth of the radius of a droplet varies inversely with its radius, the size distribution becomes narrower with time. This discrepancy between the observed size distributions and those resulting from simple parcel calculations implies that in real clouds all droplets are not submitted to the same supersaturation. More precisely, all droplets do not have the same Lagrangian integral of supersaturation.

Manton (1979) and Cooper (1989) developed a statistical approach to predict the evolution of the size distribution of cloud droplets from a knowledge of the variance of the Lagrangian integral of the supersaturation averaged over an ensemble of cloud

droplets. By approximating the supersaturation by the quasi-stationary supersaturation, they were able to express the variance as a function of the variability of the integral radius and the correlation between the integral radius and the vertical wind. Politovich (1993) tested this approach and found that the predicted and observed dispersions in the size spectra agreed well in diluted regions of the clouds. However, it should be pointed out that the relaxation time scale for quasi-steady supersaturation is of the order of a few seconds with corresponding spatial scales on the order of a few tens of centimeters in a turbulent medium (Cooper 1989). The approach of Manton and Cooper therefore neglects the contribution of scales smaller than a few tens of centimeters to the variability of the supersaturation. Despite this weakness, the evidence so far accumulated suggests strongly that in diluted regions of cumulus clouds, mixing between cloudy and non-cloudy air can explain the complex nature of the observed size distributions (Cooper 1991).

However, observations have also shown that even in adiabatic cloud regions which have not been affected by mixing, the size distribution are also broader than expected. In particular, Brenguier and Chaumat (1996) analyzed measurements made by a high resolution Fast Forward Scattering Spectrometer Probe (Brenguier et al. 1998) in adiabatic cloud cores and showed that even the narrowest spectra measured are still broader than those obtained from simple diffusional growth calculations. By comparing the narrowest spectra sampled at various altitudes against a reference level spectrum, they were able to infer the probability distribution of the Lagrangian integral of the supersaturation necessary to explain the evolution of the observed spectra. Thus it is clear that mixing is not sufficient to explain all observed size distributions and other processes contributing to the variability in supersaturation must be in operation.

Srivastava (1989) suggested one possible mechanism. He hypothesized that both the random spatial distribution of droplets and the variations in the vertical air

velocity could cause non-negligible deviation of the supersaturation experienced by individual droplets (*microscopic* supersaturation) from the supersaturation calculated for cloud parcels containing a large number of droplets (*macroscopic* supersaturation). He pointed out that in most theoretical and numerical studies of clouds, it is implicitly assumed that droplet to droplet variability is not important in calculating the growth of an ensemble of droplets. Srivastava viewed this assumption justifiable only if it can be shown that molecular diffusion or some other processes can result in negligible differences between the *microscopic* and *macroscopic* supersaturations. By assuming that the spatial distribution of the droplets is described by the Poisson distribution, he derived analytical estimates for the variance in the *microscopic* supersaturation and concluded that the variance can contribute significantly to the width of the droplet size distributions. However, his conclusion must be viewed as tentative because two important effects, that of turbulence and that of sedimentation, were not taken into account.

The importance of turbulence and sedimentation arises from the fact that somewhat surprisingly, the average distance between cloud droplets is of the same order of magnitude as the Kolmogorov length scale. Thus the behavior of the droplets would be affected by the fine scale structure associated with turbulence in the range of the Kolmogorov length scale. Furthermore, as will be shown later, the eddy turnover time associated with the Kolmogorov length scale is of the same order of magnitude as the sedimentation time scale of the droplets traversing the Kolmogorov length scale. Therefore, dynamics and sedimentation effects are expected to play a critical role in affecting the behavior of the drops and in influencing the ambient conditions within which individual droplets grow.

Another process which has not been taken into consideration is the inertia effect. Recent numerical simulations and laboratory experiments in mechanical engineering indicated that particles in a turbulent fluid, because of their finite inertia, tend to

diverge from regions of high vorticity (coherent vortices for example) and converge preferentially in regions of low vorticity. As a result, regions with much higher and lower concentrations than predicted from a random Poisson spatial distribution can develop. As this process can affect the local concentration of cloud droplets, its possible role in affecting the size distribution of cloud droplets should be explored.

The focus of this thesis is to provide answer to the following question:

> Can non-uniformity in the spatial distribution of the size and position of droplets and/or variable vertical velocity in a turbulent medium contribute to the broadening of the droplet size distributions?

Since it is extremely difficult to resolve this question analytically or from observations, a numerical model will be used. The strategy is the following. We simultaneously solve two sets of equations. The *macroscopic* equations and the *microscopic* equations. The *macroscopic* set of equations correspond to a simple Lagrangian parcel experiment in which all droplets are exposed to the same supersaturation. The *microscopic* set of equations explicitly solves for the growth and trajectory of each individual droplet as a function of the conditions in their individual ambient environments. In the *microscopic* approach each droplet is therefore exposed to a different supersaturation. There are several factors responsible for droplet to droplet variations in supersaturation. Among them are the spatial distribution of the position and the size of the droplets, the spatial variability in the scalar fields caused by the growing droplets, molecular diffusion and by turbulence and the sedimentation of the droplets through these fields. The role of these various factors in causing differences between the *microscopic* and *macroscopic* approaches in terms of sizes of individual droplets and in terms of the width of the size distribution would be examined. To simulate the turbulent flow we use a direct numerical simulation (DNS) approach. Since our interest is in the growth of cloud droplets in the size range from 5 to $\approx 25\mu m$, growth by collision-coalescence, as well as the solute and curvature effects can all be neglected.

The thesis is structured in the following manner. In Chapter 2 we first review pertinent theoretical aspects of turbulent flows. Using these concepts, we characterize the observed turbulence in cumulus clouds. We then analyze the problem of the two-way interaction between cloud droplets and turbulent flows characteristic of cumulus clouds.

In Chapter 3 we perform a scale analysis of droplet growth by condensation in a turbulent flow. This scale analysis serves to justify the set of equations solved in this thesis as well as to shed light on the limitation of our simplifications. Furthermore, it guides us in the choice of appropriate experimental conditions. For example, we conclude from the scale analysis that in order that the gridpoint values of temperature and water vapor mixing ratio represent the ambient conditions of individual droplets, the size of the grid cells must be $\approx .1cm$. Furthermore, this gridsize is also necessary to resolve the turbulent flow. Consequently the size of the computational domain is of the order of $10cm$ and it contains several tens of thousands of droplets.

In Chapter 4 we describe the two sets of equations solved in this work, the *microscopic* and *macroscopic* equations. In Chapter 5 we describe the computational framework and the numerical methods used to solve the equations. We also present a formalism which will be used in the analysis of the results.

In Chapter 6 we present results from simple experiments with no turbulent flow. This framework is useful because it offers a simple context to interpret the effect of sedimentation and the sensitivity of spectral broadening to various initial conditions. These results are compared to the analytical estimates of Srivastava (1989). In Chapter 7 we first describe the three turbulent flows with varying eddy dissipation rates used for the experiments with cloud droplets. We then explore the subject of preferential concentration and its link to vorticity. Finally we present the results for the full experiments of cloud droplet growth in a turbulent flow and compare these results with the observations of Brenguier and Chaumat (1996).

In Chapter 8 we summarize the main results and present an answer to the central question posed in this thesis.

Chapter 2

Turbulent flow in cumulus clouds

Convection in cumulus clouds is forced by buoyancy. The convective updrafts may be influenced by the temperature stratification in the environment and by turbulence in regions where thermal gradients and/or shear render the flow unstable. The objective of this chapter is first to summarize the observations on the turbulent characteristics of cumulus clouds. This will be followed by a discussion of the scales at which in-cloud turbulence is compatible with the Kolmogorov theory of isotropic turbulence. Finally, we will explore the question of at what scales stratification may be an important factor in modifying the flow.

Contrary to most work in cloud physics, we are concerned here with the evolution of individual cloud droplets. From this perspective, the large body of work done on particle-laden turbulent flows in mechanical engineering becomes relevant. We will pay special attention on how droplets may influence the flow and how the flow may influence the spatial distribution of the droplets.

2.1 Turbulence: basic concepts and definitions

Turbulence develops in rotational flows. It arises from diffusion and stretching of vorticity which can be created in the flow by various means relating to either shear or thermal gradients. A turbulent flow, which exhibits complex chaotic spatial and temporal behaviour, can be described as a weakly correlated random field with strongly correlated yet highly localized structures that are largely responsible for intermittent effects (She et al. 1990, 1991). Gaussian statistics are associated with the random nature of turbulence while non-Gaussian intermittent behaviour (higher probability for high amplitude events in vorticity for example) is a signature of coherence. Kolmogorov (1941) proposed a phenomenological theory of the universal statistical properties of small scale turbulence in high Reynolds number flows. Even though this theory fails to describe intermittent effects, it gives a very good approximation to the turbulent energy spectrum in the inertial range. The energy spectrum (called Kolmogorov's spectrum) takes on the form:

$$E(k) = C_K \epsilon^{2/3} k^{-5/3}, \tag{2.1}$$

where C_K is a universal constant called the Kolmogorov constant. Numerous observations in the atmosphere (Champagne et al. 1977) , the ocean (Gargett et al. 1984) and in laboratory experiments (Gagne 1987) have shown that the structure of flows in the "small" scales agrees well with Kolmogorov's spectrum when the Reynolds number is sufficiently high.

Kolmogorov's spectrum is obtained from dimensional analysis by assuming that the energy spectrum, at wavenumbers greater than that at which the flow is forced and smaller than that at which viscous dissipation dominates the flow, depends only on ϵ, the eddy dissipation rate, and the wavenumber k. The parameter ϵ controls the energy flux in the inertial subrange, i.e. from the forcing scales down to k_d the Kolmogorov wavenumber, where viscous dissipation becomes important. The inverse

of k_d is the Kolmogorov length scale and is given by:

$$\eta = \left(\frac{\nu^3}{\epsilon}\right)^{1/4}. \tag{2.2}$$

Using this definition and the Kolmogorov spectrum it is possible to find a velocity scale and a time scale associated with this length scale:

$$v_\eta = (\epsilon\nu)^{1/4} \qquad \tau_\eta = \left(\frac{\nu}{\epsilon}\right)^{1/2}. \tag{2.3}$$

Let us recall the definition of some other characteristic quantities which will be used to describe the simulated flows. The integral scale, the length scale characteristic of the energy containing eddies, is defined as:

$$l_0 \sim \frac{u_0^3}{\epsilon} = \frac{(2E_T)^{3/2}}{2\nu D}. \tag{2.4}$$

where u_0 is the root mean square velocity, E_T is the total kinetic energy and D corresponds to the enstrophy which is the variance of the vorticity. From this length scale, the large-eddy turnover time scale can be defined as:

$$\tau_0 = \frac{l_0}{u_{rms}} \tag{2.5}$$

The Taylor microscale, the length scale characteristic of the mean spatial extension of the velocity gradients is defined as:

$$\lambda^2 \sim \frac{u_0^2\nu}{\epsilon} = \frac{E_T}{D}. \tag{2.6}$$

With these quantities one can define two Reynolds numbers: the integral-scale Reynolds number $R_l = l_0 u_0/\nu$ and the Taylor microscale Reynolds number $R_\lambda = \lambda u_0/\nu$.

There is no simple universal theory of the dynamics of coherent structures in three dimensions (3D). Numerical simulations have shown that these structures appear as regions of high intensity of vorticity organized in long tube-like structures that

generate velocity fields that spiral around them. Their width is typically of the order of the Kolmogorov length scale and they are sparsely distributed in space. Very little is known about their temporal evolution but by definition they are called coherent structures if their associated time scale is longer than the eddy turnover time associated with their width. These structures were first noticed in direct numerical simulations by Siggia (1981) at $R_\lambda \approx 100.$ and were further studied by others such as Kerr (1985), She et al. (1990) and Vincent and Meneguzzi (1991) for $R_\lambda \approx 48, 90,$ and 150 respectively.

2.2 Observations in cumulus clouds

We now consider the observed turbulent characteristics of cumulus clouds. Turbulence in clouds is thought to originate from the boundary layer and from instabilities that develop at the cloud-environment interface (Grabowski and Clark 1993). We will investigate to what degree and at which scale Kolmogorov's theory applies to the description of turbulence in clouds. Our investigation will guide us in choosing the parameters for our simulations of turbulent flows.

The most complete set of observations on the turbulent characteristics of cumulus clouds can be found in MacPherson and Isaac(1977), MacPherson(1979) and Weil et al.(1993). They reported that for most of the measurements, the $-5/3$ power law appears to be valid for scales up to about $100m$ for the three components of the wind velocity. Between 100 and $400m$, the energy spectra for the vertical component of the velocity shows a steeper slope. These authors speculate that the release of latent heat during condensation may produce turbulent eddies that fall preferentially within this wavelength range.

In general, the observations cited above indicate that at least for scales between

$15m$ (minimum wavelength at which measurements were made) and $100m$ the measured turbulence appears to be described well by Kolmogorov's theory. When all the scales, up to the size of the whole cloud, are considered, it was found that the variance of the vertical velocity is generally about 50% greater than the variance of the horizontal velocities. This finding is not too surprising since clouds are driven mainly by buoyancy forces and the cloud circulation as a whole is therefore not isotropic.

Eddy dissipation rates can be obtained by integrating (2.1) over the range of scales obeying the $-5/3$ power law (MacPherson and Isaac 1977; MacPherson 1979) or from measured pressure fluctuations (Weil et al. 1993). The above sources reported that ϵ may be quite variable inside a cloud, with the highest values generally found near the cloud top. The measured extreme values are ≈ 1 and $1000 cm^2 s^{-3}$. The median eddy dissipation rate associated with measurements mostly made near the cloud top in these three papers are respectively $288 cm^2 s^{-3}$, $165 cm^2 s^{-3}$ and $130 cm^2 s^{-3}$. MacPherson and Isaac(1977) did obtain some measurements at the cloud base and a few hundred meters below the cloud base. In these locations, the value for ϵ was smaller. The measured maximum is $90 cm^2 s^{-3}$ at the cloud base and the values range from 10 to $40 cm^2 s^{-3}$ below the cloud base. With regard to the cloud core, there is little data in the reported literature on the eddy dissipation rate. However, the core regions are located away from the cloud top and far removed from turbulence source regions like the cloud boundaries. It is reasonable to assume that the eddy dissipation rate should be much smaller than the averages found near the cloud top level and closer to values at or below the cloud base. Definitely more systematic observations are needed to validate this assumption.

For the observed range of eddy dissipation rate in cumulus clouds, we calculated the Kolmogorov length, time, and the velocity scales according to (2.2) and (2.3). The results are displayed in Table 2.1. The Kolmogorov length scale is of the order of millimeters, the velocity at that scale is of the order of cms^{-1} while the associated time

scale (eddy turnover time) varies over two order of magnitudes from one hundredth of a second to one second for the highest and lowest values of eddy dissipation rates. These characteristic scales will be useful for the scale analysis in the next chapter.

Energy dissipation rate $\epsilon(cm^2s^{-3})$	Kolmogorov length $\eta(cm)$	Kolmogorov time $\tau_\eta(sec)$	Kolmogorov velocity $v_\eta(cms^{-1})$
.1	.45	1.25	.35
1	.25	.4	.63
10	.14	.13	1.1
100	.08	.04	2.0
1000	.045	.01	3.5

Table 2.1: Characteristic Kolmogorov scales for eddy dissipation rates observed in cumulus clouds

2.3 Effects of stratification

It is known that density stratification influences the structure of turbulent flows. Stable stratification introduces wave-like characteristics (gravity waves) into the flow field. It also tends to enhance the growth of horizontal scales while inhibiting the growth of the vertical scales (Riley et al. 1981). The question arises as to what scales may be affected. As mentioned earlier, observations indicate that at least for the scales between $15m$ and $100m$, turbulence in cumulus clouds appears to be isotropic. For smaller scales, it is appropriate to examine the Osmidov scale (Lesieur 1990, page 340) defined as the scale at which the Froude number equals one. The Froude number measures the relative importance of inertial effects over stratification effects. The Osmidov scale is given by:

$$l_B = \left(\frac{\epsilon}{N^3}\right)^{1/2},$$

where N is the Brunt-Vaisala frequency. For scales $l \ll l_B$ stratification has a negligible effect on turbulence. Using a typical value of N of $1.2 \times 10^{-2}\ s^{-1}$ (Rogers and Yau 1989, page 32) and the range of observed values of ϵ, this scale turns out to vary from 7 to $200m$. Hence for the scales considered in this work, namely a few tens of centimeters, it can reasonably be assumed that stratification does not significantly modify the three dimensional nature of the flow. Our analysis is consistent with direct numerical simulation results of thermals rising in a stably stratified environment by Grabowski and Clark(1993). They showed that the perturbations which developed on the thermal interface evolved toward a flow structure possessing characteristics typically found in homogeneous isotropic turbulence.

2.4 Effects of the presence of droplets

We are concerned here with the possible modification of the properties of turbulence by the presence of droplets and the effect turbulence may have on the spatial distribution of droplets. Recent relevant work on these subjects regarding particles in turbulent flow in mechanical engineering are reviewed in Stock (1996), McLaughlin (1994) and Eaton and Fessler (1994).

2.4.1 Effects of particles on the flow

Particles like cloud droplets (size much smaller than the Kolmogorov length scale) may influence the flow either through the drag force (mechanical coupling) or through thermodynamic effect in the form of sources or sinks of latent heat and water vapor. In cloud models, these effects are generally included in the vertical momentum equation in the form of a buoyancy force which takes into account both thermal buoyancy and the liquid water mass loading.

We first concentrate on mechanical coupling. In clouds, cloud droplets interact

with the flow through relative velocity which arises because droplets fall under the influence of gravity and because droplets possess inertia so that they do not respond to the flow instantaneously. The following four dimensionless parameters are relevant for the study of the mechanical effect of an individual particle or the overall effect of a group of particles on the turbulent flow.

- The ratio of particle diameter (d) to a characteristic length scale (l) of the flow (either the Kolmogorov length scale or the integral scale)
- The Stokes number which is the ratio between the particle's response time (defined in Section 4.1.2) and a characteristic time scale of the flow (either the time scale associated with the Kolmogorov length scale or with the integral scale). The particle's response time, also called the particle's relaxation time scale or the Stokes time scale, is a characteristic time the particle takes to react to changes in the flow.
- The particle's Reynolds number, $Re_P = U R/\nu$, where U is the relative velocity between the flow and the particle, ν is the kinematic viscosity of the fluid, and R is the radius of the particle.
- The mass loading, given by the liquid water mixing ratio.

The first three parameters govern the type of interaction that can be expected between the particles and the flow. For $d/l \approx 1$, the diameter of the particles is comparable to the Kolmogorov length scale, and the particles will exert a direct influence on the structures of the flow on that scale. Particles with a large Stokes number will react very slowly to the changes in the flow while particles with a small Stokes number behaves essentially like a tracer because its reaction to any change in the flow is almost instantaneous. It is expected that there is maximum interaction between the flow and the particles when the Stokes number is close to one. The

Reynolds number is important because particles with large Reynolds number influence directly the turbulent kinetic energy through vortex shedding.

Table 2.2 shows the possible range for the radii of cloud droplets, their associated terminal velocity, Reynolds number and the Stokes number for different eddy dissipation rates. We note that the typical size of cloud droplets is much smaller than the typical Kolmogorov length scale found in clouds (see Section 2.2). Thus cloud droplets are not expected to exert a direct influence on the structure of the flow. The Stokes number approaches 1 only for the largest cloud droplets in a cloud with very active turbulence ($\epsilon \approx 1000 cm^2 s^{-3}$). Hence under most conditions, it is anticipated that the relative velocity between the flow and the droplets is mostly associated with sedimentation. Cloud droplets are also unlikely to affect the flow by vortex shedding because their Reynolds number is $\ll 1$.

We turn now to the effect of mass loading. This parameter can be used to infer the overall effect of all the particles in a certain volume on the turbulent flow. When the mass loading is small, the overall effect of particles can be neglected. When the mass loading is appreciable, experimental data show that the presence of particles may either increase or decrease the turbulent kinetic energy of the carrier fluid, depending on the magnitude of other parameters defined above. Unfortunately, there is no clear understanding of the underlying mechanism (Elghobashi and Truesdell 1993). Furthermore, there is no consensus as to the precise range of the above four parameters which would effect an increase or a decrease in turbulent energy. Two examples will serve to illustrate this point. In the first example, we note that Hestroni (1989) suggested that when $Re_P < 400$, a decrease in turbulence energy should be expected while for larger Re_P turbulence should be enhanced due to vortex shedding. However, other experimental evidence (Hardalupas et al. 1989) demonstrated an increase in turbulence energy for small Re_P. As a second example of this controversy, we note that Gore and Crowe (1989), based on various experimental results, proposed

that the relevant parameter should be d/l, the ratio between the particle diameter and the integral scale of the turbulent flow. The critical value is $d/l \approx 0.1$. The turbulence intensity increased above this critical value and it decreased below this value. However, the numerical results of Elghobashi and Truesdell (1993) show an increase in turbulence intensity for $d/l \approx 10^{-3}$ and $Re_P < 1$.

Squires and Eaton (1990) conducted a series of numerical experiments on the interaction between a turbulent flow and non-sedimenting particles. The Stokes number in their experiments was around .5 and the mass loading varied between .1 and 1. They found that for a mass loading of 1., over 50% of the total dissipation was caused by the drag of the particles and this percentage decreased to $\approx$ 10% for a mass loading of .1. Elghobashi and Truesdell (1993) conducted similar numerical experiments in the context of a decaying turbulent flow field for both sedimenting and non-sedimenting particles. Their Stokes number was about 1 and their mass loading varied from .2 to .9. They found a similar decrease in the effect of the particles on the flow as the mass loading decreased. However, they also found that sedimenting droplets with small Reynolds number can be a net source of turbulent kinetic energy for the flow even though vortex shedding is not expected to occur. Nevertheless, these two studies showed that for a constant mass loading, the effect of the particles on the flow decreases with a decrease in Stokes number.

The typical mass loading found in clouds is in the range .001 - .01 (1 to $10 gkg^{-1}$ of liquid water content). These values are one or two orders of magnitude smaller than the typical mass loading examined in the above studies. In the experiments that we will describe in the following chapters, the mass loading is close to .001 and the Stokes number of the cloud droplets does not exceed .16. It is therefore expected that the effect of cloud droplets on the turbulent flow is negligible. Unpublished work by S. Elghobashi and his team at such small mass loadings confirm this assumption

(personal communication). Furthermore, this conjecture is confirmed in simple numerical experiments presented in Section 7.4. Based on our scaling arguments and the numerical results, we will neglect any mechanical effect of the particles on the flow in most of our experiments discussed in subsequent chapters.

Radius $R(\mu m)$	Terminal velocity $V_T(cms^{-1})$	Reynolds number Re_P	Particle response time $\tau_P(sec)$	Stokes for $\epsilon = 10cm^2s^{-3}$ τ_P/τ_η	Stokes for $\epsilon = 100cm^2s^{-3}$ τ_P/τ_η	Stokes for $\epsilon = 1000cm^2s^{-3}$ τ_P/τ_η
5	0.3	$.9 \times 10^{-3}$	$.3 \times 10^{-3}$	$.2 \times 10^{-2}$	$.8 \times 10^{-2}$	$.3 \times 10^{-1}$
10	1.2	$.7 \times 10^{-2}$	$.1 \times 10^{-2}$	$.8 \times 10^{-2}$	$.3 \times 10^{-1}$	.1
15	2.7	$.2 \times 10^{-1}$	$.3 \times 10^{-2}$	$.2 \times 10^{-1}$	$.8 \times 10^{-1}$	.3
20	4.8	$.6 \times 10^{-1}$	$.5 \times 10^{-2}$	$.4 \times 10^{-1}$	.1	.5
25	7.5	.1	$.8 \times 10^{-2}$	$.6 \times 10^{-1}$	.2	.8

Table 2.2: Characteristic scales of cloud droplets

We comment briefly on the thermodynamic effect exerted by the particles in the form of sources or sinks of latent heat and water vapor exchange when the droplets grow and evaporate. These exchanges can cause fluctuations in temperature and water vapor which may influence the dynamics of the turbulent flow through the buoyancy term. We performed sensitivity experiments in Section 7.4 by including and excluding the thermodynamic effect and found that the difference in the results for our small scale turbulent flow is small. In the same section we also present a simple scale analysis to explain this result. Therefore, the thermodynamic effect will also be neglected in most of our experiments in subsequent chapters.

2.4.2 Effects of turbulent flow on spatial distribution of particles

Studies on the dispersion of particles in homogeneous flows are relevant to our work. Numerical simulations by Squires and Eaton(1990;1991) and Wang and Maxey (1993)

showed that, due to their inertia, particles tend to diverge from regions of high vorticity and converge preferentially in regions of low vorticity and high strain rate (saddle or stagnation points). As a result, their spatial distribution is not random and does not follow a Poisson distribution. This phenomenon of clustering has been confirmed by Fessler et al. (1994) in experimental work involving particles in a turbulent channel flow. Further results from numerical simulations by Squires and Eaton(1990;1991) and Wang and Maxey (1993) indicated that the clustering is a function of the Stokes number based on the fluid time scale associated with the Kolmogorov length scale. Clustering occurred for Stokes number between 1 and 10 and was most important at Stokes number close to 1. However, no lower bound on the Stokes number for this effect has been established. Very light (small Stokes number) and very heavy particles (large Stokes number) show less tendency to cluster because the light ones follow the fluid elements and the heavy ones are less affected by the turbulence. Maxey(1987) also showed that because of the bias in the particles trajectory towards regions of low vorticity, the average settling velocity of the particles is inertia dependent and is not simply given by the sum of the terminal velocity of the particles and the mean fluid velocity. Furthermore, he showed analytically that this effect may be important even for low values of particle inertia.

It is of interest to enquire whether clustering may also apply to particles like cloud droplets? As was shown in Table 2.2, the Stokes number approaches 1 for the largest droplets in moderate to strong turbulence. Under these conditions, significant clustering of droplets can be expected. However, the time of interaction between the droplets and the smallest eddies of the flow (η/V_T see Table 3.1) decreases as the Stokes number approaches unity. This is because larger droplets have larger terminal velocities and also because the Kolmogorov length scale is smaller at higher eddy dissipation rates. This counteracting effect may impose a limit on the extent of the clustering.

In recent years, new instruments and better statistical analysis methods have allowed the direct observation or the analysis of spatial homogeneity in droplet concentration down to the *mm* scale. Baker (1992) found inhomogeneities in droplet concentration at the *cm* scale that may be real deviations from Poisson (personal communication). However, by analyzing data taken with the Fast FSSP from many cloud passes, J.-L. Brenguier and his team found no clear deviations from Poisson down to the scale of a few millimeters, the highest resolution which they can resolve (personal communication). A new instrument which records the exact position of droplets but samples only small cloud volumes is the HODAR (holographic droplet and aerosol recording system). Kozikowska et al. (1984), Borrmann (1993) and Uhlig et al. (1998) analyzed the spatial distribution of cloud droplets in holograms of cloud volumes of the order of $10cm^3$ using ground based HODARs. While Borrmann found no deviations from Poisson statistics, the other two studies did. In particular, Uhlig et al. (1998) found that the deviations from Poisson were more significant when the spatial distribution of only the largest droplets (larger Stokes number) in the sample volume were analyzed.

In summary, some evidence exists that clustering on scales below a few centimeters may occur for cloud droplets in natural clouds. The clustering can lead to a non-random spatial distribution of cloud droplets and may have potentially important effect on cloud droplet growth by condensation. Pinsky et al. (1996) and Shaw et al. (1998) studied the broadening of the size distribution by artificially imposing drastic variations in concentration on the scale of a few *cms*. Not surprisingly, they found important broadening. However, these studies are not conclusive because of the highly idealized way in which variations in concentration of droplets are imposed.

Furthermore, Khain and Pinsky (1995) has suggested that drop inertia in a turbulent flow may even accelerate the coalescence process. In Chapter 7 we explore the clustering of sedimenting and non-sedimenting cloud droplets at three different levels

of turbulence. We then examine whether this clustering may affect the width of the size distributions.

Chapter 3

Scale analysis of droplet growth by condensation

We deal with an ensemble of cloud droplets ranging in size from several to tens of microns. The droplets are distributed non-uniformly in space and are moving in a turbulent flow field. They are growing by diffusion of water vapor from the ambient environment onto their surface. To properly calculate the growth of the droplets by condensation, we have to solve the convective-diffusive equations for water vapor and heat, both inside and outside the droplets, subject to the appropriate boundary conditions at the surface of all the droplets. Kinetic corrections have to be made for those droplets whose Knudsen number (ratio of the molecular mean free path of the gas to the radius of the drop) is not too small compared to unity. However, for many droplets in constant motion, this direct approach becomes impractical. To make the problem tractable but physically realistic, we shall perform a scale analysis on the time and spatial scales to obtain a simplified set of equations for the growth of cloud droplets. We shall show that a scale separation exists between the time and spatial scales related to the modification of the scalar fields by turbulence and that related to the growth of the cloud droplets. Our analysis would also shed light on the limitation

of our simplifications.

3.1 Time and spatial scales associated with the ambient conditions

The concept of ambient environment or ambient conditions for a droplet is important but does not have a strict definition. It refers to environmental conditions (temperature and water vapor density) sufficiently far away from a droplet such that the presence of the droplet exerts negligible influence on the gradients in these quantities. As will be shown in the next section, this far away distance is typically of the order of several tens of droplet radii.

Droplets distributed non-uniformly create structures in the temperature and water vapor fields which are modified by turbulence. Furthermore, because of sedimentation, the droplets fall through these structures. The droplets are therefore subject to a variable ambient environment. We will evaluate the spatial and time scales associated with these sources of variability.

The typical scale of the smallest significant spatial structure in a turbulent flow is the Kolmogorov length scale η. This scale is, strictly speaking, only valid for kinematic fields. However, the coefficients of viscosity of air, thermal diffusion and water vapor diffusion are all of the same order of magnitude. Therefore the Kolmogorov length scale can also be applied to scalar fields where it is sometimes known as the Batchelor scale. The Kolmogorov length scale and the associated time and velocity scales relevant to clouds are discussed in the previous chapter and the values were summarized in Table 2.1.

There are two time scales which are related to the changes in ambient conditions associated with these small turbulent structures. The first is the eddy turnover time characteristic of the lifetime of these structures. The second is the time it takes for a

droplet to sediment a distance η. Table 3.1 lists these two time scales for various eddy dissipation rates and droplet radii. Note that the time scales are generally of the same order of magnitude except for large R and small values of the eddy dissipation rate. The fastest time scale, corresponding to the largest values of η and R considered, is $.006sec$.

	$\eta/V_T(sec)$ for			
Radius $R(\mu m)$	$\epsilon = 1cm^2s^{-3}$	$\epsilon = 10cm^2s^{-3}$	$\epsilon = 100cm^2s^{-3}$	$\epsilon = 1000cm^2s^{-3}$
5	0.8	0.5	0.3	.15
10	0.2	0.1	.07	0.04
15	0.1	0.05	0.03	0.02
20	0.05	0.03	0.02	.009
25	0.03	0.02	0.01	.006
	Eddy turnover time $\tau_\eta(sec)$			
	.4	.13	.04	.01

Table 3.1: Time scales associated with ambient conditions

3.2 Time and spatial scales associated with diffusional growth

The growth of cloud droplets in the size range considered involves several processes. Water vapor is transported from the environment to the droplet-air interface by molecular diffusion and by convective transport (ventilation effect). The latent heat released at the droplet-air interface is transported both to the environment and inside the liquid droplet by the same processes. These processes can be calculated explicitly by solving a set of three convective-diffusive equations for water-vapor, heat outside the droplet and heat inside the droplet. Sedunov (1974) analyzed the typical Peclet (ratio of convective over diffusive transport of water vapor) and Reynolds numbers

associated with the flow inside and outside growing droplets and concluded that the convective transport (ventilation effect) can be neglected for droplets with a radius smaller than $30\mu m$. The convective-diffusive equations can then be simplified to the pure diffusion equations of the form:

$$\frac{\partial X}{\partial t} = D\nabla^2 X,$$

where X refers to either water vapor density or heat and D is the appropriate diffusion coefficient.

In the classical solution for the diffusional growth of a cloud droplet, the ambient water vapor density and heat are assumed to be in a steady state relative to the adjustment of these fields close to the droplet-air interface. Since our objective in this work is to explicitly solve for the growth of individual droplets growing by diffusion in a turbulent flow, the validity of the steady state assumption for water vapor density and heat in the ambient environment is not obvious and has to be re-evaluated. Specifically, we must demonstrate that the time scale for changes in the ambient environment is much longer than other relevant time scales involved.

We begin our evaluation of other relevant time scales by considering the initial value problem of radially symmetric diffusion of water vapor onto a still droplet of radius R. If r is the radial distance measured from the center of the droplet, and if the boundary and initial conditions are $\rho_v(R,t) = \rho_{v,R}$ = constant and $\rho_v(r,0) = \rho_{v,\infty}$ = constant for $r > R$, the solution of the diffusion equation for water vapor then becomes:

$$\rho_v(r,t) = \rho_{v,\infty} + (\rho_{v,R} - \rho_{v,\infty})\frac{R}{r}[1 - \mathrm{erf}(y)]. \tag{3.1}$$

where $\rho_{v,\infty}$ is the ambient value for the water vapor density, $y = \frac{r-R}{2\sqrt{D_v t}}$ and $\mathrm{erf}(y) = \frac{2}{\sqrt{\pi}}\int_0^y e^{-z^2}dz$ is the error function.

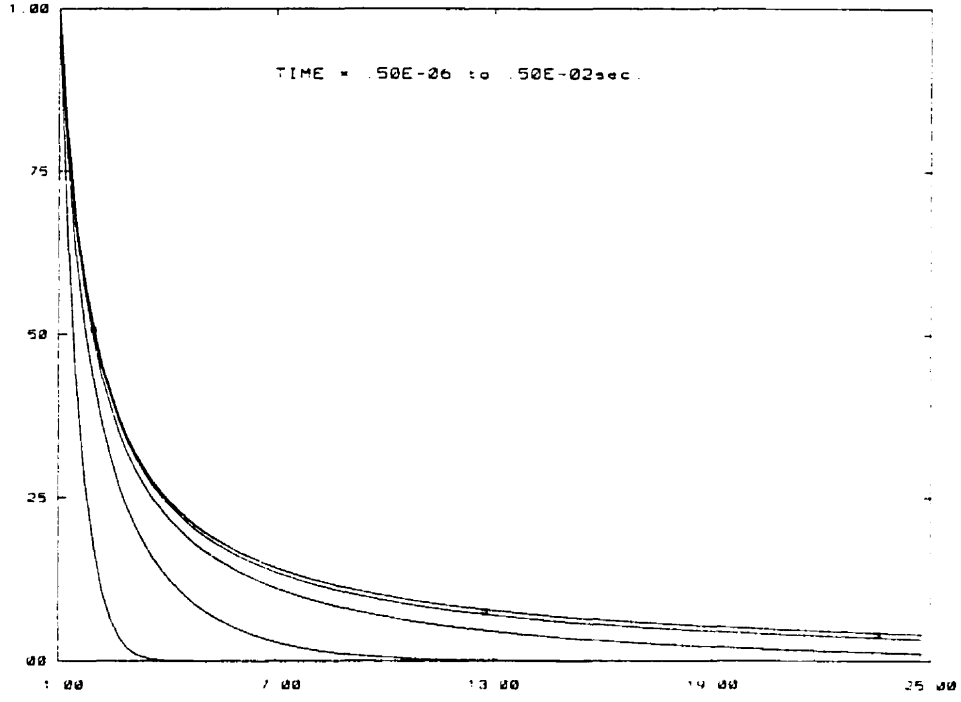

Figure 3.1: Water vapor density profile near a droplet-air interface at five different times

Equation 3.1 can be used to give a more precise view when recast in the form:

$$\frac{\rho_v(r,t) - \rho_{v,\infty}}{\rho_{v,R} - \rho_{v,\infty}} = \frac{R}{r}\left[1 - \mathrm{erf}(y)\right]$$

which yields the fractional approach of $\rho_v(r,t)$ to the ambient value. Figure 3.1 shows this ratio as a function of r/R at various times. It is obvious that beyond ≈ 20 droplet radii, the ambient condition is approached as the variation is negligible. A distance of about 20 droplet radii therefore delimits the range of direct influence of the droplet.

To obtain the time scales, we calculate the water vapor flux, I, diffusing to the droplet as:

$$I(t) = 4\pi R^2 D_v \frac{\partial \rho_v}{\partial r}\Big|_{r=R} = 4\pi R D_v(\rho_{v,R} - \rho_{v,\infty})\left(1 + \frac{R}{\sqrt{\pi D_v t}}\right). \qquad (3.2)$$

and the steady state form of (3.2) becomes $I_0 = 4\pi R D_v(\rho_{v,R} - \rho_{v,\infty})$.

If the characteristic time for vapor diffusion τ_v is defined as the time for I to reach twice the value of I_0, then $\tau_v = R^2/\pi D_v$. Using a similar set of equation, as well as boundary and initial conditions for the diffusion of heat, we can obtain respectively the characteristic time scales associated with the temperature inside and outside the droplet as $\tau_{Ti} = R^2/\pi k_w$ and $\tau_{To} = R^2/\pi k_a$, where k_a and k_w are the thermal diffusivities of air and liquid water.

Table 3.2 lists the characteristic time scales for several cloud droplet radii of typical sizes. The first three columns contain the vapor and temperature diffusion time scales defined above. It is evident that the slowest of these three time scales is that associated with the diffusion of the temperature inside the droplet and it varies between values of $.6 \times 10^{-4}$ and $.1 \times 10^{-2}$ *sec*. The other two time scales are almost two orders of magnitude faster.

Radius $R(\mu m)$	Vapor $\tau_v(sec)$	Temp. outside droplet $\tau_{To}(sec)$	Temp. in droplet $\tau_{Ti}(sec)$	Psychrometric temp. $\tau_{T_R}(sec)$
5	$.3 \times 10^{-6}$	$.3 \times 10^{-6}$	$.6 \times 10^{-4}$	$.5 \times 10^{-3}$
10	$.1 \times 10^{-5}$	$.1 \times 10^{-5}$	$.2 \times 10^{-3}$	$.2 \times 10^{-2}$
15	$.3 \times 10^{-5}$	$.3 \times 10^{-5}$	$.5 \times 10^{-3}$	$.5 \times 10^{-2}$
20	$.5 \times 10^{-5}$	$.5 \times 10^{-5}$	$.9 \times 10^{-3}$	$.9 \times 10^{-2}$
25	$.8 \times 10^{-5}$	$.8 \times 10^{-5}$	$.1 \times 10^{-2}$	$.1 \times 10^{-1}$

Table 3.2: Characteristic time scales of cloud droplet diffusional growth

There is another time scale which appears when the boundary conditions for water vapor density and temperature at the surface of the droplet are not assumed to be held constant. This is indeed the more realistic situation because as water vapor diffuses onto the surface of the droplet during the condensation process, latent heat is released and the surface temperature of the droplet changes. Kinzer and Gunn (1951)

and Watts and Farhi (1975) evaluated the relaxation time scale for surface temperature change by suddenly exposing a droplet to a new ambient condition and then solving the energy balance equation at the droplet's surface. They calculated the psychrometric temperature, the temperature at the surface of the droplet, and obtained the e-folding time associated with the relaxation of the psychrometric temperature to its steady state value as:

$$\tau_{T_R} = \frac{c_w \rho_w R^2}{3k_a \left(1 + \frac{\rho_{v,sat} D_v L^2}{k_a R_v T^2}\right)}.$$

It should be noted that the water vapor density just above the droplet's surface will also vary with a similar time scale.

This relaxation time scale is listed in the last column of Table 3.2. It varies in value between $.5 \times 10^{-3}$ and $.1 \times 10^{-1}$ for the droplet radii considered and is therefore the slowest time scale associated with the condensational growth of a droplet. We will therefore compare this time scale to the time scales related to changes in ambient conditions to determine if the steady state assumption for water vapor density and heat in the ambient environment is justifiable in the derivation of the droplet growth equation.

3.3 Presence of other droplets

Before we can make a comparison of the time scales, there is one additional complication we have to deal with. It is well known that droplets do not grow in a state of total isolation but can influence each other. To resolve this problem, we must estimate the extent of interaction between droplets or between droplets and the ambient environment.

We can identify two regimes of interaction, the direct and the indirect. The indirect regime occurs when droplets interact only through their common influence on the

ambient vapor density and temperature fields. As pointed out by Srivastava(1989), the steady-state diffusion field with its $\frac{1}{r}$ dependence (see equation 3.1) is a long range field and even arbitrarily distant regions can make a significant contribution to the diffusing field at any point. Thus, if steady state diffusion fields are assumed, the supersaturation in the vicinity of a droplet can be affected by arbitrarily distant regions. In reality, of course, diffusion occurs at a finite rate and at any given time only a finite volume of space can affect a given point.

Direct interaction or competitive growth occurs when the droplets are so close that their individual profiles of vapor density and temperature overlap. Carstens et al. (1970) numerically solved the problem of two droplets (5 and $10\mu m$) undergoing direct interaction. They calculated the growth rate of the surface area of the large droplet and the small droplet when they are in isolation and when they are close to each other. It was found that the radius of the smaller droplet grows faster than that of the larger one, but not as fast as their isolated counterparts. Politovich and Cooper (1988) estimated that the change in mass flux to a growing droplet when an identical droplet is placed at a distance $10R$ from it is about 11%.

Although direct interaction can occur, a relevant question is what proportion of the droplets in a cloud actually undergoes significant interaction. In a randomly distributed population of droplets, the average inter-droplet distance can be estimated by $.554N^{-1/3}$ (Underwood 1970, page 84), where N is the average concentration. For example, at concentrations of 50 and $1000cm^{-3}$ the average inter-droplet distance is 1500 and $500\mu m$ respectively. Hence the average inter-droplet distance is greater than the approximate $10R$ criterion for significant direct interaction. Carsten et al. (1970) and Politovich and Cooper (1989) assumed a randomly distributed population of droplets and evaluated the proportion of droplets close enough to be under a direct interaction regime. They found the fraction varies from .001 to .4%. Since this fraction is small and since droplets move with respect to one another so that their time

of interaction is limited, the authors concluded that the effect of direct interaction between droplets can be neglected. Based on these results, we will include only the effect of indirect interaction in the formulation of our model for droplet growth in Chapter 4. Furthermore, since this simplification is more valid at lower concentrations of cloud droplets, our simulations will be done with low concentrations of droplets.

3.4 Scale separation

We are in a position to compare the time scales associated with changes in the ambient conditions and those associated with droplet growth. Table 3.3 contains the ratio of the slowest time scale associated with the droplets (τ_{T_R}) and the fastest time scale associated with the ambient conditions (Table 3.1) for various values of R and ϵ.

	Eddy dissipation rates $\epsilon(cm^2s^{-3})$				
Radius R (μm)	.1	1	10	100	1000
5	$.4 \times 10^{-3}$	$.1 \times 10^{-2}$	$.4 \times 10^{-2}$	$.1 \times 10^{-1}$	$.5 \times 10^{-1}$
10	$.5 \times 10^{-2}$	$.1 \times 10^{-1}$	$.2 \times 10^{-1}$	$.5 \times 10^{-1}$	.2
15	$.2 \times 10^{-1}$	$.5 \times 10^{-1}$	.1	.2	.5
20	$.9 \times 10^{-1}$	.2	.3	.45	1.
25	.2	.3	.5	1.	1.6

Table 3.3: Ratio of droplet growth and ambient time scales

This table reveals the conditions under which the assumption of steady state condensation is valid. For R smaller than $20\mu m$ and eddy dissipation rates smaller than $100cm^2s^{-3}$, the ratio between the time scales is much less than one and the assumption is justifiable. The assumption becomes less valid as the size of the droplet and the eddy dissipation rate increase. For example for droplets larger than $25\mu m$ and dissipation rate greater than $100cm^2s^{-3}$, it may be necessary to explicitly solve for the non-steady-state psychrometric temperature. For the droplet growth problem

considered in this thesis, most of the cloud droplets considered have a radius below $20\mu m$ and the eddy dissipation rates are less than $200cm^2s^{-3}$. Thus the steady-state assumption for the distribution of water vapor density and temperature in the diffusional growth of cloud droplets is still justifiable.

Chapter 4

Model equations

We describe in this chapter two sets of equations governing the growth of cloud droplets. The first set, referred to as the *microscopic* equations, models explicitly the evolution of the turbulent flow, the scalar fields of temperature and water vapor, as well as the movement of the droplets and their growth by condensation within a three-dimensional air parcel. The parcel is prescribed to rise at a constant ascending rate. The resulting adiabatic cooling contributes to the generation of supersaturation in the air parcel. The space coordinate for all *microscopic* variables are measured relative to the ascending parcel. The second set of equations, referred to as the *macroscopic* equations, constitutes a simplified version of the *microscopic* equations in the sense that the whole air parcel is treated as a single entity. It represents the classical equations for the growth of a population of cloud droplets in an ascending updraft. Hence, turbulence is not explicitly resolved, and all the droplets are submitted to the same *macroscopic* supersaturation have the same growth history.

4.1 Microscopic equations

4.1.1 Droplet growth equation and condensation rate

In Chapter 3, we established the validity of the following assumptions for the growth of cloud droplets in a turbulent flow:

(a) Convective transport to the droplet-air interface is negligible relative to the diffusive fluxes.

(b) The time scales associated with the diffusive adjustment of vapor and temperature fields (inside and outside the droplet) are significantly smaller than the time scale associated with changes in the ambient conditions due to turbulence and sedimentation.

(c) The time scale associated with the relaxation to steady state psychrometric temperature (steady state condensation) is sufficiently smaller than the time scale associated with changes in the ambient conditions.

(d) The droplets can be considered to be growing in isolation and interact indirectly with the other droplets through their effect on ambient conditions.

Employing these assumptions, it is possible to parameterize the growth of a droplet as a function of its ambient conditions. To do so, we calculate the steady state mass flux onto a droplet using (3.2) and compute the steady state psychrometric temperature at the droplet's surface by solving an energy balance equation (Pruppacher and Klett 1978, page 419). Using the Clausius-Clapeyron equation and the equations of state for water vapor and dry air, together with the assumption that the water vapor density at the droplet's surface equals the saturation vapor density at the psychrometric temperature, we obtain the equation for the rate of growth of the radius of a droplet as:

$$\frac{dR^2}{dt} = 2KS, \tag{4.1}$$

where S the supersaturation is defined in terms of the vapor pressure as $S = e_\infty / e_{sat(T_\infty)} - 1$ and

$$K^{-1} = \frac{\rho_w R_v T_\infty}{e_{sat}(T_\infty) D_v} + \frac{L\rho_w}{k_a T_\infty}\left(\frac{L}{T_\infty R_v} - 1\right) \tag{4.2}$$

can be assumed constant over the range of pressure and temperature considered. The subscript ∞ again refers to ambient conditions. From hereafter we will drop this subscript for simplicity. Instead of calculating the supersaturation using vapor density, we shall use the vapor mixing ratio and compute $S = q_v / q_{vsat} - 1$. It is simple to show that under typical conditions, the relative difference between the two definitions for S amounts to less than .1%.

By summing the rate of increase of mass of an individual droplet over the total population in a unit mass of dry air, we obtain the condensation rate [per unit mass] as

$$C_d = \frac{1}{M_a}\frac{dM_{Liq}}{dt} = \frac{1}{M_a}\frac{4}{3}\pi\rho_w \sum_{i=1}^{n} \frac{dR_i^3}{dt} = \frac{1}{M_a} 4\pi\rho_w \sum_{i=1}^{n} R_i K S_i. \tag{4.3}$$

where n is the number of droplets in a volume of dry air with mass M_a and use has also been made of (4.1). Note that S_i refers to the supersaturation resulting from the ambient conditions of the i^{th} droplet.

4.1.2 Equations for the velocity of a droplet and its position

In general, three types of forces act on particles moving in a fluid - external forces, resistance of the medium(drag) and interaction between particles. For our problem, gravity is the only external force and the concentration and size of particles are small enough that any interaction (collision) between the particles can be neglected. Under these conditions the equation of motion for a particle of mass m_p, according to Newton's law of motion, is:

$$m_p \frac{d\mathbf{V}(t)}{dt} = \mathbf{F}_{res} + m_p \mathbf{g}. \tag{4.4}$$

To solve for the particle's trajectory it is necessary to calculate the resistance forces $\mathbf{F}_{res}$. In theory, this can be accomplished by solving the Navier-Stokes equation for the flow around the particle with appropriate boundary conditions and then integrating the resulting stress over its surface. The resultant integrodifferential equation is however quite complex (e.g. see Maxey and Riley 1983). Fortunately, for our application simplifications can be made by noting that the cloud droplets under consideration have low Reynolds number (see Table 2.2). Therefore, a Stokes drag law may be assumed, and the resistance force is reduced to $\mathbf{F}_{res} = 6\pi R\mu(\mathbf{U}(\mathbf{X}(t), t) - \mathbf{V}(t))$ (Pruppacher and Klett 1978, page 290), where $\mathbf{U}(\mathbf{X}, t)$ is the undisturbed flow velocity at the particle's position , $\mathbf{X}(t)$ is the position of the particle and μ is the dynamic viscosity. Furthermore, since the density of water is much greater than the density of air many of the forces in the equation of motion may be neglected (Maxey and Riley 1983). The equation of motion for a cloud droplet in a turbulent flow therefore takes on a simpler form:

$$m_p \frac{d\mathbf{V}(t)}{dt} = 6\pi R\mu(\mathbf{U}(\mathbf{X}(t), t) - \mathbf{V}(t)) + m_p\mathbf{g} \text{ or}$$

$$\frac{d\mathbf{V}(t)}{dt} = \frac{1}{\tau_P}(\mathbf{U}(\mathbf{X}(t), t) - \mathbf{V}(t)) + \mathbf{g} \tag{4.5}$$

where $\tau_P = m_p/6\pi R\mu = 2\rho_w R^2/9\mu$ is the particle response time. Equation (4.5) can be recast in an alternate form by introducing the notion of terminal velocity. When there is no motion in the fluid, i.e. $\mathbf{U}(\mathbf{X}, t)$ is zero, (4.5) can be solved analytically to yield:

$$\mathbf{V}(t) = \tau_P\mathbf{g}\left[1 - exp^{-t/\tau_P}\right]$$

$$= \mathbf{V_T}\left[1 - exp^{-t/\tau_P}\right]$$

where $\mathbf{V_T}$ is the terminal fall velocity of the droplet. The time τ_P therefore appears as a relaxation time scale. It is the time for the droplet to reach about 67% of its terminal velocity.

Using the definition of $\mathbf{V_T}$, (4.5) becomes:

$$\tau_P \frac{d\mathbf{V}(t)}{dt} = \mathbf{U}(\mathbf{X}(t), t) - \mathbf{V}(t) + \mathbf{V_T} \tag{4.6}$$

$$\frac{d\mathbf{X}(t)}{dt} = \mathbf{V}(t) \tag{4.7}$$

and the particle's position can be obtained by solving (4.7).

It is of interest here to discuss briefly the significance of the inertia term (or acceleration term) in (4.6). The importance of this term depends on the ratio of the particle response time to the fluid's fastest time scale (Stokes number). If this ratio is small, then the droplet responds almost instantaneously to all scales of motion of the fluid. In an isotropic turbulent flow the fastest fluid time scale is the time scale associated with the Kolmogorov length scale. We have shown in Table 2.2 the Stokes number for various droplet sizes and eddy dissipation rates. Clearly, for eddy dissipation rates less than $10 cm^2 s^{-3}$, the inertia of the droplets can be neglected. For larger values of the eddy dissipation rates, inertia can significantly influence the trajectory of the droplets particularly for the larger sizes, and must therefore be included in the equation of motion. It is of interest to note that when the particle's inertia is neglected, (4.6) reduces to

$$\mathbf{V}(t) = \mathbf{U}(\mathbf{X}(t), t) + \mathbf{V_T}. \tag{4.8}$$

which is simply the statement that the velocity of the particle is the sum of the terminal fall velocity and the flow velocity at the position of the particle. Under this condition, $\mathbf{F}_{res} = -m_p \mathbf{g}$, the drag force and the gravitational force are therefore in balance. Extending this to a population of droplets in a unit mass of air, the total drag force becomes $q_c \mathbf{g}$, where q_c is the liquid water mixing ratio.

4.1.3 Flow equation

It is assumed that the turbulent flow is governed by the Navier-Stokes equation with the incorporation of the Boussinesq approximation. With the inclusion of the buoyancy of water vapor and the drag force exerted by the cloud droplets, the equation for the case of constant kinematic viscosity ν takes on the form

$$\frac{\partial \mathbf{U}}{\partial t} + (\mathbf{U} \cdot \nabla)\mathbf{U} = \frac{-1}{\rho_{a0}} \nabla P^* - \mathbf{g}B + \nu \nabla^2 \mathbf{U} \tag{4.9}$$

$$B = \frac{T^*}{T_0} + .608 q_v^* - q_c^*$$

$$\nabla \cdot \mathbf{U} = 0 \tag{4.10}$$

The starred terms represent the perturbations relative to the time dependent domain average while ρ_{a0} and T_0 are the initial density and temperature of air in the domain. The perturbation pressure term P^* represents the pressure deviation from the hydrostatic pressure. The term $\mathbf{g}B$ is the buoyancy term which includes the effect of temperature and water vapor perturbations as well as the drag of the droplets on the flow. The simplified form for the drag force is valid when the inertia of the droplets is ignored or when the relative velocity between the drops and the flow due to inertia becomes negligible. As discussed in Section 2.4.1, in most of the experiments presented in subsequent chapters the buoyancy term will be neglected.

By taking the curl of (4.9), the vorticity equation becomes

$$\frac{\partial \omega}{\partial t} = -\nabla \times (\omega \times \mathbf{U}) - \nabla B \times \mathbf{g} + \nu \nabla^2 \omega, \tag{4.11}$$

where ω is the vorticity vector.

4.1.4 Scalar equations

Temperature

The evolution equation for temperature is derived from the principle of conservation

of energy by neglecting the specific heats of the water vapor and the droplets

$$\frac{\partial T}{\partial t} = -\nabla \cdot (\mathbf{U}T) - W\Gamma_d + \frac{L}{c_p}C_d + \kappa\nabla^2 T, \tag{4.12}$$

where c_p is the specific heat of dry air, κ is the coefficient of thermal diffusivity ,W is the vertical velocity, Γ_d is the dry adiabatic lapse rate and C_d is defined by (4.3). The non-divergent condition (4.10) was used to put the advection term in flux form. Note that we neglected the conversion of turbulent kinetic energy into internal energy by viscous dissipation. The rate of temperature change due to this source scales as ϵ/c_p. A simple calculation shows that this term is more than two order of magnitude smaller than the other source terms.

Water vapor mixing ratio

The evolution equation for the water vapor mixing ratio is

$$\frac{\partial q_v}{\partial t} = -\nabla \cdot (\mathbf{U}q_v) - C_d + D_v\nabla^2 q_v. \tag{4.13}$$

4.2 Macroscopic set of equations

The set of equations that describe the temporal evolution of *macroscopic* temperature, water vapor mixing ratio, pressure and cloud droplet size in an ascending parcel of moist air is

$$\frac{dT_M}{dt} = -W_M\Gamma_d + \frac{L}{c_p}C_{dM}, \tag{4.14}$$

$$\frac{dq_{vM}}{dt} = -C_{dM}, \tag{4.15}$$

$$\frac{dR_{iM}^2}{dt} = 2KS_M \tag{4.16}$$

$$C_{dM} = \frac{1}{M_a}4\pi\rho_w\sum_{i=1}^{n} R_{Mi}KS_M = 4\pi\frac{\rho_w}{\rho_a}NKS_M\overline{R}_M \tag{4.17}$$

$$\frac{dP_M}{dt} = -\rho_a g W_M \tag{4.18}$$

$$\rho_a = \rho_{a0} \tag{4.19}$$

The pressure is given by the hydrostatic equation. To be consistent with the Boussinesq approximation made in the *microscopic* equations, the density is held constant as in (4.19).

4.3 Perturbation equations for scalars

Subtracting (4.14) from (4.12) and (4.15) from (4.13) yields the perturbation form of the scalar equations

$$\frac{dT'}{dt} = -W'\Gamma_d + \frac{L}{c_p}(C_d - C_{dM}) + \kappa\nabla^2 T' \tag{4.20}$$

$$\frac{dq'_v}{dt} = -(C_d - C_{dM}) + D_v\nabla^2 q'_v, \tag{4.21}$$

where the perturbation terms $T' = T - T_M$, $q'_v = q_v - q_{vM}$ and $W' = W - W_M$ represent the differences in values between the *microscopic* and the *macroscopic* variables. As will be shown later, these perturbations are very small, i.e $\frac{T'}{T}$, $\frac{q'_v}{q_v} \ll 1$. Hence, for reasons of numerical accuracy, we solve (4.20) and (4.21) instead of (4.12) and (4.13). Whenever necessary, the total fields are obtained by simply adding the *macroscopic* variables to the perturbation fields. Note that we will refer to the term $-W'\Gamma_d$ as the cooling term.

Chapter 5

Numerical procedures

The two sets of equations developed in Chapter 4 are solved numerically as a marching problem from time step n to time step n+1. The choice of the size of the grid cells for the *microscopic* model depends on two factors. First, the grid cell values of temperature and water vapor mixing ratio must adequately represent ambient conditions for a cloud droplet situated in that grid cell. This imposes the conditions that the dimension of a grid cell should be $>\approx 20R$ (see Section 3.2) but small enough such that , on average, only a fraction of the grid cells contain one or more droplets. The second factor is that the turbulent flow must be properly resolved. In all of the experiments described in this thesis the grid cell size is $.125cm$. We use droplet concentrations of $\approx 50cm^{-3}$. Therefore, on average, only one grid cell out of ten contains a droplet. We will show in Chapter 7 that the turbulent flow is well resolved with such a grid length.

The choice of the number of grid cells depends essentially on computational limitations. All experiments without a turbulent flow (Chapter 6) use $120 \times 120 \times 120$ grid cells. The dimension of the computational domain is therefore $15cm \times 15cm \times 15cm$ and there are $\approx$ 170000 droplets in the domain. However, in all experiments with a turbulent flow (Chapter 7) the number of grid cells is reduced to $80 \times 80 \times 80$

because these experiments consume more memory and cpu time per time step. In the turbulence experiments, the dimension of the computational domain is therefore $10cm \times 10cm \times 10cm$ and there are ≈ 50000 droplets in the domain.

In all experiments the initial temperature and pressure is $T_m = 283.15K$ and $P_M = 90kPa$. The coefficients of thermal diffusivity and diffusion of water vapor evaluated at this temperature and pressure are $\kappa = 2.22 \times 10^{-5} m^2 s^{-1}$ and $D_v = 2.55 \times 10^{-5} m^2 s^{-1}$. These coefficients are treated as constants.

5.1 For droplet growth

To solve (4.1), the value of supersaturation is required. There are three common methods to calculate supersaturation (Hall 1980). They are the explicit method, the combined analytical/numerical method and the implicit method. The explicit method is the simplest. It involves solving directly the water vapor mixing ratio and temperature equations by including only the processes of diffusion and advection. The supersaturation is then diagnosed from the ratio of the water vapor mixing ratio and the saturation mixing ratio at the new temperature. The drawback of this method is that it does not treat simultaneously the combined effect of dynamical and microphysical processes which can be of the same order of magnitude (Clark 1973). The second method involves solving a linear equation for the tendency of supersaturation (e.g., Pruppacher and Klett 1978, eq. 13-29). The equation can be solved analytically to yield the average supersaturation over one time step. This supersaturation is then used in the droplet growth equation which can now be integrated with an explicit method. Chen (1994) developed a non-linear supersaturation equation which is more accurate particularly in subsaturated regions where evaporation occurs. The equation can also be solved analytically.

For reasons of generality and simplicity, the implicit method is employed in this

thesis. This method, detailed in Hall (1980), consists in solving the implicit equation $S^{n+1} = q_v^{n+1}/q_{vsat}(T^{n+1})$, where q_v^{n+1} and T^{n+1} are calculated from (5.6) and (5.7), by iteration using the Newton-Raphson method. Once S is determined, it is applied to the cloud droplet growth equation (4.1) which is then solved with a simple forward in time method.

Note that some grid cells contain more than one droplet because the droplets are distributed non-uniformly in space. However, there is only one value of supersaturation in each grid cell.

5.2 For droplet trajectory

To solve (4.6) or (4.8) for the velocity of the droplets, the velocity of the flow at the position of the droplet is required. Since the flow velocity is only available at a fixed grid cell, a linear interpolation scheme in three spatial directions (Yeung and Pope 1988) is used to obtain the flow velocity between grid cells. This scheme involves only the 8 nodal values of the interpolation cell. It approximates the dependent variable within the cell as a linear function in each coordinate. By enforcing the collocation condition, the interpolation weights can be determined uniquely. Time marching is done with a simple forward in time method.

To obtain accurate solution on the trajectories of the droplets, the time step must be much smaller than τ_P, the particle's response time. Elghobashi and Truesdell (1993), using a second order method to solve for the trajectory of the particles, used a time step that ranged from one half to one third of τ_P. In our experiments, we used a time step $\Delta t < \frac{1}{4}\tau_P$. Sensitivity tests with smaller time steps indicated little difference in the statistics of the spatial distribution of droplets.

5.3 For flow

Our objective is to obtain a statistically stationary three dimensional turbulent flow field. Ideally, we should simulate the whole range of scales including the large energy containing eddies, and eddies in the intermediate inertial subrange and the small dissipative scales. For practical purposes, the range of scales has to be limited. It is common practice to either model the small scales or to model the large scales using an artificial forcing term. Since our interest lies in the smallest scales, the latter approach will be adopted. The turbulent flow field will be obtained from direct numerical simulation (DNS) using the pseudo-spectral technique(Orszag 1971) as implemented in Bartello et al. (1994). The DNS method solves directly the Navier-Stokes equation (modified by the Boussinesq approximation in our context), rather than the Reynolds averaged equation, in predicting the evolution of the flow.

In physical space, the domain is a cube of side L with N^3 gridpoints. The gridpoints are located at $(l_1\Delta x, l_2\Delta x, l_3\Delta x)$, where l_1, l_2 and l_3 are integers between 0 and $N-1$ inclusively and $\Delta x = L/N$. In Fourier space, there are N^3 discrete wavenumbers $\mathbf{k} = (m_1 k_0, m_2 k_0, m_3 k_0)$, where m_1, m_2, m_3, are integers between $1 - N/2$ and $N/2$ inclusively. The lowest wavenumber k_0 is equal to $2\pi/L$. The magnitude of the wavenumber is often given in non-dimensional form as $(m_1^2 + m_2^2 + m_3^2)^{1/2}$.

Periodic boundary conditions are assumed in all three spatial directions. These boundary conditions permit the use of Fourier series expansion. The pseudo-spectral method implies evaluating spatial derivatives in Fourier space, but computing the non-linear terms in physical space. This procedure is faster than calculating the generalized convolution product involved in the calculation of the non-linear term in Fourier space. The fast Fourier transform(FFT) algorithm is used to evaluate transforms (denoted with an F) and inverse transforms(F^{-1}).

In Fourier space the vorticity equation is:

$$\frac{\partial \hat{\omega}}{\partial t} = -i\mathbf{k} \times F[F^{-1}(\hat{\mathbf{U}}) \times F^{-1}(\hat{\omega})] - i\mathbf{k} \times \mathbf{g}\hat{B} - \nu k^2 \hat{\omega}, \tag{5.1}$$

where the Fourier coefficients, denoted with a caret, are functions of time and $\mathbf{k}$, the wave vector. The velocity field is calculated using the identity

$$\nabla \times \omega = \nabla(\nabla \cdot \mathbf{U}) - \nabla^2 \mathbf{U} = -\nabla^2 \mathbf{U},$$

valid for a non-divergent flow. In Fourier space this equation simply becomes:

$$i\mathbf{k} \times \hat{\omega} = k^2 \hat{\mathbf{U}} \text{ which yields } \hat{\mathbf{U}} = \frac{1}{k^2}(i\mathbf{k} \times \hat{\omega}). \tag{5.2}$$

Time marching is done using the leap-frog scheme while the dissipative term is integrated exactly as follows. By multiplying (5.1) by $exp^{\nu k^2(t-t^n)}$, we obtain

$$\frac{\partial \hat{\omega}}{\partial t} exp^{\nu k^2(t-t^n)} + \nu k^2 \hat{\omega} exp^{\nu k^2(t-t^n)} = \hat{\mathbf{A}} exp^{\nu k^2(t-t^n)}.$$

where $\hat{\mathbf{A}}$ is the sum of the advective term and the buoyancy term. This equation can also be written as

$$\frac{\partial \hat{\omega} exp^{\nu k^2(t-t^n)}}{\partial t} = \hat{\mathbf{A}} exp^{\nu k^2(t-t^n)}.$$

Using the leapfrog time-differencing scheme to march from time step $n-1$ to $n+1$ results in

$$\frac{1}{2\Delta t}\left(\hat{\omega}^{n+1} exp^{\nu k^2(t^{n+1}-t^n)} - \hat{\omega}^{n-1} exp^{\nu k^2(t^{n-1}-t^n)}\right) = \hat{\mathbf{A}}^n.$$

which after some simple algebra yields the following equation to be solved in the present model

$$\hat{\omega}^{n+1} = \hat{\omega}^{n-1}\, exp^{-\nu k^2 2\Delta t} + 2\Delta t\, exp^{-\nu k^2 \Delta t} \hat{\mathbf{A}}^n. \tag{5.3}$$

Because the dissipative terms are treated exactly, they do not enter into consideration of numerical stability. It should be pointed out that knowledge of stability

constraints in spectral algorithms is limited, although restriction on the magnitude of the Courant number is often used to determine the maximum time step. In our case the Courant number can be defined as: $C' = \frac{max(|u|,|v|,|w|)}{\Delta x}\Delta t$. For stability reasons, we choose our time step to obey $C' < .25$. However, to allow for a uniform time step in solving both the flow equations and the droplet equations, the actual time step used is the lesser of $\Delta t < \frac{1}{4}\tau_P$ and the Δt necessary to respect $C' < .25$.

To avoid the separation of numerical solutions, a time filter as described in Robert (1966) and Asselin (1972) is employed. To start or restart the calculation a second order predictor-corrector scheme is used.

Using Kolmogorov's energy spectrum (2.1), we find that the eddy turnover time associated with a length scale L is $\tau_L \sim (L^2/\epsilon)^{\frac{1}{3}}$. For a domain size of approximately $10cm$ and typical values for the eddy dissipation rate, this time scale varies between a few seconds and fractions of a second. Therefore, for a numerical experiment which lasts longer than a few seconds, the eddy of size L will lose an appreciable part of its kinetic energy, and forcing at the large scales (small wavenumbers) is essential to maintain a stationary flow. To do so, the method outlined in Sullivan et al. (1994) will be used. The forcing scheme maintains the kinetic energy in a wavenumber band $|k| < K_f$. At the end of each time step the energy in this wavenumber band, E', is calculated as well as the ratio $E/E' = c^2$, where E is the initial energy in the wavenumber band. Energy is artificially put back into the flow by multiplying all Fourier coefficients of vorticity for $|k| < K_f$ by c. A statistically stationary state is achieved after some time when the average rate of energy addition is equal to the average energy dissipation rate. The mean kinetic energy will then oscillate around a constant value.

5.4 For scalars

A two step procedure is used to solve the scalar equations. First, equations (4.20) and (4.21) are marched forward in time by including only advection and diffusional processes. An intermediate temperature and water vapor mixing ratio (starred quantities) are obtained as in (5.4) and (5.5).

$$\hat{T}'^{*} = \hat{T}'^{n-1} exp^{-\kappa k^2 2\Delta t} - 2\Delta t\, exp^{-\kappa k^2 \Delta t} \left(\hat{W}'^{n} \Gamma_d + i\mathbf{k} \cdot F\left[F^{-1}(\hat{T}'^{n}) F^{-1}(\hat{\mathbf{U}}) \right] \right) \quad (5.4)$$

$$\hat{q}_v'^{*} = \hat{q}_v'^{n-1} exp^{-D_v k^2 2\Delta t} - 2\Delta t\, exp^{-D_v k^2 \Delta t} i\mathbf{k} \cdot F\left[F^{-1}(\hat{q}_v'^{n}) F^{-1}(\hat{\mathbf{U}}) \right] \quad (5.5)$$

The supersaturation is then calculated from the intermediate temperature and vapor mixing ratio using the method described in Section 5.1. Finally a new temperature and water mixing ratio at time step n+1 are computed from the intermediate values by including the microphysical processes in (5.6) and (5.7).

$$T'^{n+1} = T'^{*} + \Delta t \frac{L}{c_p} (C_d(S^{n+1}) - C_{dM}(S_M^{n+1})) \quad (5.6)$$

$$q_v'^{n+1} = q_v'^{*} - \Delta t (C_d(S^{n+1}) - C_{dM}(S_M^{n+1})). \quad (5.7)$$

5.5 For macroscopic equations

The macroscopic supersaturation is calculated using exactly the same procedure as for the microscopic supersaturation. All equations are advanced in time using a simple forward in time numerical scheme.

5.6 Formalism for analysis of spectral modifications

In the following chapters we will compare the results from the *microscopic* model and the *macroscopic* model. In addition to examining the perturbations, particularly that

of the supersaturation, in the scalar fields caused by the *microscopic* approach, we will analyze the difference in the growth of individual droplets and the difference in the size distributions between the two approaches. Much of our analysis will be in terms of a parameter called the *degree of growth*, defined in Brenguier (1991) as:

$$\beta^2 \equiv \int_0^t 2KSdt = 2K \int_0^t Sdt,$$

where the time integral is taken along a droplet's trajectory. To understand the meaning of this parameter, we refer to the droplet growth equation (4.1 or 4.16) which is:

$$\frac{dR^2}{dt} = 2KS.$$

The degree of growth, calculated as the time integral of the supersaturation along the trajectory of a given droplet, therefore represents the change in the surface area of the droplet.

We will make use of this parameter in our analysis for two reasons. First, we will demonstrate in what follows that it simplifies the interpretation of the evolution of the size distribution. Second, Brenguier and Chaumat (1996) analyzed observed cloud droplet size distributions in cloud cores at various altitudes. They calculated the probability distribution of the degree of growth which is required to explain the observed spectral evolution in adiabatic cloud cores. We will compare the distributions of this parameter in our numerical experiments to those inferred by Brenguier and Chaumat (1996) to determine if a *microscopic* approach can explain spectral broadening in adiabatic cloud cores.

The application of the parameter, the degree of growth, will now be clarified. First, we point out that within the *macroscopic* approach all droplets are submitted to the same supersaturation S_M and therefore possess the same degree of growth β_M^2. The time integral of (4.16) for the i^{th} droplet in the macroscopic model leads to:

$$\Delta R_{Mi}^2 \equiv {}^tR_{Mi}^2 - {}^0R_{Mi}^2 = \beta_M^2, \tag{5.8}$$

where the left superscripts t and 0 denote time and β_M^2 is referred to as the *macroscopic* degree of growth. Equation (5.8) states that all droplets undergo the same change in surface area β_M^2 during the time interval t. It is easy to show (Appendix A) that (5.8) implies that the variance of the R_M^2 spectrum is constant, i.e.

$$V({}^tR_M^2) = V({}^0R_M^2) \equiv V({}^0R^2). \tag{5.9}$$

where the last term on the right denotes the variance of the initial squared radius in the microscopic model. From (5.8), we can calculate β_M^2 given the initial and final drop sizes (or the initial and final average of the R_M^2 spectrum). Alternately, we can compute the final drop sizes once β_M^2 and ${}^0R_M^2$ are known.

Turning to the *microscopic* approach, the degree of growth for the i^{th} drop is:

$$\beta_i^2 = 2K\int_0^t S_i' dt + 2K\int_0^t S_M dt \equiv \beta_i'^2 + \beta_M^2. \tag{5.10}$$

where use has been made of $S_i = S_i' + S_M$. Using this result and the droplet growth equation (4.1), we obtain:

$$\Delta R_i^2 \equiv {}^tR_i^2 - {}^0R_i^2 = \beta_i'^2 + \beta_M^2. \tag{5.11}$$

Subtracting equation(5.8) from(5.11) we get:

$$\Delta R_i^2 - \Delta R_{iM}^2 = {}^tR_i^2 - {}^tR_{Mi}^2 = \beta_i'^2. \tag{5.12}$$

which expresses the simple but important fact that when the time integral of the supersaturation perturbation is non-zero, the squared radius of the i^{th} droplet in the *macroscopic* approach will be different from that in the *microscopic* approach. The term $\beta_i'^2$ is referred to as the perturbation degree of growth.

By averaging (5.12) over all droplets, we get $\overline{R^2} = \overline{R_M^2} + \overline{\beta'^2}$. As we will see in the numerical results, $\overline{\beta'^2}$ is not zero but is negative and $\ll \overline{R_M^2}$ or β_M^2. Consequently,

the average squared radius of the *microscopic* and *macroscopic* size distributions are practically the same. Furthermore, averaging (5.11) over all droplets we see that the change in the average squared radius of the *microscopic* size distribution is $\approx \beta_M^2$.

The variance of the R^2 distribution in the *microscopic* model can be derived from (5.12) and using the identity $V(x+y) = V(x) + V(y) + 2cov(x,y)$, where V and cov denote the variance and the covariance respectively. The result is:

$$V({}^tR^2) = V({}^tR_M^2) + V(\beta'^2) + 2cov(\beta'^2, {}^tR_M^2). \tag{5.13}$$

Using (5.9) and the result that $cov(\beta'^2, {}^tR_M^2) = cov(\beta'^2, {}^0R^2)$ (Appendix A), (5.13) can be rewritten as:

$$V({}^tR^2) - V({}^0R^2) = V(\beta'^2) + 2cov(\beta'^2, {}^0R^2). \tag{5.14}$$

Hence the perturbation degree of growth associated with the supersaturation perturbation is responsible for changes in the variance of the R^2 distribution. The first term on the right, the variance of the perturbation degree of growth over all droplets, must be positive and therefore contributes to a widening of the R^2 spectrum. In the numerical modeling context, this term can be obtained either by directly computing the time integral of the supersaturation perturbation for all droplets and then calculating $V(\beta'^2)$ at the end of the experiment. Alternately, we can use (5.12) and simply compute $V({}^tR^2 - {}^tR_M^2)$. The second term on the right in (5.14) can contribute to spectral broadening if it is positive or to spectral narrowing if it is negative. When normalized by the product of the standard deviations of β'^2 and ${}^0R^2$, this term is the correlation between the degree of growth and the initial size of the droplets. It should be noted that when this correlation is significantly negative, it implies that the growth of the droplets initially smaller (larger) than average is more (less) important in the *microscopic* approach than in the *macroscopic* approach (see (5.12)).

Equation (5.14) gives an estimate of the change in the variance of the squared radius. The terms on the right of this equation have a simple physical meaning and

thus facilitate the analysis of spectral changes. We are also interested in the change in the variance(or standard deviation) of the radius itself to gauge if broadening of the spectra occurs. Mathematically, $V({}^tR^2) - V({}^0R^2) > 0$ does not necessarily imply that $V({}^tR) - V({}^tR_M) > 0$.. However, it is possible to prove that when the dispersion of the size distribution is small, the following approximations are valid

$$V(R^2) \approx 4\overline{R^2}V(R) \tag{5.15}$$

$$V({}^tR^2) - V({}^0R^2) \approx 4\overline{\beta'^2}V({}^tR) + 4\overline{{}^tR_M^2}(V({}^tR) - V({}^tR_M)). \tag{5.16}$$

Equation (5.16) states that when $\overline{\beta'^2}$ is negative (always the case in our experiments), an increase in the variance of the squared radius always implies an increase in the variance of the radius itself. Furthermore, in all experiments presented in the following chapters, the first term on the right of (5.16) is always negligible compared to the second term. Hence, a decrease in the variance of the squared radius also always implies a decrease in the variance of the radius itself. Note that the difference in the variance of the radius is simply related to the difference in the standard deviation of the radius by $\sigma(R) - \sigma(R_M) = (V(R) - V(R_M))/(\sigma(R) + \sigma(R_M))$. Thus, the sign of the difference in the variance of the radius is necessarily the same as the sign of the difference in the standard deviation.

When comparing the results from the *microscopic* model to those of the *macroscopic* model or to observations we will often make use of the dispersion of the degree of growth distribution and the dispersion of the supersaturation distribution over all droplets:

$$d(\beta^2) \equiv \frac{\sigma(\beta^2)}{\overline{\beta^2}} \qquad\qquad d(S) \equiv \frac{\sigma(S)}{\overline{S}}.$$

Using $S_i = S_i' + S_M$, (5.10) and the fact that $\overline{\beta'^2} \ll \beta_M^2$ as well as $\overline{S'} \ll S_M$ we obtain the expressions for the dispersion used in subsequent chapters:

$$d(\beta^2) \approx \frac{\sigma(\beta'^2)}{\beta_M^2} \qquad\qquad d(S) \approx \frac{\sigma(S')}{S_M}. \tag{5.17}$$

Chapter 6

Experiments with no turbulence

In this chapter we will describe the results of experiments without turbulence. The important physical processes acting are molecular diffusion of heat and water vapor, condensational growth of the droplets and adiabatic cooling of an air parcel rising in a constant updraft. Equations (4.14) to (4.19) are solved for the *macroscopic* approach. For the *microscopic* approach, the equations solved are (4.1), (4.3),(4.20) and (4.21). The advection terms are excluded from (4.20) and (4.21) as well as the cooling term from (4.20).

As mentioned earlier, the average inter-droplet distance is of the same order of magnitude as the typical Kolmogorov length scale in clouds. Turbulence is therefore expected to be as important as molecular diffusion in determining the ambient conditions in which an individual droplet grows. Neglecting turbulence would seem unrealistic unless the flow is near laminar. However, our simplified experiments in this chapter are still very useful because they offer a much simpler context to interpret the effect of sedimentation and the sensitivity of spectral broadening to various initial conditions. Also we can compare directly our results to the analytical estimates obtained by Srivastava (1989). Finally, as will be shown in the next chapter, the no turbulence case sets an upper limit on spectral broadening.

Our models were thoroughly tested to ensure that the *microscopic* results do converge to the *macroscopic* results when the number of grid points approached one. Furthermore, sensitivity tests on the time steps showed that in the *microscopic* model, the results for spectral change do converge when the time step becomes smaller. In fact, these tests allowed us to choose an appropriate time step for our integration. The budgets for water and energy were also checked and they are conserved to within a fraction of a percent.

Table 6.1 contains the basic parameters for the ten experiments performed. In all experiments, the grid size used is $.125cm$ and the number of grid points is 120^3. The domain size is therefore $15cm \times 15cm \times 15cm$. For a droplet concentration of $\approx 50cm^{-3}$, the total number of droplets is ≈ 170000. This implies that, on average, only one grid point in ten contains a droplet. The models are integrated for $200s$ in each experiment and the domain undergoes adiabatic cooling with a rate consistent with a constant updraft of $2.5ms^{-1}$. The cloud droplets at initial time are distributed randomly in space except for Experiment N01, where they are uniformly distributed. Because sedimentation is not included in Experiments N01 to N09, the droplets in these experiments are basically frozen in space throughout the duration of the integration.

Expt #	N01	N02	N03	N04	N05	N06	N07	N08	N09	N10
# of gridpoints	120^3	120^3	120^3	120^3	120^3	120^3	120^3	120^3	120^3	120^3
$\Delta x(mm)$	1.25	1.25	1.25	1.25	1.25	1.25	1.25	1.25	1.25	1.25
$\Delta t(ms)$	10	10	10	10	10	10	10	10	10	10
duration(s)	200	200	200	200	200	200	200	200	200	200
concentration (cm^{-3})	51	51	51	51	51	51	51	51	51	51
$\overline{^0R}(\mu m)$	10	10	10	10	10	10	15	10	5	10
$\sigma(^0R)(\mu m)$	2.9	0	.15	0.5	1.0	2.9	0.	0.	.0	2.9
updraft(ms^{-1})	2.5	2.5	2.5	2.5	2.5	2.5	2.5	2.5	2.5	2.5
sedimentation	no	no	no	no	no	no	no	no	no	yes

Table 6.1: Basic parameters of experiments without turbulence

We would explore the effect of a variety of initial size distributions. They include the very narrow monodispersed distribution, the broader Gaussian distributions with different widths, and the very broad uniform distribution. The monodispersed spectrum and the broad uniform spectrum can be regarded as the two extremes while the Gaussian distributions lie somewhere in between. A uniform deviate random number generator which generates a real number within a specified interval with uniform probability is used for the uniform distribution and the initial positions of the droplets. A Gaussian deviate random number generator, which generates a real number according to a Gaussian probability distribution with a specified mean and a specified standard deviation, is used to yield the Gaussian size spectra.

Experiments N01 and N02 constitute two extreme cases. In N01, the initial size spectrum is broad. The number density of the droplet sizes is uniform in the interval between 5 to $15\mu m$ in radius. The droplets are placed evenly in space with one droplet in every 10^{th} grid cell such that they form a regular cubical grid. Experiment N02 starts with a monodispersed spectrum. The droplets are distributed randomly in space but they have the same size which is $10\mu m$ radius. The mean sizes of the droplets in N01 and N02 are therefore identical.

Experiments N03 to N06 are designed to study the effect of varying the initial size distributions which have the same mean radius but increasing standard deviations. Gaussian distributions with various widths characterize the initial spectra in the first three runs while a uniform distribution from 5 to $15\mu m$ in radius is used in N06. Even though very large and very small drops are theoretically possible in the Gaussian distributions, in practice the finite number of droplets in the domain ($\approx$ 170000) results in a truncated spectrum in N03-N05. Specifically, the radius of the smallest and the largest droplets in μm at initial time for N03, N04, and N05 are [9.3,10.7], [7.7,12.4], and [5.5,14.7] respectively.

Experiments N07-N09 compare the results for three different monodispersed spectra, whose initial radius decreases from 15 to $5\mu m$. Finally, N10 examines the effect of sedimentation using the same broad initial size distribution as in N06.

In the analysis of the results, we are interested in the difference between the *microscopic* and the *macroscopic* models, particularly in the rate of growth of individual droplets and the evolution of the width of the size spectra. In this context, it is important to bear in mind that supersaturation affects directly the rate of droplet growth. Furthermore, the parameter $\mathcal{J}_i'^2$, the perturbation degree of growth (see Section 5.6), is proportional to the time integral of the supersaturation perturbation for droplet i. It is a key parameter which determines whether the radius of individual droplets would differ in the *microscopic* and the *macroscopic* approach.

The evolution of the size distribution in the *microscopic* model with respect to that of the *macroscopic* model is analysed both in terms of the difference in the standard deviation, $\sigma(R) - \sigma(R_M)$, and in terms of the difference in the variance of the squared radius, $V({}^tR^2) - V({}^0R^2)$ (see (5.14)). As discussed in Section 5.6 the sign of these quantities is the same and thus both quantities can be used to diagnose spectral broadening or narrowing. We will pay special attention to the terms appearing on the right of (5.14). These terms have a physical meaning (Section 5.6) which facilitates the analysis of spectral changes.

We will focus on these parameters in our analysis and make reference to Table 6.2 which contains a summary of the important results at the end of the experiments (200 s).

Fig. 6.1 shows the temporal evolution of the difference in standard deviation of the size distribution between the *microscopic* and *macroscopic* models ($\sigma(R) - \sigma(R_M)$) for N01 and N02. In N01 (curve A), the standard deviation of the size distribution from the *microscopic* approach is $\approx 2\%$ smaller than that from the *macroscopic* approach

at 200s. In other words, the *microscopic* spectrum is narrower than the *macroscopic* spectrum when the droplets are not distributed randomly in space. A curve labeled "0" is also plotted. It represents the result of a hypothetical experiment where equal-sized droplets are distributed evenly in space. Curve "0" and curve A showed that the *microscopic* spectrum is always narrower than the *macroscopic* spectrum for uniformly spaced droplets. Indeed, the two curves delineate the range for spectral narrowing for droplets distributed uniformly in space in a non-moving medium. In contrast to N01, broadening occurs in N02 (curve B) where the standard deviation $\sigma(R)$ of the spectrum increased from 0. to .15 μm.

The difference in the width of the spectrum between N01 and N02 is related to the temporal evolution of the terms on the right of (5.14) (see Fig. 6.2). The curves for $V(\beta'^2)$ and $2cov(\beta'^2, {}^0R^2)$ are denoted by small and capital letters respectively. The term $V(\beta'^2)$, which is positive and has a broadening effect on the spectra, is much larger in N02 (curve b) than in N01 (curve a), reaching values of 1.7 and $31.6\mu m^4$ respectively at 200 s. The dispersion of the degree of growth is given by $\sigma(\beta'^2)/\beta_M^2 \times 100$. (see (5.17) for derivation). The *macroscopic* degree of growth β_M^2 depends only on the change in the mean squared radius of the spectrum (see Section 5.6), and is approximately $233\mu m^2$ in both experiments. Using this value for β_M^2, the dispersion of the degree of growth turns out to be .572% for N01 and 2.47% for N02.

In contrast to the behavior of the $V(\beta'^2)$ term, the $2cov(\beta'^2, {}^0R^2)$ term is zero for N02 (not shown) but is large and negative at all times for N01 where the correlation between β'^2 and ${}^0R^2$ reached a value of $-.86$ at 200 s.

The much larger broadening effect observed in N02 is reflected in the probability distribution of supersaturation perturbations at 200 s (Fig. 6.3). When compared to the results of N01 (not shown), the standard deviation of the probability distribution for N02 ($.156 \times 10^{-3}$) is almost one order of magnitude larger than that in N01 ($.23 \times 10^{-4}$). The dispersion of the supersaturation perturbation at 200 s, calculated

from $\sigma(S')/S_M \times 100.$ (see (5.17) for derivation) with the *macroscopic* supersaturation S_M at about $.54 \times 10^{-2}$ for both experiments, turns out to be 0.434% and 2.89% for N01 and N02 respectively. The maximum and minimum supersaturation perturbations in N02 correspond to deviations of 11 and -15% ($S'/S_M \times 100.$) from the *macroscopic* supersaturation. In contrast, the maximum and minimum supersaturation perturbations in N01 correspond to deviations of only $\pm 1.3\%$ from the *macroscopic* supersaturation (not shown).

Note that the distribution of S' is not symmetric but rather negatively skewed. Furthermore, the probability distributions for temperature and water vapor mixing ratio (not shown) are also skewed. The skewness is positive for the former and negative for the latter. These asymmetries are directly related to the fact that the droplets are randomly distributed and therefore the concentration of droplets follows the Poisson distribution which is positively skewed (see Appendix A). In other words, the tail of the Poisson distribution towards high concentration of droplets is responsible for the positive skewness of temperature and the negative skewness of the water vapor mixing ratio which result in a negative skewness for the supersaturation perturbation. Subsequently, the distribution of β'^2 is also negatively skewed.

The results of N01 and N02 showed that non-uniform distribution of the initial size of droplets and their position lead to variation in supersaturation. However, the dispersion of the distribution of supersaturation perturbation is much wider in N02 than in N01, indicating that the random position of the droplets provides a larger forcing for supersaturation perturbation than the initial variability in droplet radius. We will provide an explanation for this in Section 6.1.

Returning to the covariance term plotted in Fig. 6.2. It was shown that this term is large and negative for N01 and thus has a dominating narrowing effect on the spectrum. The correlation between β'^2 and ${}^0R^2$ is negative, indicating that droplets initially smaller than the average size would tend to grow faster (subject to a positive

supersaturation perturbation) and droplets initially larger than the average size would grow more slowly (subject to a negative supersaturation perturbation). To clarify this point, we plotted in Fig. 6.4 the contribution of droplets of various sizes to the total correlation between β'^2 and ${}^0R^2$. To construct this figure, we first sorted the $\approx$ 170000 droplets according to sizes in groups of 1000. The correlation is then calculated for each group and plotted with the mean radius of each group along the abscissa . It is clear that the further the mean radius of the group deviates from the mean radius of the total population ($10\mu m$), the greater is its contribution to the total negative correlation.

The reason for this increasing contribution is attributable to the fact that in the *microscopic* approach, condensation affects the temperature and water vapor distribution in the environment of individual droplets. Since the release of latent heat (with the accompanying decrease in water vapor mixing ratio) is proportional to the size of the droplet (see equations (4.12), (4.13) and (4.3)), a drop which is smaller (larger) than the average size would develop in an immediate environment which is colder (warmer) and moister (drier) than that in the *macroscopic* approach. This interpretation is supported by the results of an experiment similar to N01 but with droplets of only two sizes (5 and 15 μm) distributed uniformly in space. Fig. 6.5 shows the time series of the supersaturation perturbation (top panel), the perturbations for temperature and water vapor mixing ratio for the large droplet (middle panel) and the small droplet (bottom panel). The temperature perturbation and water vapor perturbation are respectively positive (negative) and negative (positive) for the large (small) droplet. The supersaturation perturbation is therefore negative (positive) for the large (small) droplet.

To examine the effect of the *microscopic* approach on individual droplets, we plotted in Fig. 6.6 the probability distribution (in % of total number of droplets) for ${}^tR - {}^tR_M$ at $200s$ for experiments N01 (top panel) and N02 (bottom panel). In N01,

curve c denotes the probability distribution for all droplets while curves a and b represent respectively those for the initially 10% smallest and 10% largest droplets. It is obvious that the smallest droplets tend to grow faster than their *macroscopic* counterparts (positive ${}^tR - {}^tR_M$) while the largest droplets tend to grow slower. The extrema in ${}^tR - {}^tR_M$ are .10 and $-.13\mu m$. In N02, the distribution is much wider with extrema of .842 and $.56\mu m$. These extrema are upper bounds to how much larger the largest droplet of the size distribution and how much smaller the smallest droplet of the size distribution can be in the *microscopic* approach relative to the *macroscopic* approach. Contrasting the results for N01 and N02, the effect of the non-uniformity in the spatial distribution of droplets becomes quite clear. Also note that similar to the instantaneous supersaturation perturbation and the perturbation degree of growth, the distribution for ${}^tR - {}^tR_M$ is again negatively skewed.

Having seen that spectral broadening can occur when droplets are distributed randomly in space and spectral narrowing can take place for spatially uniform droplets whose size distribution is broad, we now explore the sensitivity of the results to the initial widths of the size distribution in experiments N03 to N06 (see Table 6.1). The widths of the size distributions increases from N03 to N05. They are generated by a Gaussian random number generator. In N06, the size distribution is uniform. The initial mean radius for these distributions remains constant at $10\mu m$.

Fig. 6.7 shows the temporal evolution of $\sigma(R) - \sigma(R_M)$ for these four experiments. Clearly, whether the *microscopic* spectrum broadens with respect to the *macroscopic* spectrum depends on the width of the initial spectrum and also on time. Curve C, for a Gaussian size distribution with an initial standard distribution of $.15\mu m$, shows a spectrum which narrows for a few seconds and then broadens. At the end of the experiment, $\sigma(R)$ is 116% greater than $\sigma(R_M)$. Curves D and E indicate spectra which narrow for the first 30 and 110 seconds respectively and then they broaden. At the end of N04 and N05, $\sigma(R)$ is greater than $\sigma(R_M)$ by 14 and 2%

respectively. The widest initial size distribution narrows with respect to the *macroscopic* spectrum throughout the duration of the experiment and is 1.4% narrower at 200 s.

Fig. 6.8 shows the temporal evolution of the terms appearing in (5.14) for N03-N06. Even though $\sigma({}^0R)$ increases from N03-N06, the values for $V(\beta'^2)$ (curves c, d, e, f) are similar for these four size distributions with the same initial mean radius. However, curves C to F clearly indicate that the magnitude of the $2cov(\beta'^2, {}^0R^2)$ term is an increasing function of the initial standard deviation of the size distribution. The sum of the two terms (not shown) show that the R^2 spectra first narrows and then widens. In particular, the wider an initial distribution the longer it takes the R^2 spectrum to widen beyond its initial variance.

The next three experiments (N07-N09) have monodispersed initial size distributions with ${}^0R = 15, 10$ and $5\mu m$ respectively. Fig. 6.9 shows the temporal evolutions of the standard deviation , $\sigma(R)$ (top panel), and $V(\beta'^2)$ (bottom panel). We see that the increases in the standard deviation and $V(\beta'^2)$ become larger when the initial sizes of the droplets becomes smaller. In these simple experiments, where the positions of the droplets remain frozen, the variance of the supersaturation perturbations follows the same trend. However, the *macroscopic* supersaturation also increases as a function of decreasing initial size, thus the dispersions of the distributions of S and β^2 actually decrease slightly. The standard deviations of ${}^tR - {}^tR_M$ for N07-N09 at 200s are .13, .15 and $.17\mu m$ respectively, following the same trend as $V(\beta'^2)$.

We now explore the effect of the sedimentation on spectral evolution. Experiment N10 has the same initial conditions as N06 except that the sedimentation of droplets at their terminal fall speeds is allowed. The initial size of the droplets for N10 vary from 5 to $15\mu m$, and the corresponding initial terminal velocities range from .3 to $2.7 cm s^{-1}$ (see Table 2.2). In previous experiments, the droplets grew in an environment where the concentration of droplets in the immediate surrounding remains

constant. As a result, the supersaturation perturbations varied slowly and smoothly. When the droplets sediment, this is no longer the case. Fig. 6.10 compares the temporal evolution of the supersaturation perturbation for several droplets in N10 and in N06. Because of sedimentation, the droplets in N10 grow in a much more variable environment where growth varies rapidly between favorable (positive perturbation) and unfavorable (negative perturbation) conditions.

The average time that a droplet stays in similar conditions can be estimated from the decorrelation time, calculated from the autocorrelation coefficient of the supersaturation perturbation as a function of lag time. The decorrelation time can be loosely defined as the time lag at which the autocorrelation coefficient approaches zero. In all experiments without turbulence and sedimentation, the decorrelation time of the supersaturation perturbation is very long (order of minutes). Therefore, the probability distribution of the time integral of the supersaturation perturbation, which yields the perturbation degree of growth β'^2, has similar properties as that of the instantaneous supersaturation at the end of experiments (e.g. the dispersion and the maximum and minimum relative to the *macroscopic* quantity, refer to Table 6.2).

Fig. 6.11 shows the autocorrelation coefficient of S', averaged over 2000 droplets, as a function of the lag time. Comparing the two curves, it can be seen that sedimentation substantially reduces the decorrelation time of the supersaturation perturbations. For the particular size distribution in N10, the droplets will grow in similar conditions for an average of $4-5$ seconds. Fig. 6.12 shows the probability distribution of $100. \times \frac{S'}{S_M}$ every $40s$ for the same experiment. The distribution changes with time, particularly for the negative tail. The dispersion of this distribution varies between .015 and .019 while the extrema vary around $-10.$ and 6.%. These values are ≈ 35 to 50.% smaller than those for experiment N06.

The decrease in the dispersion of the supersaturation perturbation distribution in N10 is directly related to the decrease in the standard deviations of temperature and

water vapor mixing ratio perturbations. The standard deviation of the temperature perturbation is reduced from $.14 \times 10^{-2}$ to $.87 \times 10^{-3}$ K, while that of the water vapor mixing ratio decreases from $.5 \times 10^{-6}$ to $.3 \times 10^{-6}$. In regions void of droplets strong negative temperature and positive water vapor mixing ratio perturbations can develop (consider (4.20) and (4.21) with $C_d = 0$) Furthermore, in regions of high droplet concentrations strong positive temperature and negative water vapor mixing ratio perturbations can develop (consider (4.20) and (4.21) with $C_d > C_{dM}$). The decrease in the standard deviations of the scalar fields can be explained by the fact while the droplets fall at their various terminal velocities they sweep the volume such that no region will stay void of droplets indefinitely and the configuration of droplets changes such that regions of high droplet concentration also do not survive indefinitely.

The evolution of the spectra can be examined from the curves plotted in Fig. 6.13. It is apparent that sedimentation has an important impact on the variance of the perturbation degree of growth ($V(\beta'^2)$), reducing it from $32.5\mu m^4$ in N06 to $3.8\mu m^4$ in N10. The dispersion of β^2 is reduced to .008 (compared to .025 in N06) and the ratios $\frac{\beta'^2_{min}}{\beta^2_M}$ and $\frac{\beta'^2_{max}}{\beta^2_M}$ to $-4.$ and 3% respectively (compared to $-12.$ and 10% in N06). The other effect of sedimentation is to reduce the importance of the covariance term. The net effect is that $\sigma(R) - \sigma(R_M)$ is still negative at 200s in N10 but its magnitude is less than that in N06. In terms of the distribution of ${}^tR - {}^tR_M$, the standard deviation was reduced to $.05\mu m$ and the extrema to $\pm.22\mu m$.

Experiment N02 was also repeated by including sedimentation. Even though all droplets initially fall at the same speed, the final $V(\beta'^2)$ is still substantially reduced from $31.6\mu m^4$ to $8.1\mu m^4$. The final $\sigma(R)$ also decreased from .15 to $.08\mu m$. Thus the inclusion of sedimentation brings the *microscopic* results closer to the *macroscopic* results.

Two experiments similar to N02 but with concentrations of 75 and $100cm^{-3}$ were

also conducted to study the sensitivity to concentration. The results indicate a decrease in the variance of the perturbation degree of growth as a function of increasing concentration, indicating that the difference between the *microscopic* and *macroscopic* results becomes smaller when the concentration increases. Experiments with concentration higher than $100cm^{-3}$ was not attempted because with a finite grid size, the problem of adequately resolving the distance between individual droplets worsens as the concentration becomes progressively larger. Nevertheless, the results so far obtained makes physical sense because when the average distance between the droplets gets smaller with higher concentration, molecular diffusion becomes more efficient in reducing the supersaturation perturbations.

Expt #	N01	N02	N03	N04	N05
$\sigma(R)(\mu m)[V(R^2)(\mu m^4)]$	1.54[3259.]	.154[31.6]	.177[41.9]	.309[129.]	.555[418.]
$\sigma(R_M)(\mu m)[V(R_M^2)(\mu m^4)])$	1.57[3388.]	.0[.0]	.082[8.98]	.272[99.9]	.543[401.]
$V(\beta'^2)(\mu m^4)$	1.75	31.6	33.3	33.4	33.5
$2cov(\beta'^2, {}^0R^2)(\mu m^4)$	-132.	0.	-.379	-4.12	-16.4
$\sigma(\beta'^2)/\beta_M^2(\%)$	.572	2.41	2.43	2.42	2.44
$\sigma(S')/S_M(\%)$	.434	2.89	2.89	2.90	2.90
Expt. #	N06	N07	N08	N09	N10
$\sigma(R)(\mu m)[V(R^2)(\mu m^4)]$	1.55[3290.]	.134[29.9]	.155[32.4]	.169[35.4]	1.55[3312.]
$\sigma(R_M)(\mu m)[V(R_M^2)(\mu m^4)])$	1.57[3388.]	.0[.0]	.0[.0]	.0[.0]	1.57[3388.]
$V(\beta'^2)(\mu m^4)$	32.6	29.9	32.4	35.4	3.76
$2cov(\beta'^2, {}^0R^2)(\mu m^4)$	-130.	.0	.0	.0	-79.4
$\sigma(\beta'^2)/\beta_M^2(\%)$	2.47	2.85	2.40	2.07	.84
$\sigma(S')/S_M(\%)$	2.90	3.17	2.88	2.76	1.86

Table 6.2: Important variables at final time for experiments without turbulence

6.1 Comparison with the analytical predictions of Srivastava (1989)

Srivastava's (1989) analytical approach led to some specific qualitative and quantitative predictions for the supersaturation perturbations for a frozen configuration of droplets (no sedimentation and no turbulence). He derived the following equation for the ratio of the supersaturation perturbation over the *macroscopic* supersaturation:

$$\frac{S'}{S_M} \approx 12l^{1/3}\left[(\frac{v}{\overline{v}})^{2/3} - \frac{R}{\overline{R}}(\frac{\overline{v}}{v})^{1/3}\right]. \tag{6.1}$$

where l is the cloud water content expressed as a volume fraction, v is the "volume occupied" by an individual droplet, and $\overline{v}$ is the average volume occupied by each droplet (given by the reciprocal of the concentration). It is assumed that the volumes are distributed randomly and obey the Poisson statistics. Several qualitative results can be deduced from this equation:

i) for a droplet of average radius, $\overline{R}$, occupying an average volume, $\overline{v}$, the supersaturation perturbation is zero

ii) if a droplet occupies the average volume $\overline{v}$, its supersaturation perturbation will be positive (negative) if its size is smaller (larger) than average.

iii) if a droplet of average size $\overline{R}$ occupying a smaller (larger) volume than average, it will experience a negative (positive) supersaturation perturbation

We can compare Srivastava's results with those from our numerical experiments presented in Fig. 6.6 which displays the probability distribution of ${}^tR - {}^tR_M$ for the smallest 10% (curve *a*) and the largest 10% (curve *b*) of the droplets in experiment N01. Recall that in this experiment, the droplets are uniformly distributed in space but the initial size distribution is very broad. It is evident that in agreement with Srivastava's result (ii), the smallest (largest) droplets do, on the average, grow faster

(slower) than their *macroscopic* counterparts. However, Fig. 6.6 also shows that the analytic results have certain limitations. For instance, results (i) and (iii) listed above may not necessarily be true for an individual droplet because the supersaturation in the immediate environment of the droplet does not depend solely on its size but also on the sizes and positions of the surrounding droplets through the action of molecular diffusion.

As a specific example, we will estimate the dispersion of the distribution of supersaturation perturbation from (6.1)and compare the analytical and numerical results for two simple situations where the droplets are uniformly distributed in space (N01) and where the size distribution is monodispersed (N02). In the former case, the "volume occupied" by all droplets is the same and equals $\overline{v}$. The analytic dispersion $\sigma(S')/S_M \approx 12l^{1/3}\sigma(R)/\overline{R}$. Using $\sigma(R) \approx .09$ and $l \approx 1g/kg$ at the end of N01, the analytic dispersion in the supersaturation perturbation turns out to be 1.1%. In contrast, the numerical results obtained was .43% (see Table 6.2). For the case where the droplets are randomly distributed in space and the size distribution is monodispersed, using a probability density of v given by $p(v) = (1/\overline{v})exp(-v/\overline{v})$, the dispersion of (6.1) can be shown to be $\sigma(S')/S_M \approx 17.4l^{1/3}$. Using the values from N02 at 200 s, the analytic dispersion can be calculated to be 18%. The numerical result, however, is only 2.9% (see Table 6.2).

The values for $\sigma(S')/S_M$, evaluated from the analytic and numerical solutions, are much larger in N02 than in N01. This result is directly related to the fact that $\sigma(R)/\overline{R} \ll 1$ for N01 and N02, whereas $\sigma(v)/\overline{v} = 1$ in N02. In fact, comparing the expressions for the two cases indicates that this result will always hold unless the dispersion of the size distribution exceeds one. In nature, the observed dispersion of the size distribution of cloud droplets in adiabatic cloud cores is much smaller than one (e.g., see Jensen et al. 1985). Thus the non-uniformity in the spatial distribution can be expected to produce greater variability in the supersaturation perturbation

than the variability in the initial size distribution of the droplets.

We showed in this chapter that Srivastava's (1989) analytical estimates are qualitatively consistent with the results from our numerical experiments. However, the analytic results, in terms of the dispersion of the supersaturation perturbation, is considerably larger than those from the numerical experiments. Thus the assumptions required to yield the analytic solutions appear to lead to significant overestimates of the magnitude of the dispersion of the supersaturation perturbation.

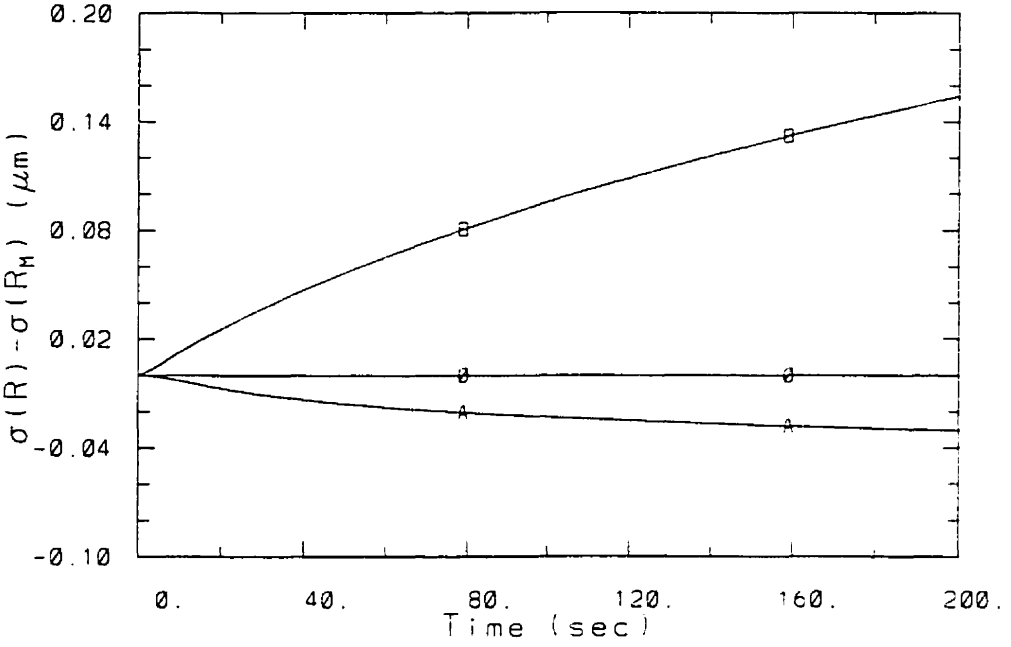

Figure 6.1: Temporal evolution of $\sigma(R) - \sigma(R_M)$ for experiments N01(curve A) and N02(curve B).

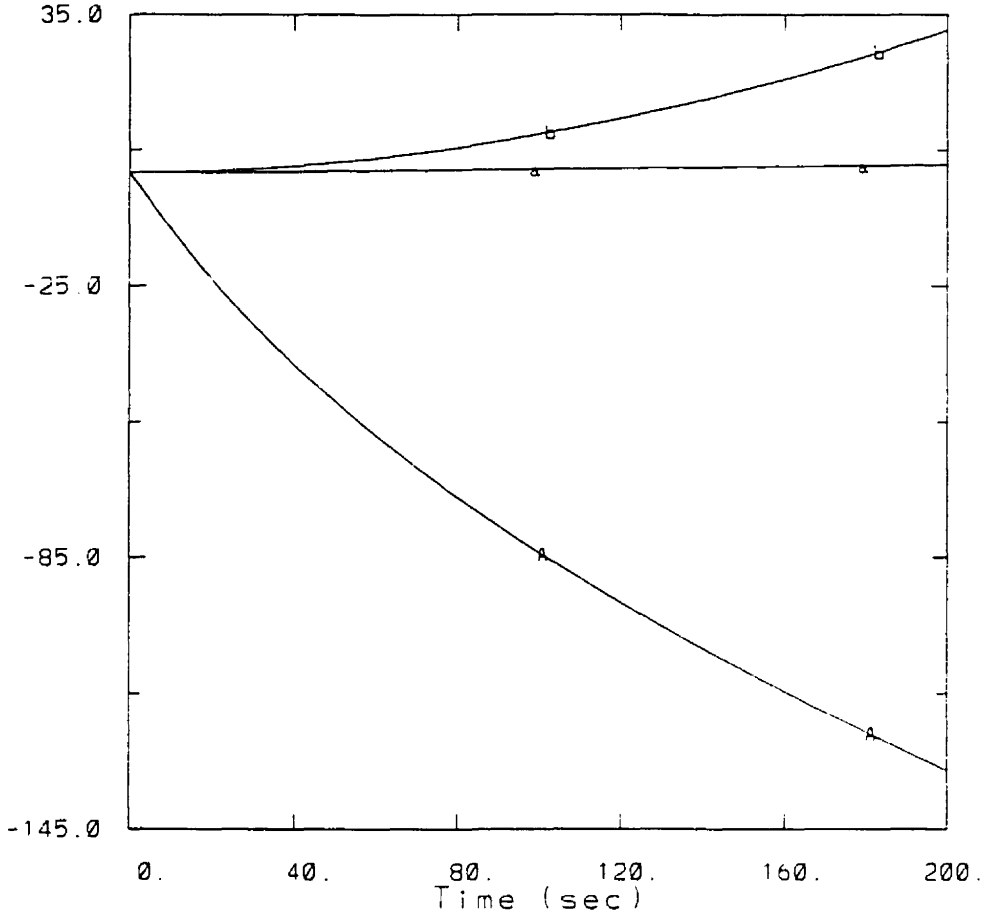

Figure 6.2: Temporal evolution of $V(\beta'^2)$ (small letters) and $2cov(\beta'^2, {}^0R^2)$ (capital letters) for experiments N01 (curves a and A) and N02 (curve b) . Units of ordinate are μm^4.

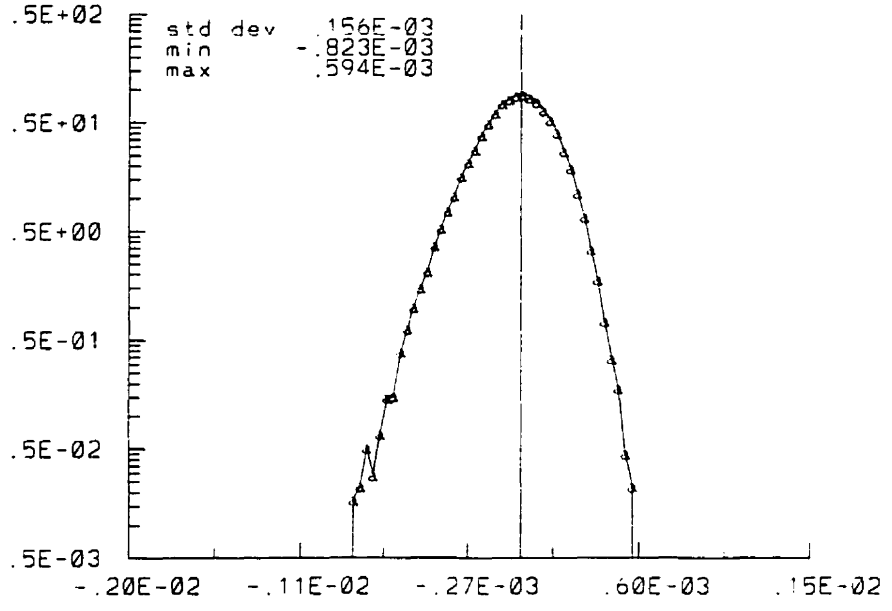

Figure 6.3: Probability distribution of supersaturation perturbations for experiment N02. Ordinate is the percentage of the total number of droplets while the abscissa is the supersaturation perturbation (S').

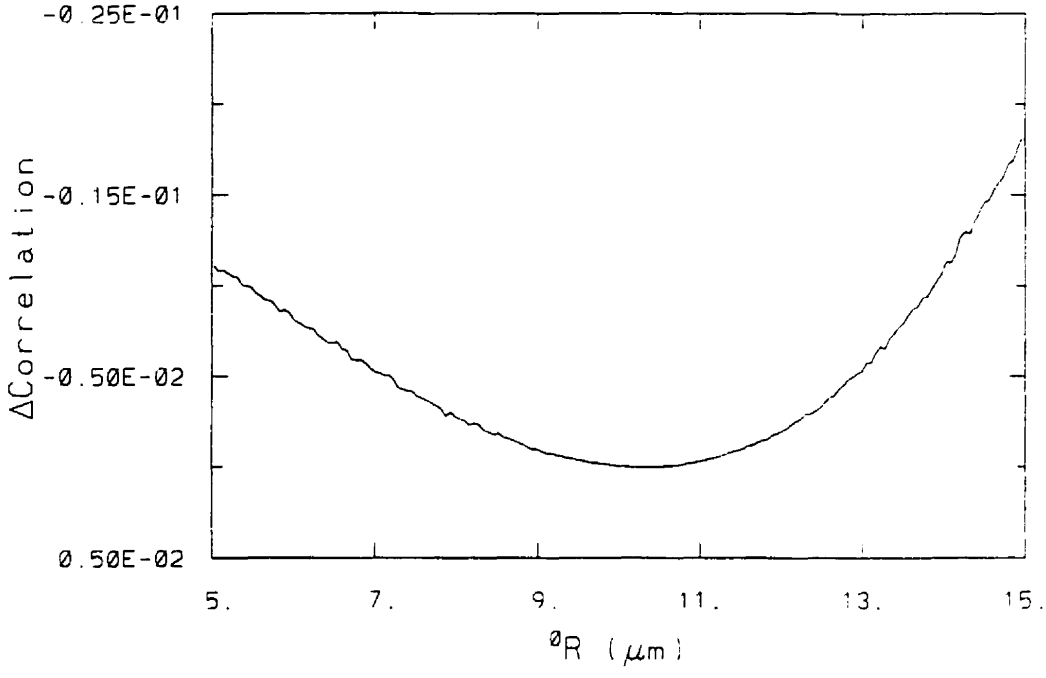

Figure 6.4: Contribution to correlation from groups of droplets sorted as a function of their initial size for $N01$

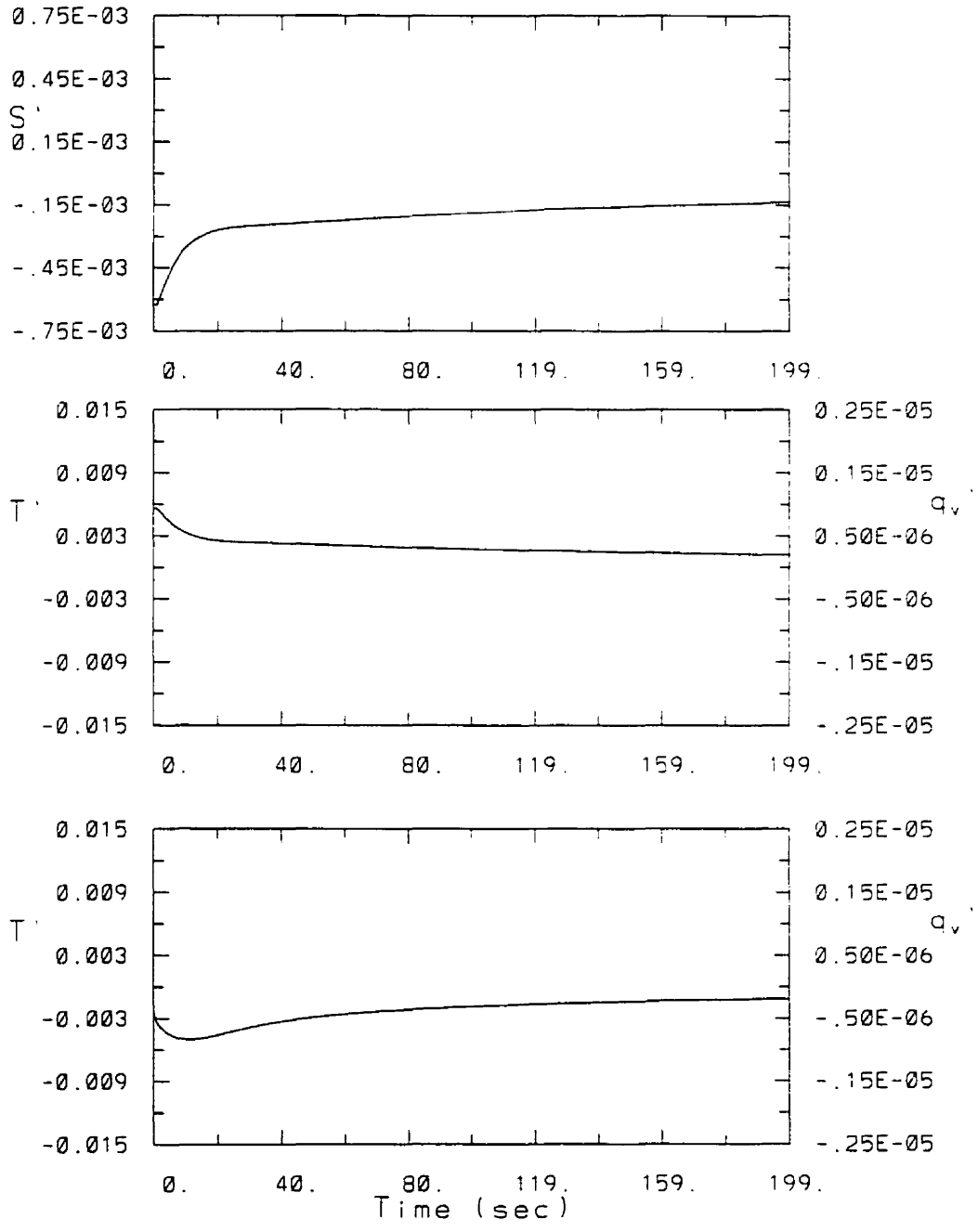

Figure 6.5: Top panel: temporal evolution of supersaturation perturbation for small droplet (dotted) and large droplet (solid). Middle panel: temporal evolution of temperature perturbation (solid) and water vapor mixing ratio perturbation (dotted) for large droplet. Bottom panel: temporal evolution of temperature perturbation (solid) and water vapor mixing ratio perturbation (dotted) for small droplet. Scale for temperature perturbation is on left and scale for water vapor mixing ratio perturbation is on right.

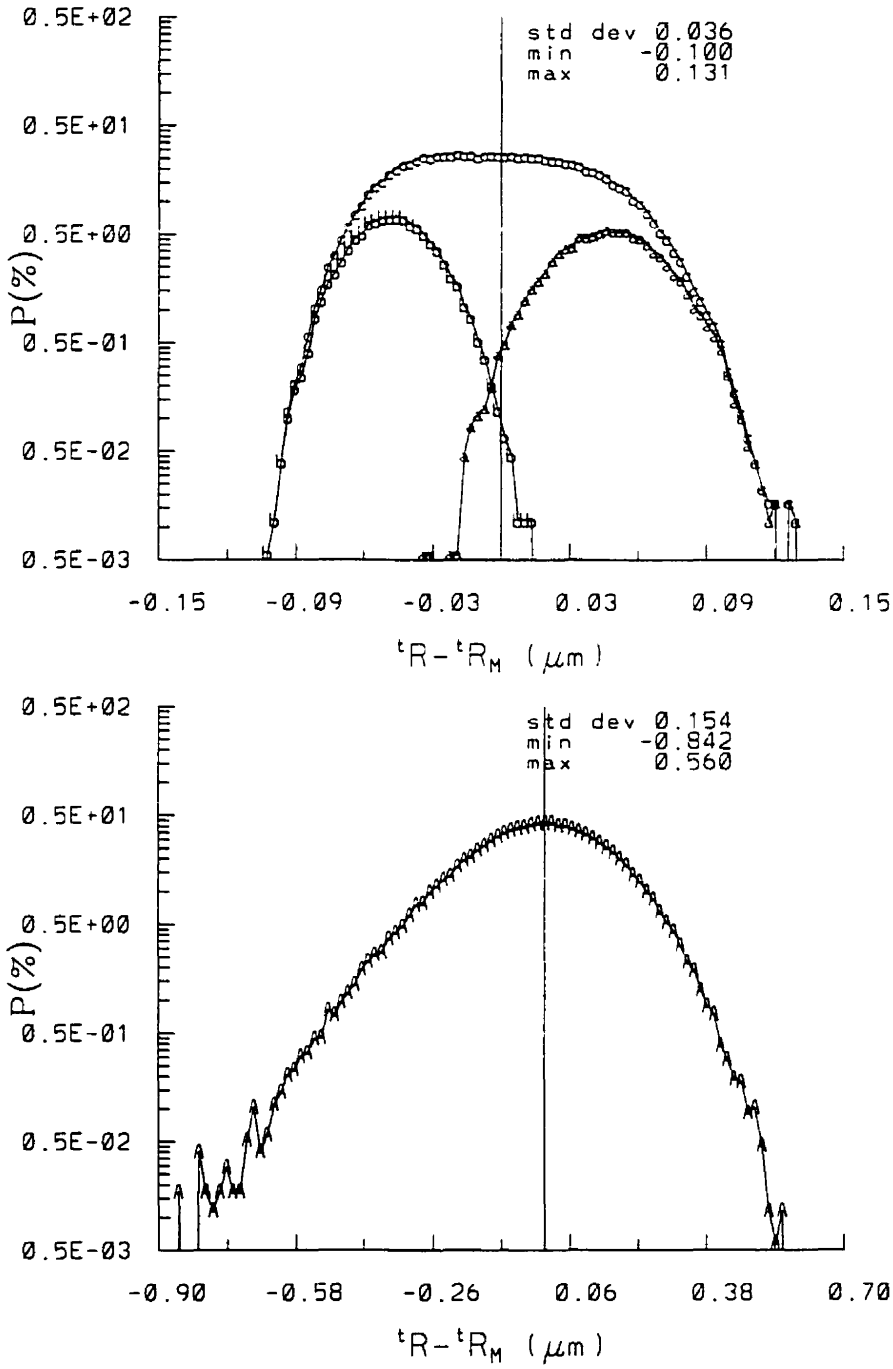

Figure 6.6: Probability distribution (in % of total number of droplets) of ${}^tR - {}^tR_M$ for experiments N01(top panel) and N02(bottom panel). In top panel, curve a is for the 10% initially smallest droplets, curve b for the 10% initially largest droplets while curve c is for all droplets.

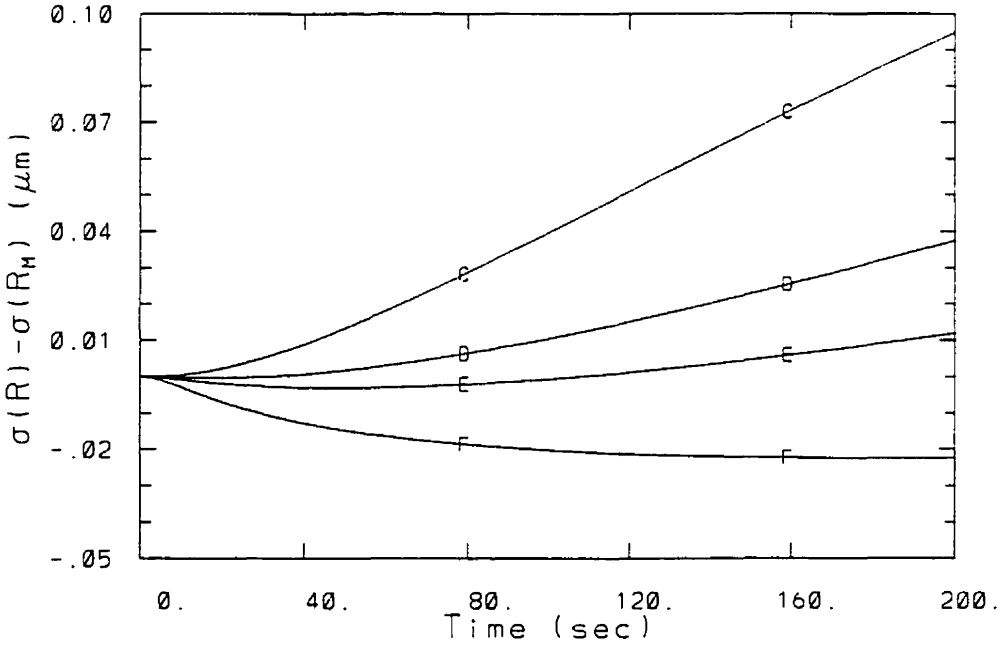

Figure 6.7: Temporal evolution of $\sigma(R) - \sigma(R_M)$ for experiments N03 (curve C) to N06 (curve F).

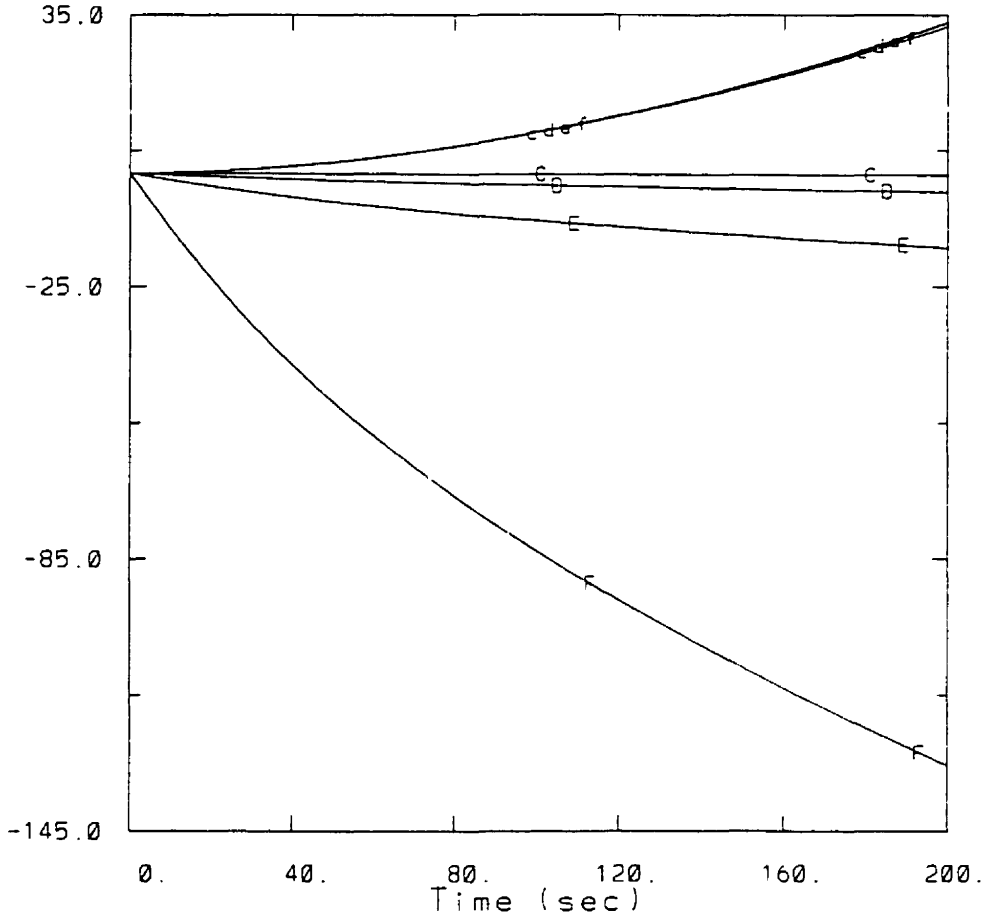

Figure 6.8: Temporal evolution of $V(\beta'^2)$ (small letters) and $2cov(\beta'^2, {}^0R^2)$ (capital letters) for experiments N03 (curves c and C) to N06 (curves f and F). Units of ordinate are μm^4

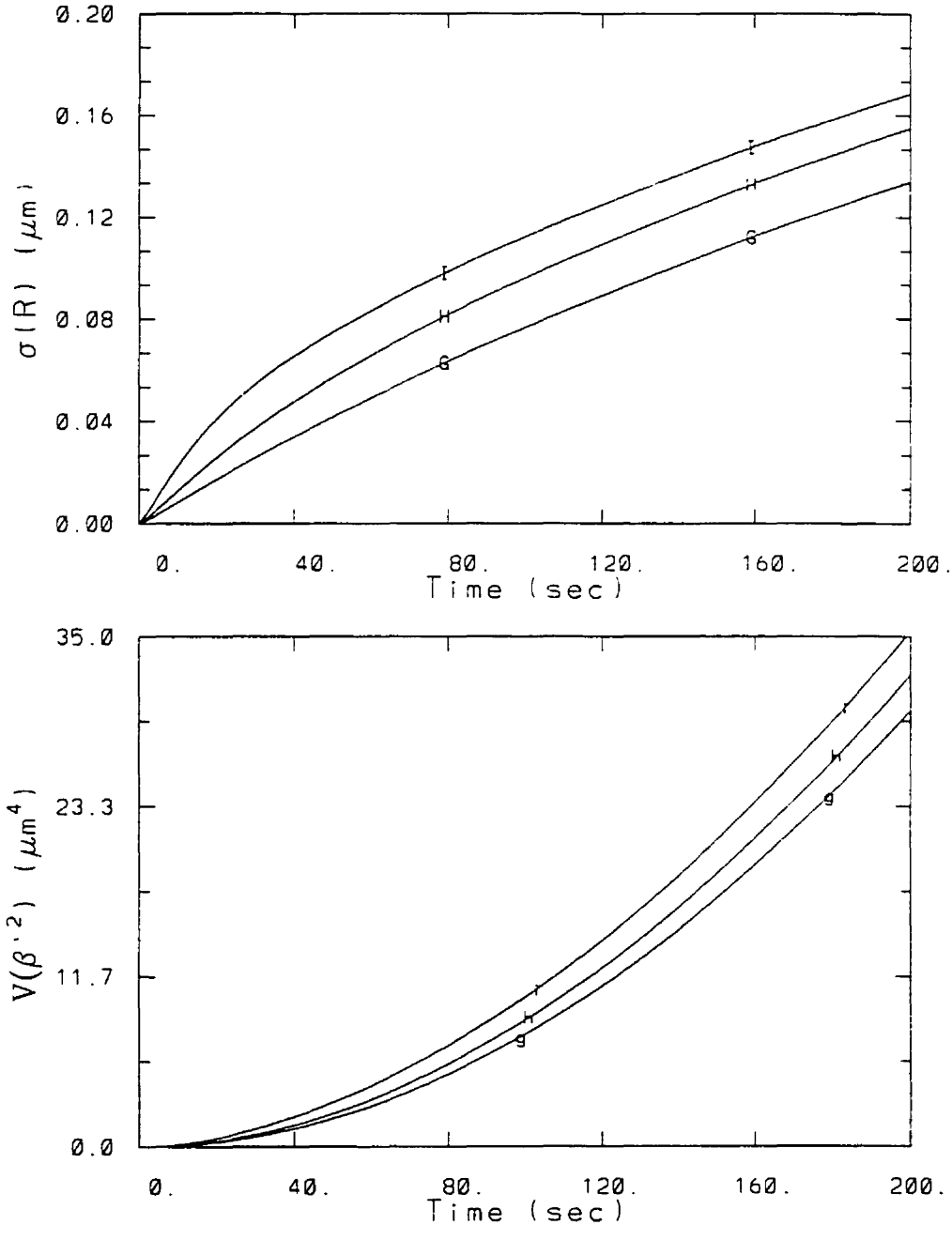

Figure 6.9: Top panel: temporal evolution of $\sigma(R)$ for experiments N07 (curve G) to N09 (curve I). Bottom panel: temporal evolution of $V(\beta'^2)$ for experiments N07(curve g) to N09 (curve i).

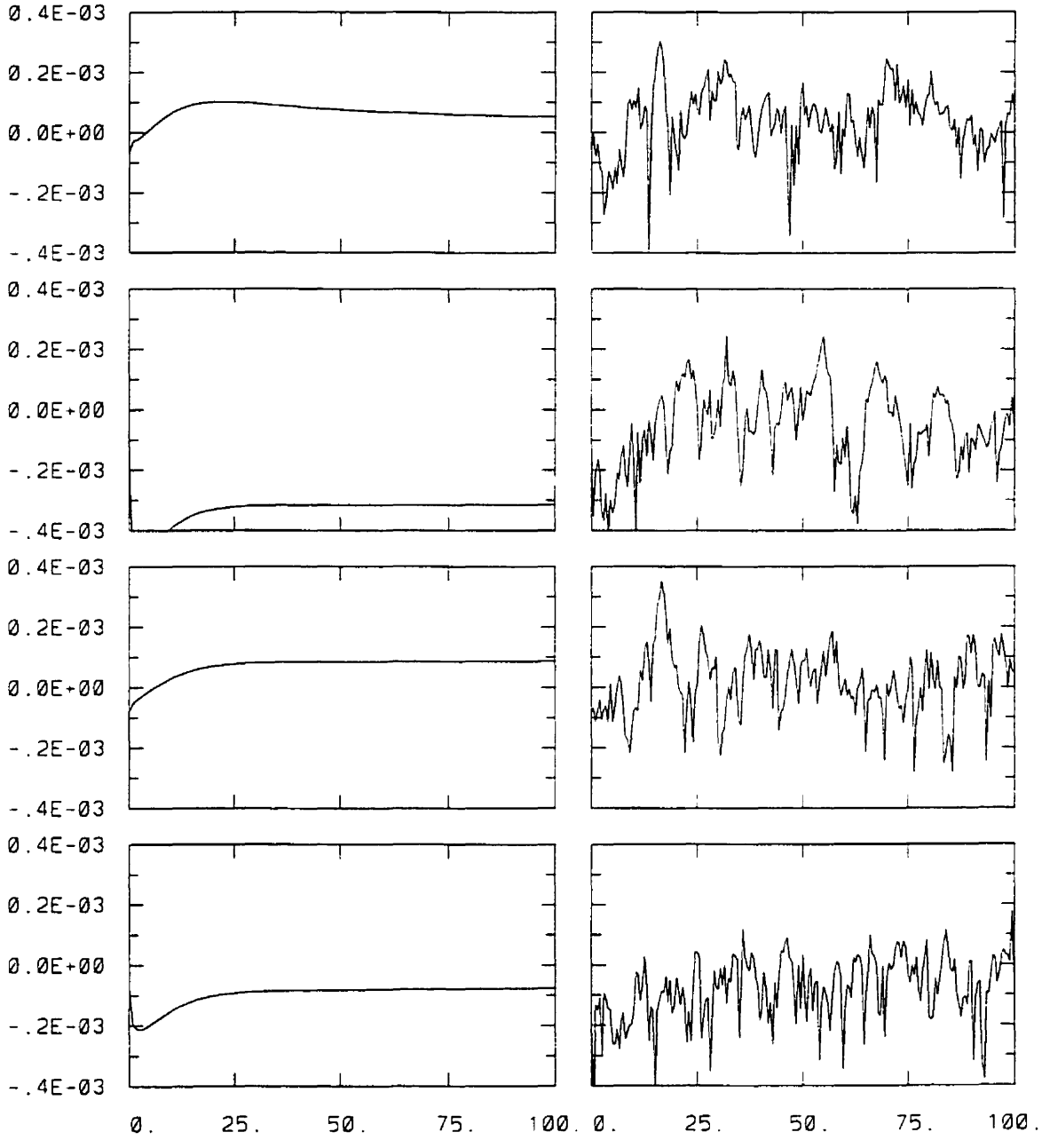

Figure 6.10: Temporal evolution over 100*sec* of the supersaturation perturbation (S') for four droplets in N06(left) and N10 (right).

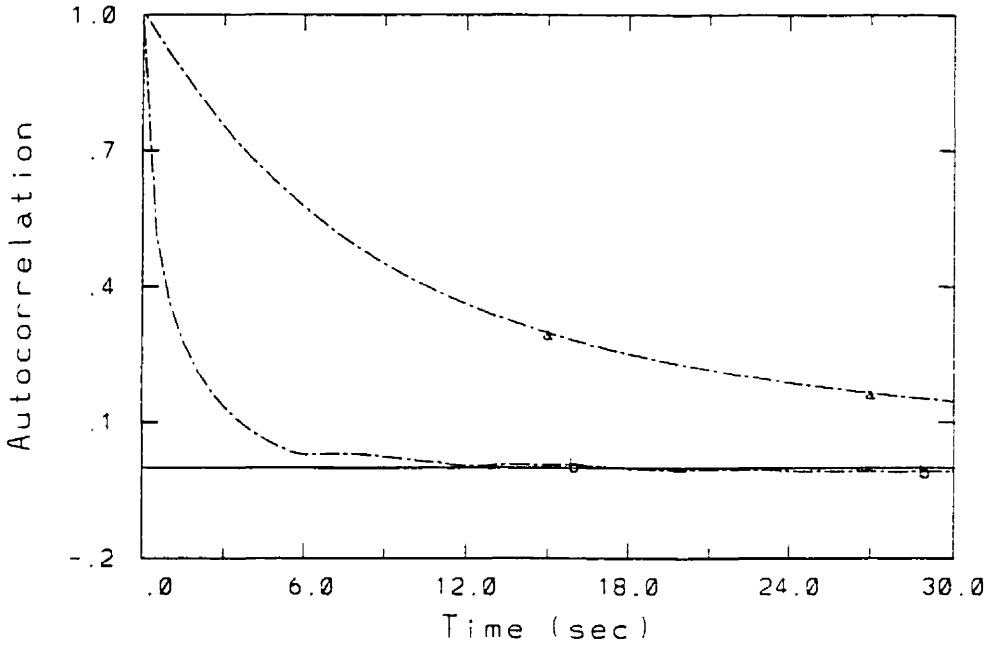

Figure 6.11: Autocorrelation, averaged over 2000 droplets, as a function of time lag for N06(curve a) and N10 (curve b). The horizontal line denotes zero autocorrelation.

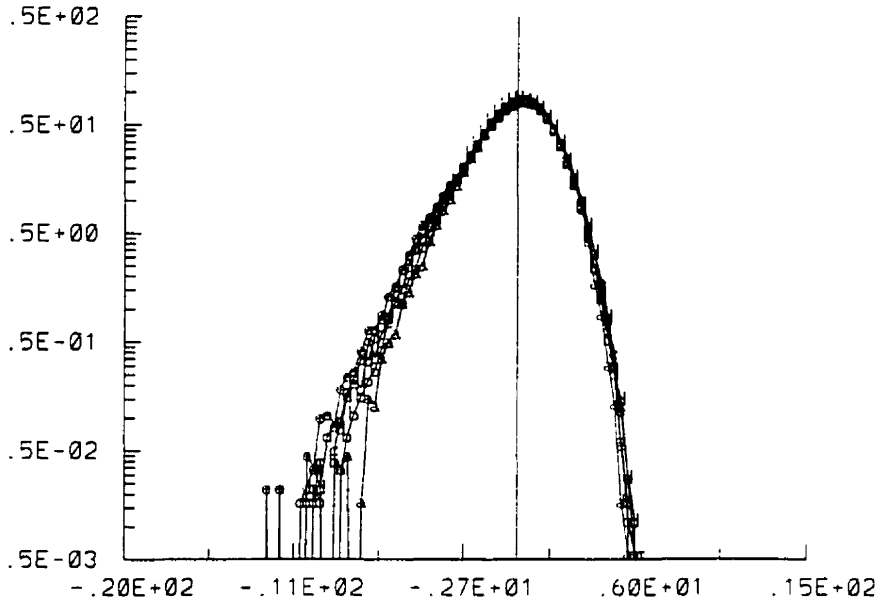

Figure 6.12: Probability distribution of 100. $\times \frac{S'}{S_M}$ every $40sec$ for experiment N10. Vertical axis is percentage of total number of droplets. The vertical line marks zero perturbation.

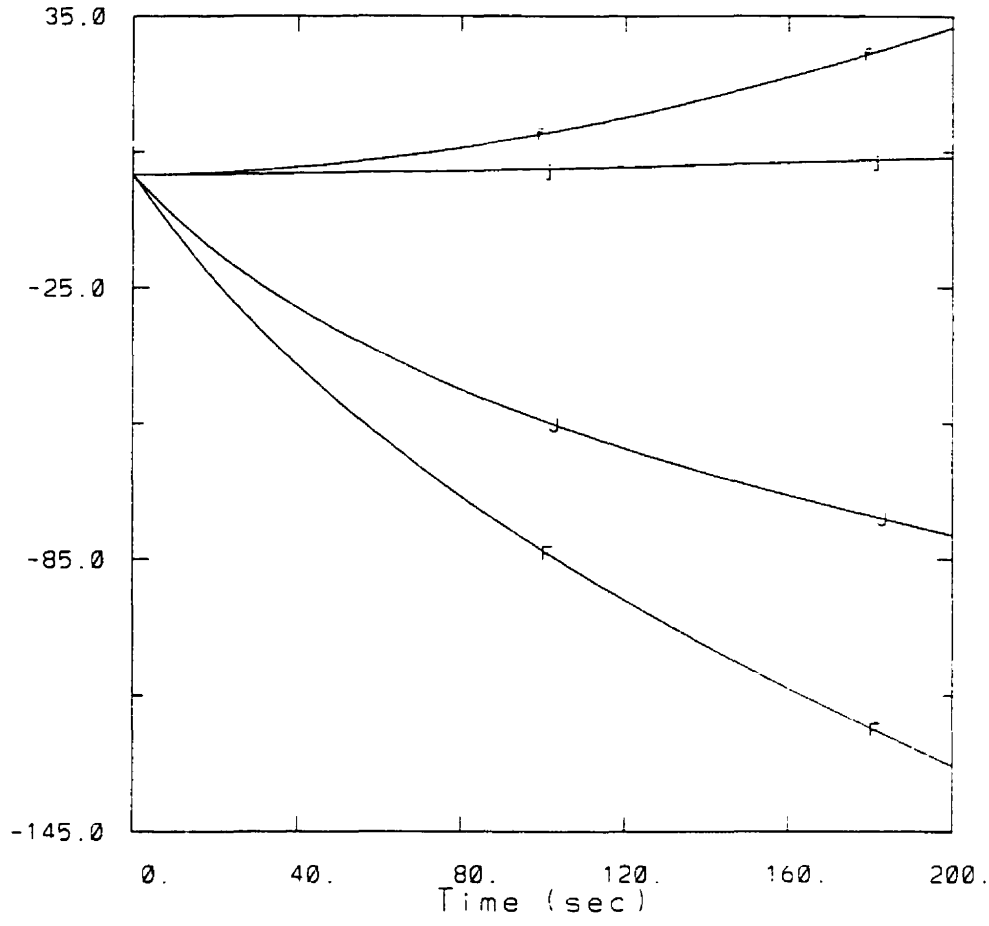

Figure 6.13: Temporal evolution of $V(\beta'^2)$ (small letters) and $2cov(\beta'^2, {}^0R^2)$ (capital letters) for experiments N06 (curves f and F) and N10 (curves j and J).Units of ordinate are μm^4

Chapter 7

Experiments with a turbulent flow

In this chapter, we will extend the results of Chapter 6 by introducing a turbulent flow field in a population of droplets. We will test three flow configurations which are well resolved realizations of statistically stationary, homogeneous and isotropic turbulence. To determine how turbulence affects the spatial distribution of the droplets and the evolution of the size spectra, we would carry out our investigation in several steps. First, we neglect the condensational growth of the droplets and examine the effects of drop inertia and sedimentation in a turbulent flow. Droplet growth by condensation is then allowed and the detailed development of the size spectra is studied. Sensitivity experiments are also conducted to examine the importance of adiabatic cooling due to the turbulent fluctuating vertical velocity (see (4.20)) and the feedback of latent heat release on the turbulent flow field.

7.1 Characteristics of the simulated flows

To save computer time, all simulations in this chapter are done using a volume with 80^3 grid points and a grid size of $.125cm$. The volume is thus $10 \times 10 \times 10cm^3$ which is smaller than the $15 \times 15 \times 15cm^3$ volume used for the experiments in Chapter 6. The

total number of droplets in the volume is proportionally reduced to 50000. We have carried out a few runs using 120^3 grid points and found that the results are similar to those obtained using 80^3 grid points. The other parameters that must be specified are the momentum viscosity coefficient ($1.6 \times 10^{-5}\ m^2 s^{-1}$), the forcing radius k_f which determines how many modes are forced, and the initial mean kinetic energy per unit mass.

We specified three values of the mean kinetic energy per unit mass to obtain three flow configurations. We forced 9 modes in the wavenumber range, $0 < |\mathbf{k}| < k_f = 1.5$. The initial kinetic energy is distributed among all the modes such that $E(|\mathbf{k}|) \propto exp^{-|\mathbf{k}|}$. The resulting eddy dissipation rates obtained for the three flow configurations are within the range of those measured in clouds. Once the flow simulation is started, the time evolution of the energy in all non-forced modes depends solely on molecular dissipation, the non-linear energy cascade, and any local sources or sinks of energy.

The three flow configurations, designated as *flowA*, *flowB* and *flowC*, correspond to an initial kinetic energy per unit mass of $.5 \times 10^{-3}\ m^2 s^{-2} kg^{-1}$, $2. \times 10^{-3}\ m^2 s^{-2} kg^{-1}$, and $8. \times 10^{-3}\ m^2 s^{-2} kg^{-1}$ respectively. To obtain a statistically stationary, homogeneous and isotropic flow, we integrated the turbulence model over ≈ 20 large eddy turnover times(τ_0). Fig. 7.1 shows that after several τ_0, the flow reaches a statistically stationary regime in the sense that the mean kinetic energy does not systematically increase or decrease with time but rather fluctuates about a constant value. Note that the duration of the integration is different for the three flows because τ_0 varies as a function of the mean kinetic energy of the flow. We consider that the flows have reached a statistically stationary state at the end of the simulations.

To examine whether the flows are isotropic, we follow Bartello et al. (1994), by examining the diagonal elements of the anisotropy tensor:

$$b_{ij} = < u_i u_j > / u^2 - \delta_{ij}/3.$$

where the angle brackets denote spatial averaging. Fig. 7.2 depicts the temporal evolution of the diagonal elements b_{11} , b_{22}, and b_{33} for *flowC*. Similar to the case for the mean kinetic energy, these components exhibit relatively large amplitudes but slow time fluctuations. However there is no systematic trend and their time means all approach zero, consistent with the behavior of statistically isotropic turbulence. It is recognized that the amplitude of the fluctuations can be decreased by forcing a greater number of modes (Wang and Maxey 1993). This was not attempted because in such a case, more large scale modes are constrained and would not be free to evolve dynamically.

The characteristic parameters for the three flow configurations are listed in Table 7.1. All quantities, except the time step, are time averages over a minimum period of $20\tau_0$. The entries in the table, from the top to the bottom, are the time step, the root mean square velocity(u_0), the eddy dissipation rate(ϵ), the integral scale(l_0), the large eddy turnover time(τ_0), the Taylor microscale(λ) and the Taylor based Reynolds number(R_λ). The Kolmogorov length scale(η) and its associated time scale(τ_η) and velocity scale(v_η) are calculated from ϵ. These quantities are defined in Section 2.1. As can be seen in the table or in Fig. 7.1, the eddy dissipation rate is almost two orders of magnitude higher in *flowC* than in *flowA*. The Reynolds number also increases from *flowA* to *flowC*.

To see whether our grid resolution is adequate, we include two parameters, $k_{max}\eta$ and S, in Table 7.1. The product $k_{max}\eta$, where $k_{max} = \frac{2\pi}{2\Delta x}$ is the maximum wave number and Δx is the grid size, should be greater than one for the smallest scales of the flow to be resolved (Eswaran and Pope 1988). The parameter S represents the velocity derivative skewness defined as:

$$S = -\frac{< (\partial u/\partial x)^3 >}{< (\partial u/\partial x)^2 >^{3/2}}.$$

The values of S obtained from laboratory measurements in grid turbulence are of the

	flowA	*flowB*	*flowC*
$\Delta t(s)$	$5. \times 10^{-3}$	$2. \times 10^{-3}$	$8. \times 10^{-4}$
$u_0(cms^{-1})$	3.1	6.7	15.2
$\epsilon(cm^2s^{-3})$	1.9	14.	161.
$l_0(cm)$	3.1	2.9	2.5
$\tau_0(s)$	1.8	.72	.29
$\lambda(cm)$	.6	.5	.4
R_λ	12.	21.	34.
$\eta(cm)$	.2	.13	.07
$\tau_\eta(s)$	.29	.11	.03
$v_\eta(cms^{-1})$	.74	1.2	2.3
$k_{max}\eta$	5.4	3.2	1.8
S	.33	.40	.45

Table 7.1: Descriptive parameters of the three simulated flows

order of .4 (Lesieur 1990, page 145). In direct numerical simulations, Kerr (1985) stated that S should increase or remain constant with increasing R_λ. Failure to do so indicates that small scale truncation and aliasing errors are significant. The values listed in Table 7.1 indicated that the resolution used is adequate.

Another useful description of turbulence is the three-dimensional energy spectrum $E(k)$ at a given time, defined as:

$$E(k) = \frac{1}{2} \sum_{k-\frac{1}{2}<|\mathbf{k}|<k+\frac{1}{2}} |\hat{\mathbf{U}}|^2 = \frac{1}{2} \sum_{k-\frac{1}{2}<|\mathbf{k}|<k+\frac{1}{2}} \frac{|\hat{\omega}|^2}{|k|^2}.$$

The sum is over all modes whose wave numbers fall into a spherical shell of width $\Delta k = 1$. The top panel in Fig. 7.3 shows $E(k)$ for the three flow configurations at $t \approx 20\tau_0$. The bottom panel depicts the product of the energy spectrum and $k^{\frac{5}{3}}$. An inertial range occurs if this product exhibits a zero slope over several wave numbers. As can be seen, even for our most energetic case *flowC*, the Reynolds number is still not high enough and the flow is bordering between the inertial subrange and the dissipation range. Considering that our purpose is to simulate the typical ambient

conditions in which individual cloud droplets grow and that, as mentioned earlier, the Kolmogorov length scale and the average inter-droplet distance are of the same order of magnitude, such flow conditions are reasonable.

The flows simulated exhibit complex and intermittent behavior. Some indication of this is found in Fig. 7.4 which shows the time averaged (over $20\tau_0$) histogram (frequency distribution) of gridpoint values of one component of the vorticity for the three flow configurations. Each curve has been normalized by its time averaged standard deviation, whose values for the three configurations are $2.(flowA), 6.(flowB)$ and $16s^{-1}$ $(flowC)$. As expected for isotropic flows, these distributions are approximately symmetric. However, relative to the Gaussian distribution, there are significant differences in the tails, indicating the occurrence of regions of very high vorticity particularly as the Reynolds number increases. This behavior can be quantified by the kurtosis of the distributions whose time average ranges from .5 to 3. from *flowA* to *flowC*. The increasing deviation from a Gaussian distribution (reference curve denoted with N) is a signature of the presence of coherent vortices in isotropic turbulence (She et al. 1990). Furthermore, the intermittent nature of the vortices can also be inferred from Fig. 7.5 which depicts the histogram of the gridpoint values of one component of vorticity in *flowC* at nine different times sampled at an interval of $2\tau_0$. Evidently, the tails of the distributions, which denote regions of high vorticity, oscillate in time.

Fig. 7.6 shows cross sections of the velocity field (top panels) and the corresponding sections of the normal component of vorticity (bottom panels) for *flowA*(left panels) and *flowC*(right panels). The qualitative and quantitative difference between the two flows appears clearly. While *flowA* is relatively smooth, *flowC* is much more complex with compact regions of large positive or negative vorticities.

We are satisfied that after integrating the turbulent model for about $20\tau_0$, the turbulent flow fields can be described as stationary, homogeneous, and isotropic. These flow configurations, at their final simulation time, will be used as initial conditions

for subsequent experiments.

7.2 Effect of inertia term

We are in a position to examine the effects of inertia and sedimentation on the spatial distribution of non-condensing droplets in a turbulent flow. To do so, the equation of motion (4.6) or (4.8), with or without the sedimentation term, is time advanced for all droplets in conjunction with the flow equations. Table 7.2 lists the six main experiments performed. The notation *iniX* indicates that the initial flow field is drawn from flow configuration *X*. The symbols *sed* and *nosed* denote respectively whether sedimentation is included or excluded. Thus experiment *iniAnosed* consists of 50000 $20\mu m$ droplets moving in *flowA*. Experiment *iniBnosed* can be regarded as four separate experiments each with a different size distribution of droplets moving in *flowB*. Three of the size distributions are monodispersed, 10, 15 and $20\mu m$ droplets, while the fourth is a uniform size distribution from 10 to $20\mu m$. Experiment *iniCnosed* is similar to *iniBnosed* except that the initial flow configuration is from *flowC*. Similar experiments with sedimentation included are *iniAsed*, *iniBsed* and *iniCsed*. Starting from the statistically stationary, homogeneous and isotropic flow configurations discussed in Section 7.1, the experiments are integrated each for a duration of a minimum of $5\tau_0$.

The inertial effect is manifested by the differences between the fluid velocity and the droplet velocity arising from the droplet's inertia. Figs. 7.7 to 7.10 show four examples of the two-dimensional (2D) projections of the trajectory of $20\mu m$ non-sedimenting droplets onto the horizontal plane in *flowC* for a duration of .8*s*. The numbers 1 to 10 indicate the successive positions of the droplets every .08*s*. Two lines originate from each position. The line that terminates with a circular symbol represents the 2D projection of the fluid velocity at that point. The other line denotes the

droplet velocity. The speed is given by the length of the line with $1cm$ corresponding to a speed of $\approx 10cms^{-1}$. It can be noted that at some points, the two lines coincide (e.g., at 10 in Fig. 7.10 or at 9 and 10 in Fig. 7.7). At other points, particularly those associated with strong curvature, the difference between the direction of the two lines can be significant (e.g., at 2 in Fig. 7.7 or 8 in Fig. 7.8). At certain locations, the two lines are almost parallel but their lengths differ, indicating that either the speed of the droplet may be less than that of the fluid (e.g., 6 in Fig. 7.7) or the opposite is true (e.g., 7 in Fig. 7.7).

Fig. 7.11 offers direct visual evidence that the spatial distribution of the droplets is affected by the turbulent flow field through the inertial effect. We examine results of experiment *iniCnosed*. The top left panel shows a cross section of the field of the magnitude of vorticity . The other three panels show the position of each droplet in the same cross section, either for 20 (top right), 15 (bottom left) or $10\mu m$ (bottom right) droplets. The correspondence between regions of a high vorticity and low droplet concentration is evident for the $20\mu m$ droplets. In particular, we note in the upper right portion of the top right panel a crescent shaped region void of droplets (more than 1 *cm* across). This region is co-located with the crescent shaped region of high magnitude of vorticity seen in the top left panel. In the two bottom panels we can see the decreasing correspondence between high vorticity and low droplet concentration as a function of decreasing droplet size.

To assess the effect of inertia on all the droplets, we need to quantify the deviations of the positions of the droplets from those given by a random distribution described by Poisson statistics. To do so, the clustering index as defined in Appendix A is calculated as follows. The domain is subdivided into sampling volumes of a given size. The number of droplets in each of these cubic volumes is counted. A distribution of the number of cubes containing a specified number of droplets is then constructed. The index is given numerically by the ratio of the variance of this distribution to

name	flow	$R(\mu m)$	sedimentation	duration
iniAnosed	*flowA*	20	no	$5\tau_0$
iniAsed	*flowA*	20	yes	$5\tau_0$
iniBnosed	*flowB*	10-15-20-uniform	no	$14\tau_0$
iniBsed	*flowB*	10-15-20-uniform	yes	$14\tau_0$
iniCnosed	*flowC*	10-15-20-uniform	no	$17\tau_0$
iniCsed	*flowC*	10-15-20-uniform	yes	$17\tau_0$

Table 7.2: Description of basic experiments done to explore the role of inertia

the expected variance if the spatial distribution of the droplets was Poisson (variance is simply equal to the mean) minus one. Obviously, if the droplets are distributed randomly, the clustering index is zero. We evaluate the index for several sizes of the sampling volume.

Fig. 7.12 shows the clustering index as a function of the length scale of the sampling cubic volume for experiment *iniAnosed*. The index was calculated every $.5\tau_0$, from $t = .5\tau_0$ (curve A) to $t = 5\tau_0$(curve I). Twelve different sizes of the sampling cubes were used. The largest cube has sides equal to one fourth the width of the integration domain. In Fig. 7.12, the sizes of the sampling cubes are given by the horizontal coordinate of the letters attached to each curve. The number of sampling cubes in the integration domain varies between 46^3 for the smallest cube to 4^3 for the largest one. Two dashed lines which correspond to $\pm\sqrt{2/N}$, where N is the number of sampling volumes, are also plotted. As explained in Appendix A, they represent the expected standard deviation of the statistical error on the clustering index related to the finite number of sampling cubes. Preferential concentration of droplets can be inferred when the clustering index lies significantly outside this region of error. For clarity of presentation, the cluster index corresponding to the twelve sizes of the sampling cubes are plotted on two panels with different scales.

The first two curves(A and B) lie mostly within the dashed lines and therefore

no preferential concentration can be diagnosed at these times. However, some small degree of preferential concentration can be seen after $\approx 2\tau_0$ when the clustering index is greater than the error for all sampling length scales. It can also be observed that the clustering index generally increases with an increase in the size of the sampling cube. The highest index, 1.1, is found in curve F at the sampling length scale of $25mm$. This value implies that the standard deviation of the number distribution in this experiment (41) is ≈ 1.45 times greater than that of the Poisson distribution(28) with the same mean (781.25).

We discussed in Section 2.4.2 that particles, due to their inertia, tend to diverge from regions of high vorticity and converge preferentially in regions of low vorticity and high strain rate. Visual evidence of the link between preferential concentration and vorticity was shown in Fig. 7.11. This link can be described quantitatively by calculating the correlation between the magnitude of the vorticity and the number of droplets $r(|\omega|, n)$ as a function of sampling length scale. Fig. 7.13 shows this correlation for experiment *iniAnosed* calculated using five sampling length scales. The times for the nine curves, designated by the letters a to i, are the same as those in Fig. 7.12.

We can estimate the statistical significance of the calculated correlation as follows. Let the magnitude of the calculated correlation be $|r|$, the probability of obtaining a correlation with magnitude $> |r|$ from two uncorrelated distributions (i.e. under the null hypothesis) is given by (Press et al. 1986):

$$erfc\left(\frac{|r|\sqrt{N}}{\sqrt{2}}\right),$$

where $erfc(x)$ is the complementary error function, and N is the number of sampling volumes. Two dashed lines are plotted in Fig. 7.13. The top line and the bottom line correspond to values of r such that $erfc\left(\frac{|r|\sqrt{N}}{\sqrt{2}}\right)$ equal 10^{-3} and 10^{-6} respectively. If the correlations have values lying between these two lines, it means that

the probability that the correlations are the result of correlating two uncorrelated signals is smaller than .1% but larger than .0001%. As can be seen in the figure, the correlations have small magnitudes but they are generally statistically significant in the sense that the probability that the same correlation occurs under the null hypothesis is very small. Note that the correlations are always negative confirming the link between large magnitudes of vorticity and small concentrations of droplets.

To illustrate the effect of sedimentation, we plotted the clustering index for experiment *iniAsed* in Fig. 7.14. Contrary to Fig. 7.12, the clustering index is generally quite small and not significantly greater than the error for all sampling length scales at all times. Preferential concentration is therefore insignificant in this flow configuration when sedimentation is included. We further examine the correlation , $r(|\omega|, n)$, for *iniAsed*. The correlation (not shown) is also found to be insignificant for all sampling length scales and for all times.

Before systematically studying the results from the other experiments in Table 7.2, we first analyze *iniCsed* which clearly indicates preferential concentration for sedimenting $20\mu m$ droplets. Fig. 7.15 shows the clustering index (top two panels) and $r(|\omega|, n)$ (bottom panel) as a function of the sampling length scale every $.5\tau_0$ from $t = 0$ (curve A) to $t = 5\tau_0$ (curve K). The values of the clustering index and the magnitude of the correlation are much higher than in *flowA*. The magnitude of the clustering index increases for all sampling length scales up to $t = 2\tau_0$ and then it fluctuates. The correlation reaches statistically significant values within a duration of $.5\tau_0$. The maximum magnitude of the correlation (.4) occurs at $1.5\tau_0$ for a sampling length scale of $12.5mm$. In general, the magnitude of the correlation increases with sampling length scale up to $12.5mm$. It then decreases to statistically insignificant values when the sampling length scale reaches $20mm$ (see curves I and J).

The existence of preferential concentration when the clustering index is large can be visualized more directly from the deviation of the frequency distribution of the

number of droplets from Poisson statistics. Fig. 7.16 depicts six distributions of the fraction of sampling volumes containing a certain number of droplets (curves marked by stars) for the six sizes of the sampling volumes indicated in the top panel of Fig. 7.15. The figure also contains the corresponding curves (unmarked) for Poisson statistics, the mean number of droplets per sampling volume, and the clustering index C for each case. The horizontal lines indicate the minimum meaningful probability which is given by the reciprocal of the number of sampling volumes. As an example, we describe the distribution at the lower right hand corner. The domain was divided into 15^3 sampling volumes containing an average of 14.81 droplets. The computed distribution is obviously wider than the Poisson distribution, with much more frequent extreme values. For instance, 18 sampling volumes (or .005 in fraction) contain no droplets. One sampling volume(or $1/15^3$ in fraction) contains 45 droplets which amounts to three times the mean. The clustering index C is 1.895, which translates into the variance of the computed probability distribution being 2.895 times greater than the variance of the Poisson distribution. Equivalently, the calculated standard deviation is $\sqrt{2.895}$, which is 1.7 times larger than that of the Poisson distribution.

We now return to examine the other experiments in Table 7.2. For economy, we will mostly present results at the final time of the experiments. A summary of the Stokes number for the various combination of flow configurations and drop sizes is given in Table 7.3.

Fig. 7.17 shows the clustering index for experiment *iniBnosed*. Curves A to C are for the 10, 15 and $20\mu m$ droplets respectively, while curve D is for the uniform size distribution. It is clear that the spatial distribution of droplets of different sizes can behave quite differently in the same flow. The clustering index increases sharply as a function of increasing droplet size. For the $10\mu m$ droplets, the clustering index lie within or close to one standard deviation of the error (dashed lines). This is also true at other times (not shown), when the cluster index exceeds twice the value of

the statistical error on only a few occasions. The Stokes number for this particular droplet size/flow combination is 0.012, too small for the inertia of the droplets to cause any significant deviation of their spatial distribution from randomness. As for the other droplet sizes, it can be seen that curve D and curve B are close to each other, indicating that when the mean radius of the droplets is the same, the spatial distribution of the droplets for the uniform size distribution is similar to that of the monodispersed distribution. This result is attributable to the fact that when droplets of different sizes are present in a flow, the bigger droplets tend to cluster in areas of low vorticity and their clustering index is high. The smaller the droplets, the more they would tend to be distributed randomly and their associated clustering index is small. The above results are valid for all times in this experiment.

When sedimentation is included in *iniBsed*, the clustering index in general decreases for both the $15\mu m$ and the $20\mu m$ monodispersed distributions (compare Fig. 7.18 and Fig. 7.17). The reduction is especially pronounced for the $20\mu m$ droplet (curve C) except at the largest sampling length scale of $25mm$ at the final time of integration. For the $10\mu m$ droplets, the clustering index always lies within the bounds of the statistical error, indicating the small effect of sedimentation for droplets of this size.

Consistent results are also found in the correlation $r(|\omega|, n)$ (Fig. 7.19). When sedimentation is suppressed (*iniBnosed*, bottom panel), the magnitude of the correlation increases with droplet size at all times. However, when droplets sediment (*iniBsed*, top panel), the magnitude of the correlations are smaller and the differences between the curves become less significant. Furthermore, there is no longer a systematic increase of the magnitude of the correlation with the size of the droplets. For example, the magnitude of the correlation for the $20\mu m$ droplets (curve C) is close to or smaller than that of the other sizes at several sampling length scales.

To examine how the correlation changes with time, we plotted the correlation

curves at ten output times (curves A to J) for the three monodispersed size distributions in Fig. 7.20. The curves labeled J are the same as those in Fig. 7.19. The top, middle and bottom panels depict the results for the $10\mu m$, $15\mu m$, and $20\mu m$ droplets respectively. A close inspection of the figure shows that most correlations for the $10\mu m$ droplets are statistically insignificant. With a few exceptions, the magnitude of the correlations for the $15\mu m$ droplets are greater than those for the $10\mu m$ droplets. Similar results are indicated for the $20\mu m$ droplets except at the time corresponding to curve J. However, contrary to the experiment without sedimentation, there is no systematic increase in the magnitude of the correlation when the size changes from 15 to $20\mu m$. Thus sedimentation complicates the relationship between vorticity and the number concentration of droplets.

The clustering index at the end of experiments *iniCnosed* and *iniCsed* are shown in Figs. 7.21 and 7.22. The magnitude of the index is significantly greater for all size distributions than in the case with *flowB*. In particular, clustering also occurs for the $10\mu m$ droplets. Again the effect of sedimentation is more pronounced for the bigger droplets and it is minimal for the $10\mu m$ droplets. In the case of droplets with a radius of $15\mu m$, there is a small but systematic decrease in the clustering index when sedimentation is included, except for the largest sampling length scale. For the $20\mu m$ droplets, there is a clear systematic decrease of the clustering index because of sedimentation except at the two largest sampling length scales. Contrary to the experiments with sedimentation in *flowB*, there is a systematic increase of the index as a function of droplet size for all sampling length scales.

Fig. 7.23 shows graphs of $r(|\omega|, n)$ for *iniCsed*(top panel) and *iniCnosed*(bottom panel). Without sedimentation (bottom panel) there is a clear increase in the magnitude of the correlation with droplet size. With sedimentation (top panel), there is still a gap between curve A and the other curves. However, the correlations for the 15 and $20\mu m$ droplets become close to each other at the end of the experiment and

$\epsilon(cm^2s^{-3})$	$R = 10\mu m$	$R = 15\mu m$	$R = 20\mu m$
1.9(*flowA*)	.004	.01	.017
14 (*flowB*)	.012	.026	.047
161(*flowC*)	.040	.090	.16

Table 7.3: Stokes number for experiments with inertia.

at other times. A comparison of the top and bottom panels indicates that, for the $20\mu m$ droplets, sedimentation in general reduces quite significantly the magnitude of the correlation, with some exceptions at the largest sampling length scale. For the $15\mu m$ droplets, $r(|\omega|, n)$ generally decreases because of sedimentation for the two smallest sampling length scales. For the larger sampling length scales, the magnitude of the correlation increases with sedimentation at the end of the experiment but shows a decrease at other times (not shown). No systematic effect of sedimentation on the correlation was found for the $10\mu m$ droplets. Finally, for the uniform size distribution, the behavior of the clustering index and the correlation for sedimenting and non-sedimenting droplets are similar to those of the $15\mu m$ monodispersed size distribution.

To summarize our results, we present in Table 7.3 the Stokes number corresponding to the various combinations of flow configuration and size of droplets. Without sedimentation, the clustering index and the magnitude of the correlation between vorticity and number density increase with the Stokes number. The lowest Stokes number at which some preferential concentration is present is .017 in experiment *iniAnosed*. Using this value as an approximate threshold, it is simple to calculate that the smallest size of the droplets for which preferential concentration can be expected is 20, 12 and $7\mu m$ in *flowA*, *flowB* and *flowC* respectively.

The picture becomes more complicated with sedimentation. Table 7.4 presents a qualitative summary of its effect on the clustering index (C) and the magnitude of the

correlation $|r(|\omega|, n)|$ (R). Relative to the no sedimentation runs, the magnitudes for C and R are in general smaller for the range of flow configurations and droplet sizes considered. However, they are still statistically significant unless preferential concentration is absent or very small in the no sedimentation runs (e.g., the $10\mu m$ droplets in *flowB* and the $20\mu m$ droplets in *flowA*). In addition, the relation between Stokes number and preferential concentration is less straightforward. It was found that in most cases, when ϵ is held fixed, an increase in the size of the droplets (corresponding to an increase in Stokes number) leads to an increase in the clustering index. But there are exceptional cases where the magnitude of C remains the same or even decreases when the droplet size (Stokes number) increases. Another interesting result is that the reduction in the magnitude of C and R relative to the no sedimentation runs decreases when the level of turbulence increases, as is evident when the reduction of C in *flowB* (Figs. 7.17 and 7.18) is compared to that in *flowC* (Figs. 7.21 and 7.22).

The complicated behavior of C and R in the sedimentation case can be explained by recognizing that sedimenting droplets are characterized by a mean velocity relative to the flow. The time of interaction between a droplet and an eddy is therefore reduced, so is the possibility of clustering . Sedimentation therefore introduces a new time scale - the time it takes a droplet to cross an eddy (Eaton and Fessler 1994) under its own terminal velocity. Table 3.1 compares this time scale ($\tau_V = \eta/V_T$), for eddies whose size is given by the Kolmogorov length scale, to the eddies' turnover time (τ_η) as a function of droplet size and eddy dissipation rate. The relative importance of sedimentation in reducing the time of interaction between a falling droplet and an eddy with size equals the Kolmogorov length scale can be estimated by calculating the ratio τ_V/τ_η. Clearly, if this ratio is very small then the droplets and the eddies will have no time to interact. If this ratio is large, sedimentation does not significantly reduce the time for the droplets and the eddies to interact and so its effect can be neglected. Thus, a large ratio indicates a small influence of sedimentation.

Flow	Description	Comments
A	$20\mu m$	Eliminates all significant C and R
B	$10\mu m$	Eliminates few significant C
B	$15\mu m$	Decreases C and R
B	$20\mu m$	Significant decrease in C and R
B	comparing $10\mu m$ to $15\mu m$	In general, increase in R and C
B	comparing $15\mu m$ to $20\mu m$	Small but general increase in C. No systematic trend of R
C	$10\mu m$	No systematic effect on C or R
C	$15\mu m$	Decreases C and R, except at largest sampling length scales
C	$20\mu m$	Significant decrease in C and R, except at largest sampling length scales
C	comparing $10\mu m$ to $15\mu m$	In general, increase in R and C. exceptions at large sampling length scale
C	comparing $15\mu m$ to $20\mu m$	No systematic trend of C or R

Table 7.4: Qualitative summary of the effect of sedimentation on the clustering index (C) and $|r(|\omega|, n)|$ (R) for the various experiments.

An inspection of Table 3.1 reveals that for a fixed ϵ, the ratio τ_V/τ_η decreases as a function of increasing droplet size. This explains why the spatial distribution of the larger droplets is much more affected when sedimentation is included. Furthermore, for a fixed droplet size, the ratio τ_V/τ_η increases as a function of increasing eddy dissipation rate, consistent with the result that the reduction in the magnitude of C and R relative to the no sedimentation runs decreases when the level of turbulence increases.

7.3 Condensational growth and evolution of spectra

We now present the results of the complete experiments including the condensational growth of the droplets. Our objective is to investigate how the presence of a turbulent flow modifies the results in Chapter 6. For each flow configuration, we will examine how the non-Poisson spatial distribution of droplets and the variability in vertical velocity affects the size spectrum of the sedimenting droplets.

We shall investigate systematically the effect of including the condensational growth of droplets. Recall that in Chapter 6, we examined droplets growing by condensation in an environment without turbulence where the droplets are distributed randomly in space (e.g. experiment N07). As was shown in the last section, the inertial effect of droplets can result in preferential concentration (spatial distribution deviates from randomness) of droplets in turbulence. Thus as a first step, we would perform a no turbulence reference experiment (R1), similar in most respects to N07, except that the number of grid cells is 80^3 and initial spatial distribution of the monodispersed $15\mu m$ droplets is given by that at the end of experiment *iCnosed*. R1 will be run for a duration of 200s. We will compare the results of R1 with a modified N07 run with 80^3 points (hereafter called R2) to see how preferential concentration affects the growth of droplets.

Turbulence would then be introduced. Table 7.5 gives a list of the experiments performed, including the reference experiments R1 and R2. The first letter in the symbols for the experiments denotes the flow configuration. For example, Aa, Bd, and Ch are the three full experiments for *flowA*, *flowB* and *flowC*. They include all the relevant effects, inertia (except for Aa where inertial effect is negligible), sedimentation, condensational growth, and perturbation cooling from the fluctuation turbulent vertical velocity. A number of sensitivity experiments are also performed (namely

$Ab, Ac, Be, Bf, Bg, Ci, Cj$, and Ck), where one or more effects are suppressed.

To save computer time, the experiments with turbulence in Table 7.5 last for a duration of ten seconds. As will be mentioned below, a few selected $50s$ and $200s$ experiments were made and the results are similar to the corresponding $10s$ runs. The initial size distribution in all runs is monodispersed, and all droplets have a radius of $15\mu m$. Inertial effect is neglected in the runs involving *flowA* because as was shown earlier, the spatial distribution of droplets of the size under consideration deviates little from randomness. For the experiments where inertia is included, the initial flow field and the spatial distribution of the droplets are given by those at the end of experiments *iniBsed*, *iniBnosed*, *iniCsed* or *iniCnosed*, depending on the appropriate flow configuration and whether sedimentation is included or excluded. Because we neglect all effects of the droplets on the flow (see Section 2.4 for justification), the time evolution of the flow is the same for all experiments involving the same flow configuration, which greatly simplified the interpretation of the results. Also because the initial size of all the droplets are the same in all experiments, the *macroscopic* results for all runs are identical. Therefore any difference between two experiments can be attributable to *microscopic* effects alone.

Table 7.5 also records some statistical results for the different runs at a time of $10s$. As a reminder, we mention that the terminal velocity for a $15\mu m$ droplet is $2.7cms^{-1}$. The root mean square velocities for *flowA*, *flowB*, *flowC* are 3.1, 6.7, and $15.2cms^{-1}$ respectively.

Fig. 7.24 shows the temporal evolution of the standard deviation of the size distribution, $\sigma(R)$ (top panel) and the variance of the perturbation degree of growth, $V(\beta'^2)$ (bottom panel) for R1 (curve 1) and R2 (curve 2). Recall that $\sigma(R_M) \equiv 0$ when the initial size distribution is monodispersed. Clearly, for a frozen configuration of droplets, preferential concentration has an important broadening effect on the size distribution. The effect on individual droplets is illustrated in Fig. 7.25 which depicts

the distribution of ${}^tR - {}^tR_M$ at $200s$. The standard deviation, the maxima and minima of the distribution are significantly larger in R1. Furthermore, the distribution is positively skewed rather then negatively skewed as in all experiments described in Chapter 6 where the spatial distribution of droplets is Poisson.

Fig. 7.26 compares the temporal evolution of the supersaturation perturbation for several droplets in Aa, Bd and in Ch. Because of turbulence and sedimentation, the droplet's growth rate varies rapidly. Recall that it is the time integrals of such signals that determine whether differences appear in the droplet sizes between the *microscopic* and *macroscopic* approaches. Furthermore, it is the variance, over all droplets, of the time integral of the supersaturation perturbation that determines if broadening of the *microscopic* size distribution relative to the *macroscopic* size distribution can occur.

Figs. 7.27 and 7.28 show the temporal evolution of the standard deviation of the size distribution, $\sigma(R)$, and the variance of the perturbation degree of growth, $V(\beta'^2)$ for the rest of the experiments in Table 7.5. The full experiments Aa, Bd, and Ch are compared at the top left panels of each figure. The curves are labeled by a capital letter which corresponds to the last letter of the experiments listed in Table 7.5. For example, the curve for Bd is labeled D. Comparing the curves A, D and H in Fig. 7.28, we see clearly that $V(\beta'^2)$ decreases as the level of turbulence increases. Since the initial distributions are monodispersed, a decreasing variance implies (see(5.14) and(5.16)) that spectral broadening also decreases when the level of turbulence increases (top left panel of Figs. 7.27).

The other panels depicts the results of sensitivity experiments in the three flow configurations. Note that the scales vary from panel to panel. Obviously neglecting sedimentation has a significant positive impact on spectral broadening (compare curves B to A, E to D and I to H), so is the inclusion of the cooling term from

turbulent vertical velocity (compare curves A to C, D to G and H to K). Furthermore, the inertia induced non-Poisson spatial distributions of droplets also contribute positively to a broadening of the spectrum (compare curves D to F and H to J).

For a more quantitative comparison, we refer to the statistical information at 10s in Table 7.5. Column 6 contains the dispersion of the perturbation degree of growth distribution, a time integrated quantity. Columns 7, 8 and 9 list the instantaneous dispersion of the supersaturation perturbation distribution, the standard deviation of the field of temperature perturbation and the standard deviation of the field of water vapor mixing ratio perturbation respectively. Note that the supersaturation perturbation distribution is calculated from the perturbation at the grid points which contain droplets.

It is instructive to compare first the results for experiments Aa, Bf and Cj, where droplet inertia or preferential concentration is neglected. The dispersion of the perturbation degree of growth ($\sigma(\beta'^2)/\beta_M^2$) decreases (from .411% to .252% to .154%) as the intensity of turbulence increases. The same is true for the dispersion in supersaturation perturbation ($\sigma(S')/S_M$) and the standard deviation in water vapor perturbation ($\sigma(q_v')$). As will be shown later, this decrease is attributable to the decrease in decorrelation time as the turbulence becomes more active. It should be pointed out that the standard deviation for temperature perturbation ($\sigma(T')$) increases slightly from Aa to Bf but then decreases in Cj. This unusual behavior is related to the presence of the cooling term in the temperature perturbation equation (4.20). The contribution of the cooling term to $\sigma(T')$ is directly proportional to the root mean square vertical velocity which increases with the level of turbulence. Consequently there are two competing processes in changing $\sigma(T')$, a reduction due to a decrease in decorrelation time and an enhancement due to increasing local cooling as turbulence becomes more active. The relative importance of these two processes determines the behavior of $\sigma(T')$.

Experiments Bd and Ch differ from Bf and Cj by including the inertia of droplets which leads to preferential concentration. Since preferential concentration increases with the activity of turbulence, inertia is expected to enhance progressively the dispersion and standard deviation of various quantities as the level of turbulence increases. Comparing the results of Aa, Bd and Ch against those from Aa, Bf and Cj, we see that when inertial effect is included, $\sigma(S')/S_M$, $\sigma(T')$ and $\sigma(q_v')$ actually increases with the intensity of turbulence. While $\sigma(\beta'^2)/\beta_M^2$ still decreases when the level of turbulence increases, the magnitude of decrease is smaller than that in the experiments without the inertial effect.

Sedimentation can affect the results in two ways. Comparing experiments Aa and Ab, we see that when sedimentation is absent, $\sigma(T')$ and $\sigma(q_v')$ are significantly larger. Sedimentation also impacts the results through its effect on preferential concentration. A close examination of Table 7.5 shows that neglecting sedimentation has a larger impact on $\sigma(\beta'^2)/\beta_M^2$ and $\sigma(S')/S_M$ than neglecting the cooling term or the inertia effects in *flowA* and *flowB*. However, in *flowC* the neglect of inertia has the largest effect. This behavior is consistent with the result obtained in a previous section that sedimentation of droplets of a given size have a decreasing impact on preferential concentration as the level of turbulence increases.

The effect of turbulence can now be clarified by comparing the results obtained so far with those from the reference experiments $R1$ and $R2$. Two important observations can be made. First, the presence of turbulence significantly decreases the dispersion of the instantaneous distribution of supersaturation perturbation $\sigma(S')/S_M$ (through decreases in the standard deviation of the temperature and water vapor mixing ratio perturbations which are of the same magnitude as the decrease in $\sigma(S')/S_M$). These decreases can be explained in the same manner as the similar decreases found when studying the effect of sedimentation on the no turbulence experiments in Chapter 6. They are due to the fact that regions void of droplets and regions of high

droplet concentration, where significant perturbations in the scalar fields can develop, will exist only for a short time. Second, turbulence reduces even more significantly the dispersion in the time integral of the supersaturation perturbations along the trajectory of the droplets. As a result, $\sigma(\mathcal{J}'^2)/\mathcal{J}_M^2$ is significantly smaller than $\sigma(S')/S_M$ in a turbulent flow. On the other hand, these two dispersions are almost of the same magnitude when turbulence is absent. Furthermore, as noted previously, the difference between these two dispersions increases with the intensity of turbulence.

Fig. 7.30 compares the temporal evolution of $\sigma(R)$ for $R1$ and $R2$ and for experiment Aa extended to 200s. Evidently, $\sigma(R)$ is much smaller in Aa at all times. It is clear that even weak turbulence significantly decreases the difference between the results of the *microscopic* and *macroscopic* approaches that were found in the experiments with no turbulence and no sedimentation.

Much of the effect of turbulence can be traced to the behavior of the decorrelation time. Fig. 7.29 shows the autocorrelation coefficient of S', averaged over 2000 randomly chosen droplets, as a function of the lag time for all experiments in Table 7.5 except Ac, Bg and Ck. The curves for Ac, Bg and Ck are very similar to those for Aa, Bd and Ch and are excluded for clarity of presentation. Comparing curves A, D and H shows a clear decrease in decorrelation time as a function of the increasing level of turbulence. Sedimentation (compare curves B to A, E to D and I to H) has a negative effect on the decorrelation time. The importance of sedimentation decreases with an increase in turbulence intensity. Inertia seems to have only a small effect on the decorrelation time (compare curves F to D and J to H). Furthermore, it is found that the decorrelation time in *flow*A is more than twice that in *flow*C whether we define the decorrelation time as the time when the autocorrelation decreases to a value of $1/e$ or the time at which it approaches zero. This implies that, over the duration of the experiments, the time integrals of the supersaturation perturbations are evaluated over more than twice as many decorrelation times in the experiments

with *flowC* as compared to those with *flowA*.

To ensure that our results do not depend critically on the duration of the experiments, we integrated the full experiment Ch to $50s$ and compared it to Aa at $50s$. The effects for different processes are found to be similar to those in the corresponding $10s$ experiments. Furthermore, we examined the temporal evolution of the dispersion of the degree of growth $(\sigma(\beta'^2)/\beta_M^2)$ and found that it is a slowly decreasing function of time in all experiments with turbulence. It reaches values of .33% (.17%) at $50s(200s)$ in Aa and .12% at $50s$ in Ch. In contrast, the dispersion is a slowly increasing function of time in the experiments without turbulence and sedimentation reaching values of 5 and 3% in $R1$ and $R2$ respectively after $200s$.

In this chapter, we have so far employed an initial spectrum which is monodispersed. The reason is that according to the finding in Chapter 6, this distribution would lead to a maximum effect in the broadening of the size spectra. For completeness, we have also conducted two (with and without sedimentation) $200s$ simulations in *flowA* using the same broad initial size distribution as in *N06* of Chapter 6. Recall that for a broad spectrum (see Chapter 6), droplets smaller (larger) than the average size tend to grow faster (slower) than their *macroscopic* counterparts in an environment without turbulence. Consequently, spectra which are initially very wide become narrower than the *macroscopic* spectra. To verify if this result still holds in the presence of turbulence, we analyzed these two new experiments and found that the right hand side of (5.14) is negative so that the *microscopic* spectra is narrower than the *macroscopic* spectra. However, the difference in standard deviations$(100. \times \frac{\sigma(R)-\sigma(R_M)}{\sigma(R_M)})$ is $<\approx -1\%$.

name	flow	inertia	sedimentation	cooling	$\frac{\sigma(\beta^{1/3})}{\beta_M^{1/3}}(\%)$	$\frac{\sigma(S')}{S_M}(\%)$	$\sigma(T')(\times 10^3)$	$\sigma(q_v')(\times 10^6)$
Aa	A	no	yes	yes	.411	.848	.50	.19
Ab	A	no	no	yes	.693	1.22	.74	.26
Ac	A	no	yes	no	.403	.836	.48	.18
Bd	B	yes	yes	yes	.311	.902	.59	.19
Be	B	yes	no	yes	.492	1.19	.76	.27
Bf	B	no	yes	yes	.252	.779	.52	.15
Bg	B	yes	yes	no	.271	.849	.51	.19
Ch	C	yes	yes	yes	.225	.943	.63	.21
Ci	C	yes	no	yes	.277	1.07	.72	.24
Cj	C	no	yes	yes	.154	.676	.46	.12
Ck	C	yes	yes	no	.206	.912	.55	.21
R1	no	no	no	no	4.36	5.34	3.5	1.3
R2	no	no	no	no	2.20	2.42	1.5	.54

Table 7.5: Description of comparative experiments with condensational growth of cloud droplets.

7.4 Two-way coupling

In Section 2.4 we discussed the possibility that the presence of the droplets may influence the turbulent flow through the drag force and the thermodynamic effect in the form of sources or sinks of latent heat and water vapor. To examine the importance of this feedback, we conducted three experiments similar to Aa, Bd and Ch but including the effects of the droplets on the flow through the buoyancy term in the flow equation (4.9). Fig. 7.31 compares the temporal evolution of the kinetic energy and the eddy dissipation rate for experiment Ch with and without the buoyancy term. The temporal evolution of these quantities is modified but their time means change only by a few percent. Fig. 7.32 shows the temporal evolution of the standard deviation of the size distribution for the experiments with (small letters) and without the buoyancy term (capital letters). It can be seen that the inclusion of the buoyancy term has only a small effect on the evolution of the standard deviation of the size distribution and therefore the neglect of this term in most of our experiments is

valid. Note that this simplification makes it much easier to analyze the microphysical results because we can repeat the experiments with various initial size distributions with exactly the same flow.

The fact that the temperature and water vapor mixing ratio perturbations at the scales considered here do not significantly influence the turbulent flow can be understood with a simple scale analysis of the inertial $(\mathbf{U} \cdot \nabla)\mathbf{U}$ and the buoyancy term $(g[T'/T_0 + .608q_v'])$ in the flow equation (4.9). The inertial acceleration term scales as U^2/L. Using typical values for the temperature and water vapor mixing ratio perturbations found in Table 7.5, and the root mean square velocity and the integral scale of *flowA* (Table 7.1) as typical velocity and length scales, we find that the order of magnitude for the buoyancy acceleration and for the inertial acceleration are respectively $\sim 2. \times 10^{-3}\ cms^{-2}$ and $\sim 1.\ cms^{-2}$. Hence, even for the lowest level of turbulence, the inertial acceleration is more than two order of magnitude larger than the buoyancy acceleration for the small scales under consideration.

7.5 Comparison with observations

Brenguier and Chaumat (1996) analyzed measurements made with the Fast Forward Scattering Spectrometer Probe (Brenguier et al. 1998) in adiabatic cloud cores. This data set provides the microphysical data with the highest size and spatial resolution available at this time. By comparing the narrowest spectra sampled at various altitudes against a reference level spectrum taken near the cloud base, they were able to infer the probability distribution of the time integral of the supersaturation necessary to explain the evolution of the observed spectra. Their procedure consists of inverting the following equation:

$$g(\phi^2, z) = \int_0^{\beta^2_{max}} \psi(\beta^2) f(\phi^2 - \beta^2, z_0) d\beta^2,$$

where ϕ is the droplet diameter, $f(\phi^2 - \beta^2, z_0)$ is the reference spectrum at level z_0, $g(\phi^2, z)$ is a spectrum measured at level z and $\psi(\beta^2)$ is the probability density function of the integral of supersaturation.

Fig. 7.33 summarizes Brenguier and Chaumat (1996) findings. It shows the calculated standard deviation of the distribution of the degree of growth as a function of the calculated average degree of growth for many selected spectra. In our notation, $\sigma(\beta'^2) = \sqrt{2}\sigma_{\beta^2}^*$ and $\beta_M^2 = \overline{\beta^2}$. They found that the broadening of the spectra, as measured by $\sigma(\beta'^2)$, is proportional to the average degree of growth, β_M^2. Furthermore, for a given β_M^2, the minimum broadening given by $\frac{\sigma(\beta'^2)}{\beta_M^2} \times 100$, is $\approx 21\%$. Referring to Tables 6.2 and 7.5 we see that the minimum broadening inferred by Brenguier and Chaumat (1996) from their measurements is much larger than the maximum broadening we found under the most favorable conditions of no flow and no sedimentation ($\frac{\sigma(\beta'^2)}{\beta_M^2}$ is only 4.36% in R1).

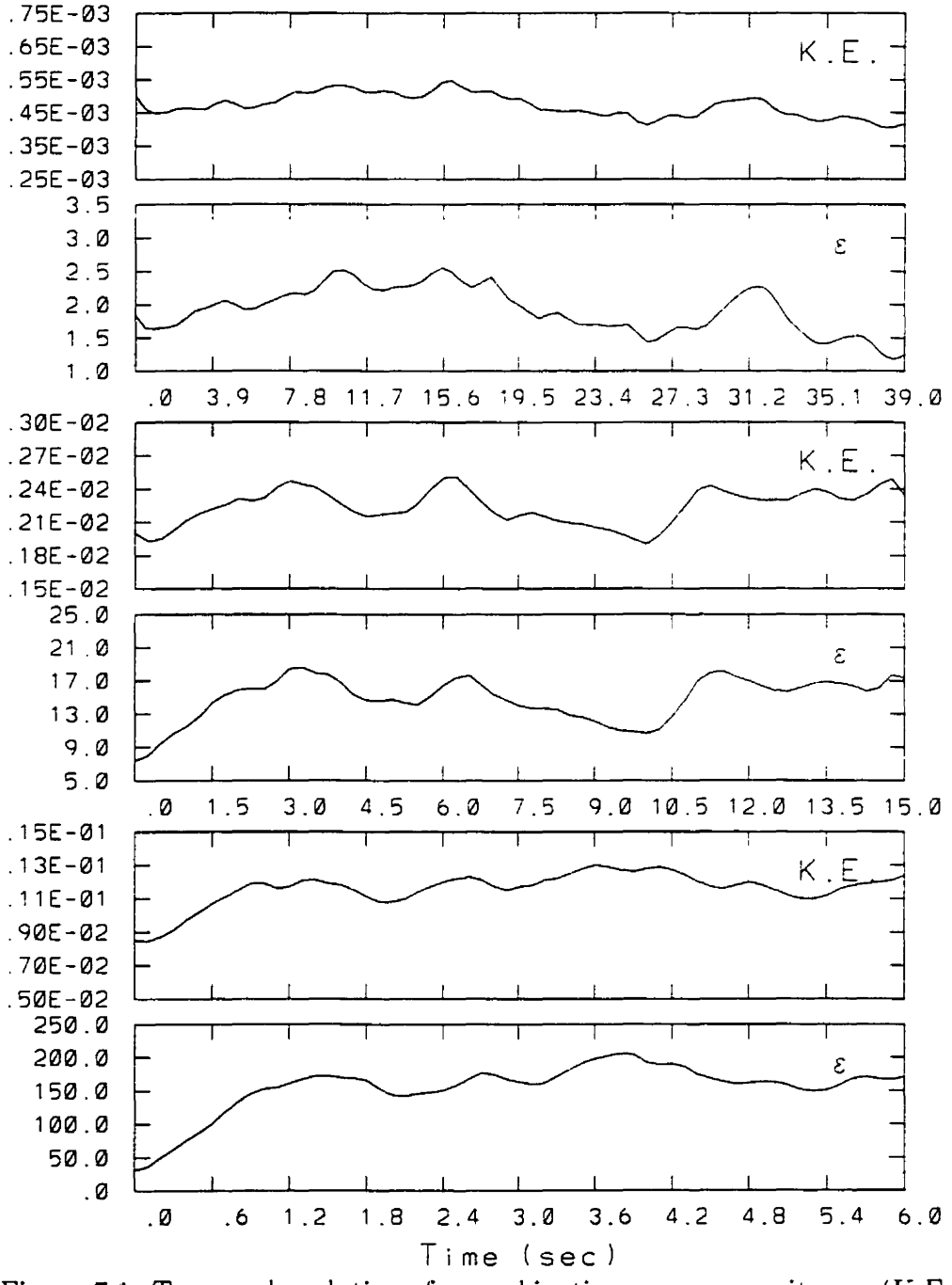

Figure 7.1: Temporal evolution of mean kinetic energy per unit mass(K.E. in units of $m^2s^{-2}kg^{-1}$) and mean eddy dissipation rate (ϵ in units of cm^2s^{-3}) for the three flows denoted with letters A(top two panels),B and C(bottom two panels).

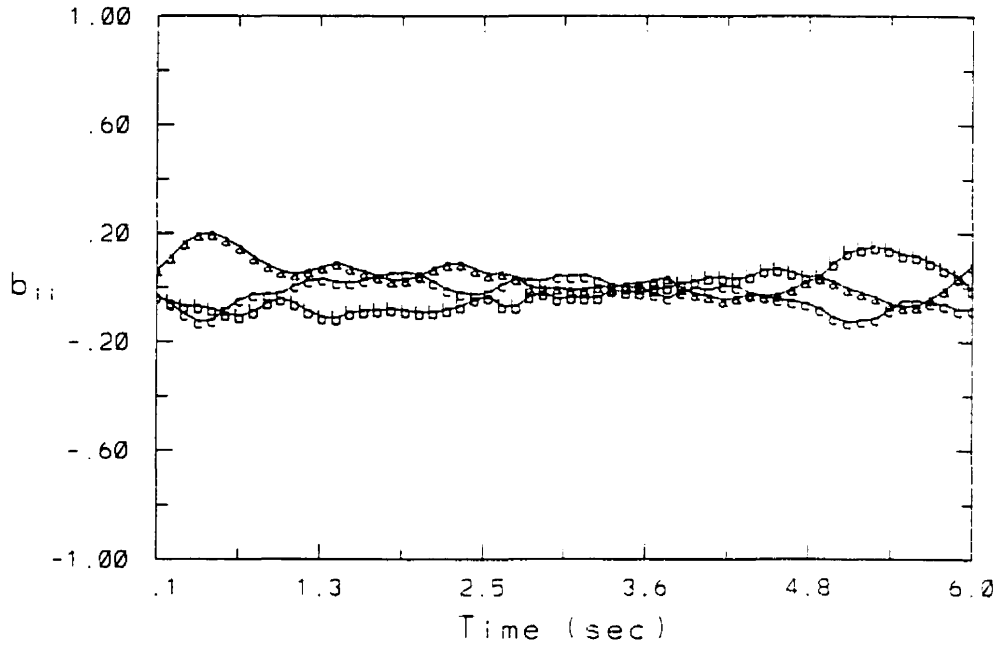

Figure 7.2: Temporal evolution of the three diagonal elements of the anisotropy tensor for *flowC*, a is b_{11}, b is b_{22} and c is b_{33}.

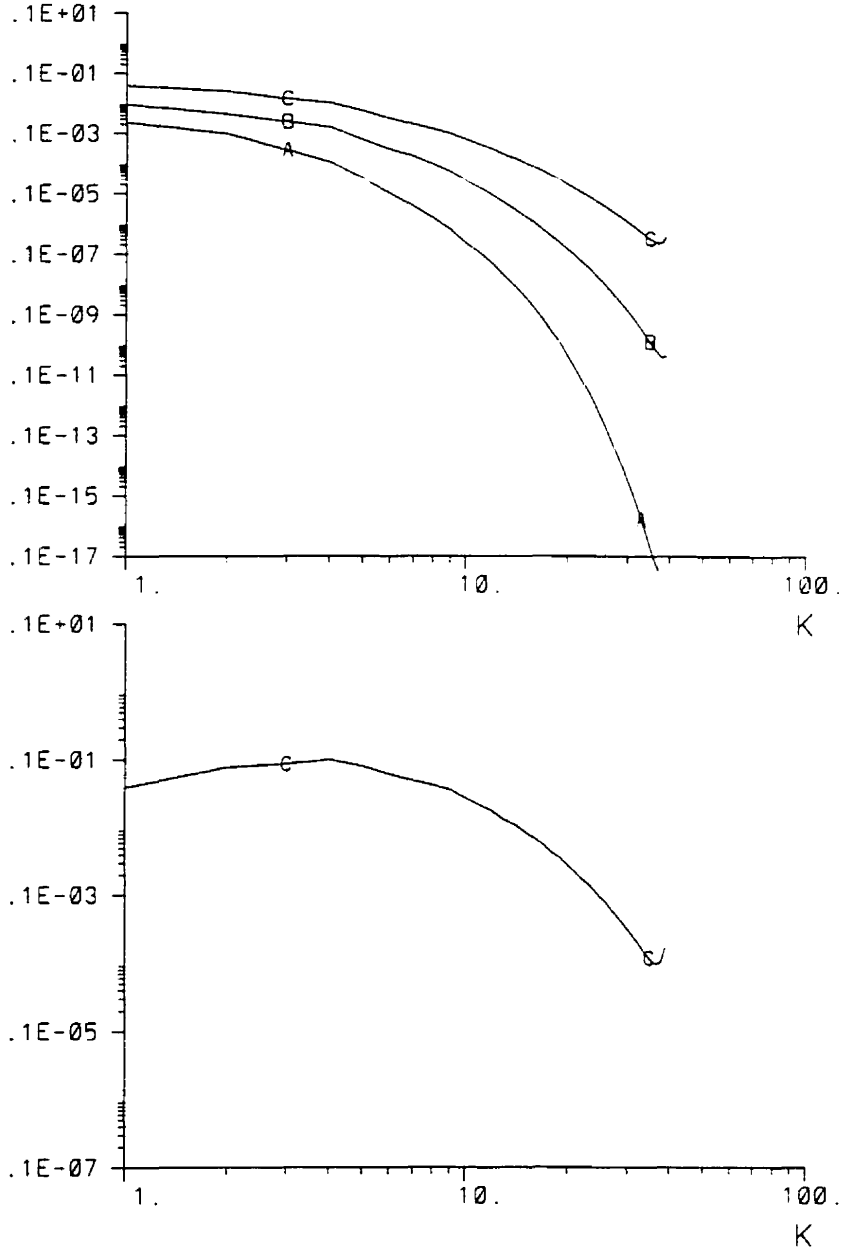

Figure 7.3: Top panel: three dimensional mean kinetic energy spectra for *flowA*(curve A), *flowB*(curve B) and *flowC*(curve C). Bottom panel: curve C multiplied by $K^{\frac{5}{3}}$. K is the magnitude of wavenumber in non-dimensional form.

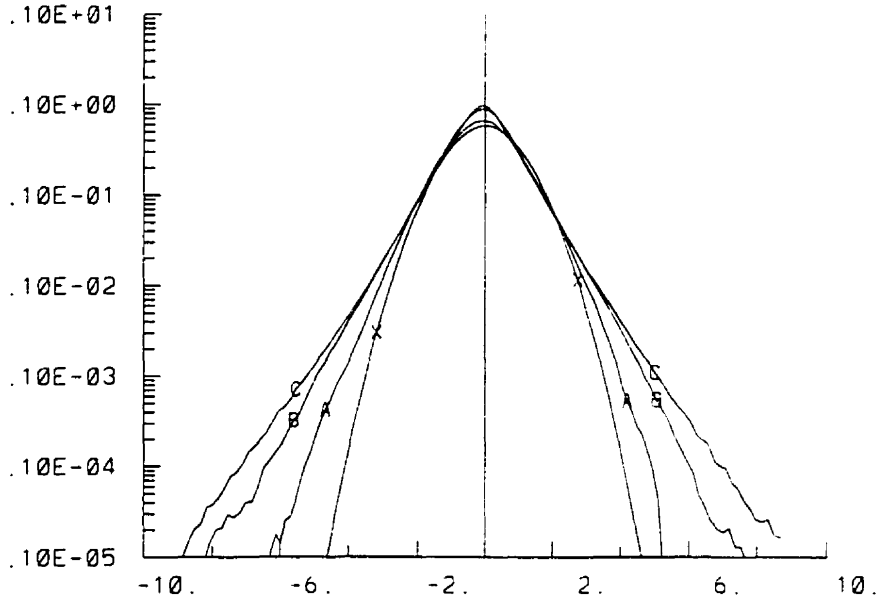

Figure 7.4: Time averaged normalized histograms (frequency distribution) of grid point values of one component of vorticity for the three flows (A, B and C). The ordinate is the fraction of the total number of grid points(1 grid point out of $80^3 = 2. \times 10^{-6}$). Each distribution has been normalized by its time averaged standard deviation. The abscissa is therefore multiples of the standard deviation for each curve. Reference curve X is a Gaussian distribution with unit standard deviation.

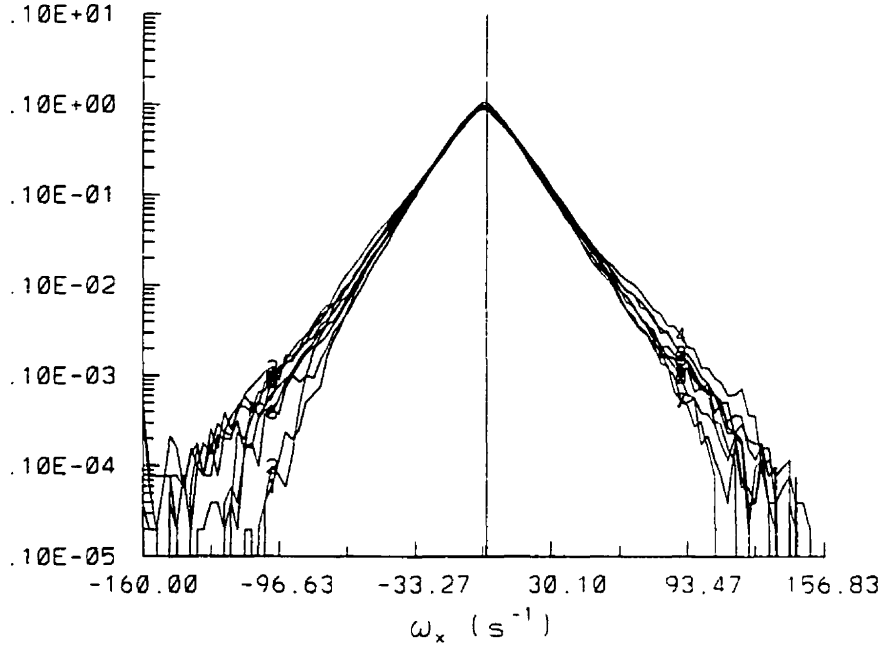

Figure 7.5: Histograms(frequency distributions) of grid point values of one component of vorticity in *flowC* every $2\tau_0$. The ordinate is the fraction of the total number of grid points(1 grid point out of $80^3 = 2. \times 10^{-6}$).

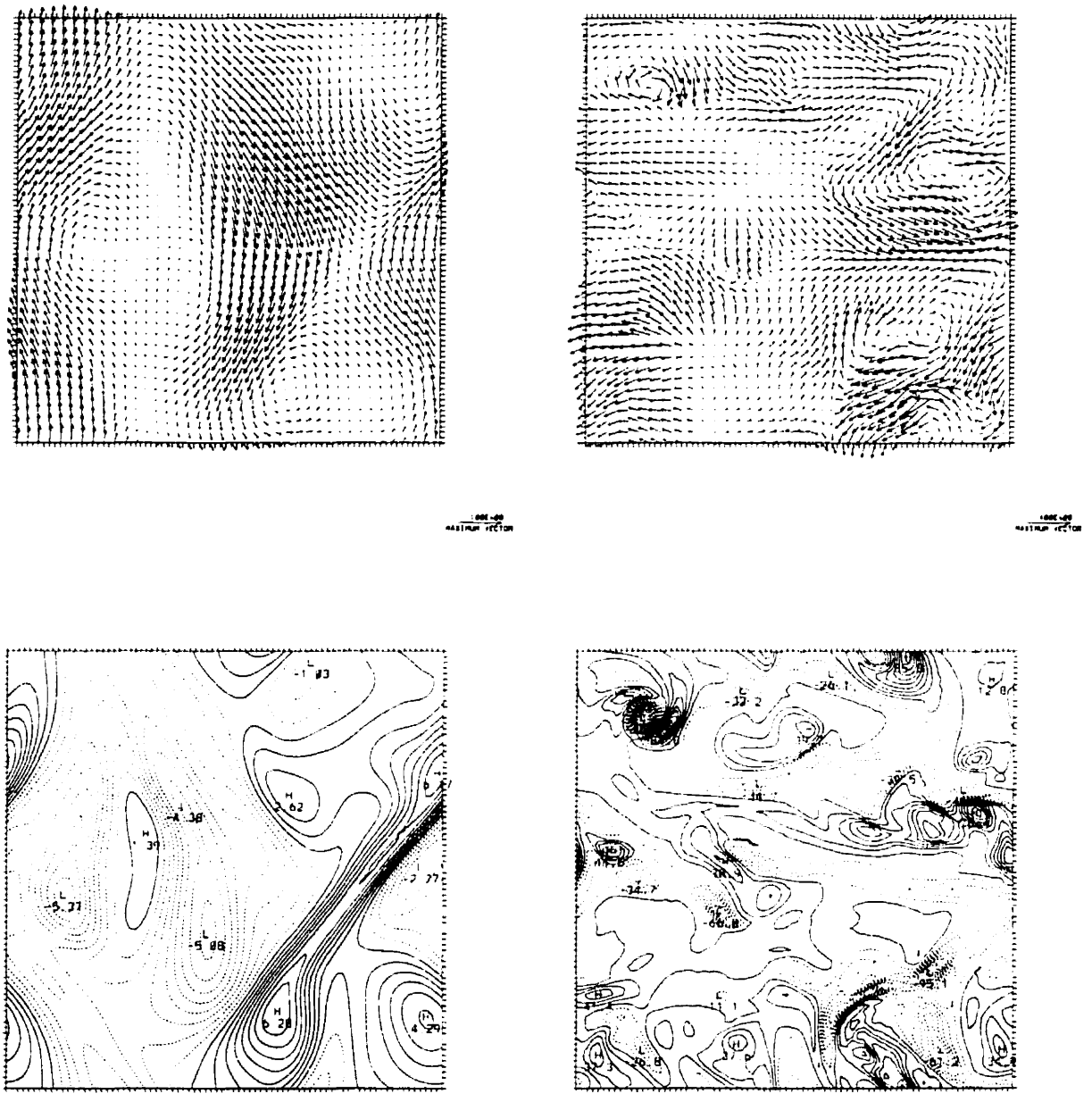

Figure 7.6: Velocity field cross section (top panels) and corresponding vorticity field cross section (bottom panels) for *flowA*(left panels) and *flowC*(right panels). The legend at the bottom right of each velocity plot indicates the magnitude of the velocity vector (in ms^{-1}). Negative vorticity lines are drawn with a dashed line pattern. The vorticity contour intervals are $.75s^{-1}$ and $10s^{-1}$ for *flowA* and *flowC* respectively.

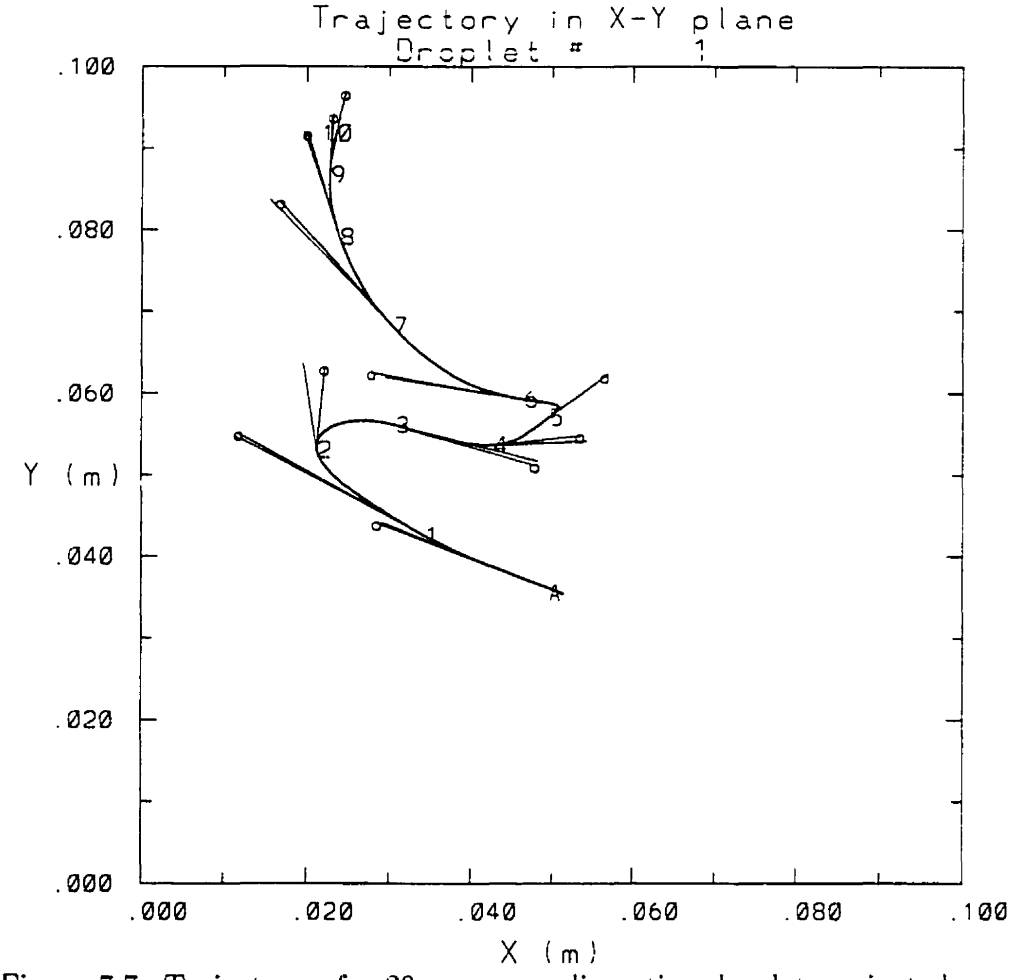

Figure 7.7: Trajectory of a $20\mu m$ non sedimenting droplet projected on a 2D plane over $.8s$ in *flowC*. The trajectory is sampled every $.008s$. The letter indicates the initial position. The numbers indicate the successive position of the droplet every $.08s$. The 2D projection of the fluid velocity and the droplet velocity at the positions indicated with a letter and with numbers is shown by the orientation and length(vector of length $1cm$ corresponds to speed of $\approx 10cms^{-1}$) of the straight lines originating at these points. The lines that end with a circle are for the fluid velocity.

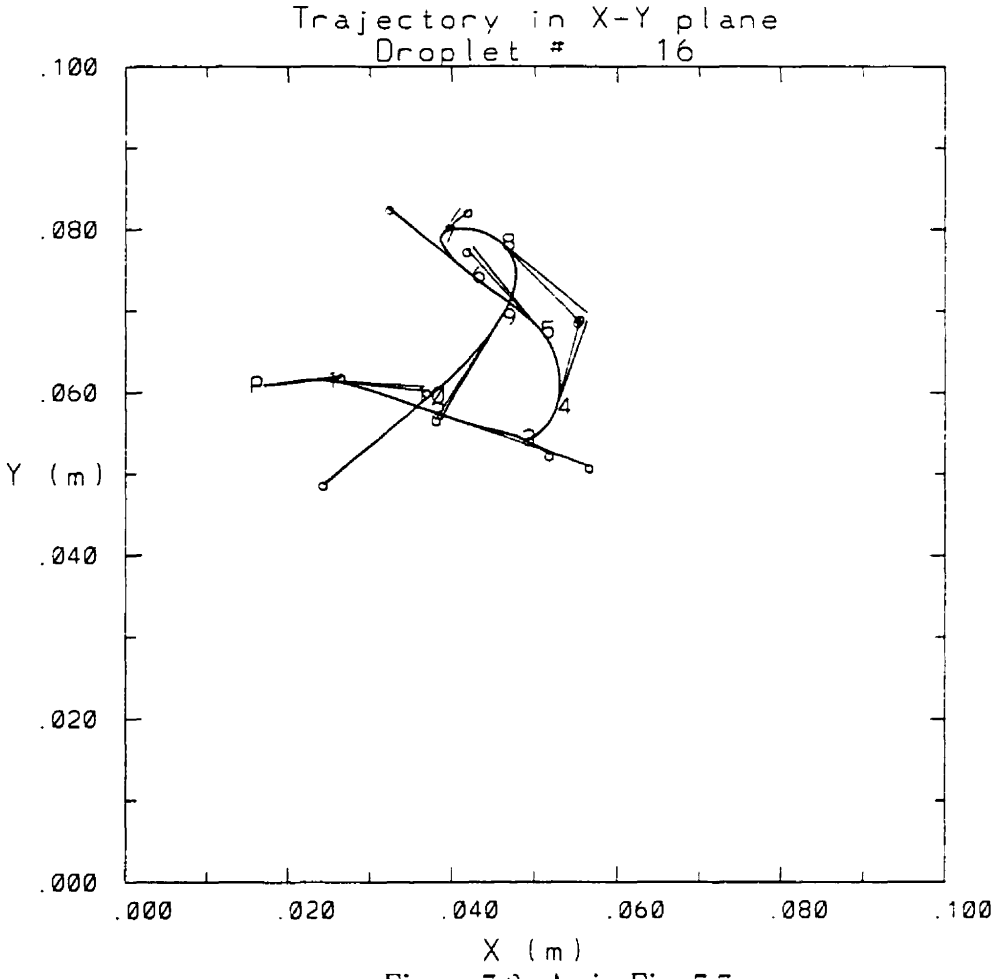

Figure 7.8: As in Fig. 7.7.

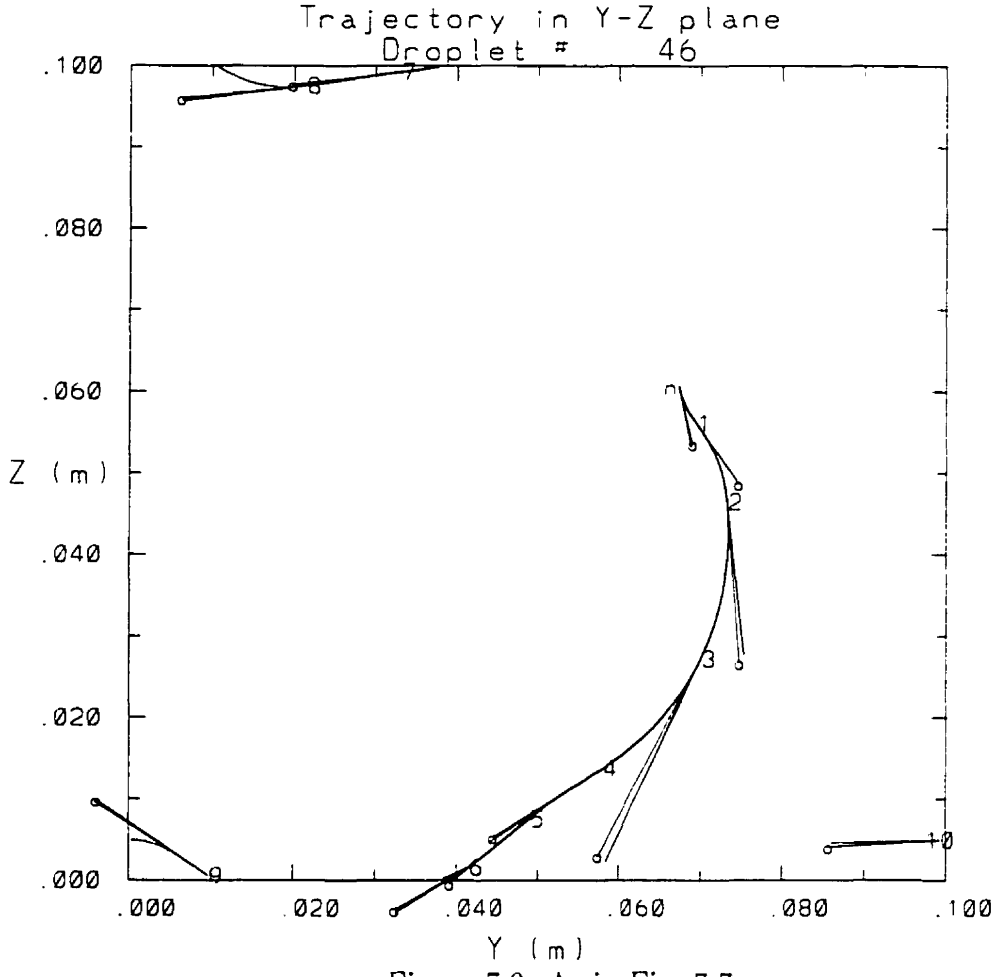

Figure 7.9: As in Fig. 7.7.

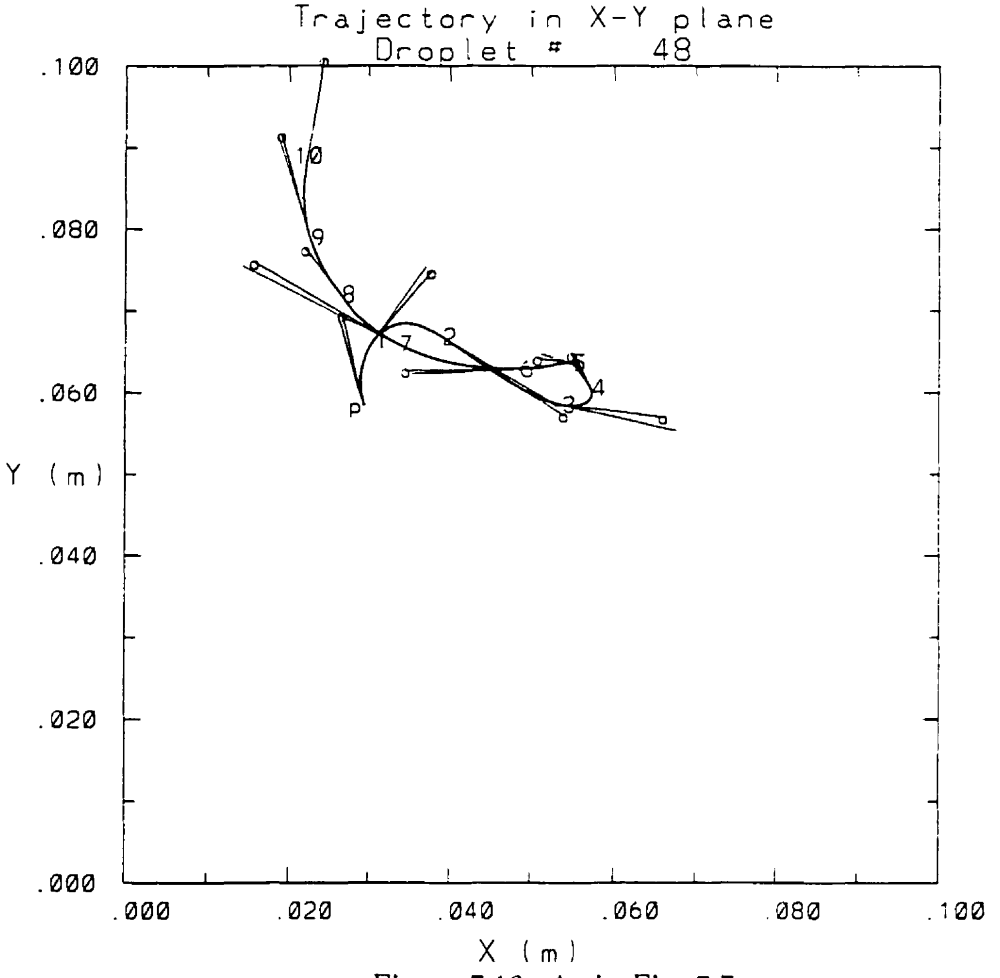

Figure 7.10: As in Fig. 7.7.

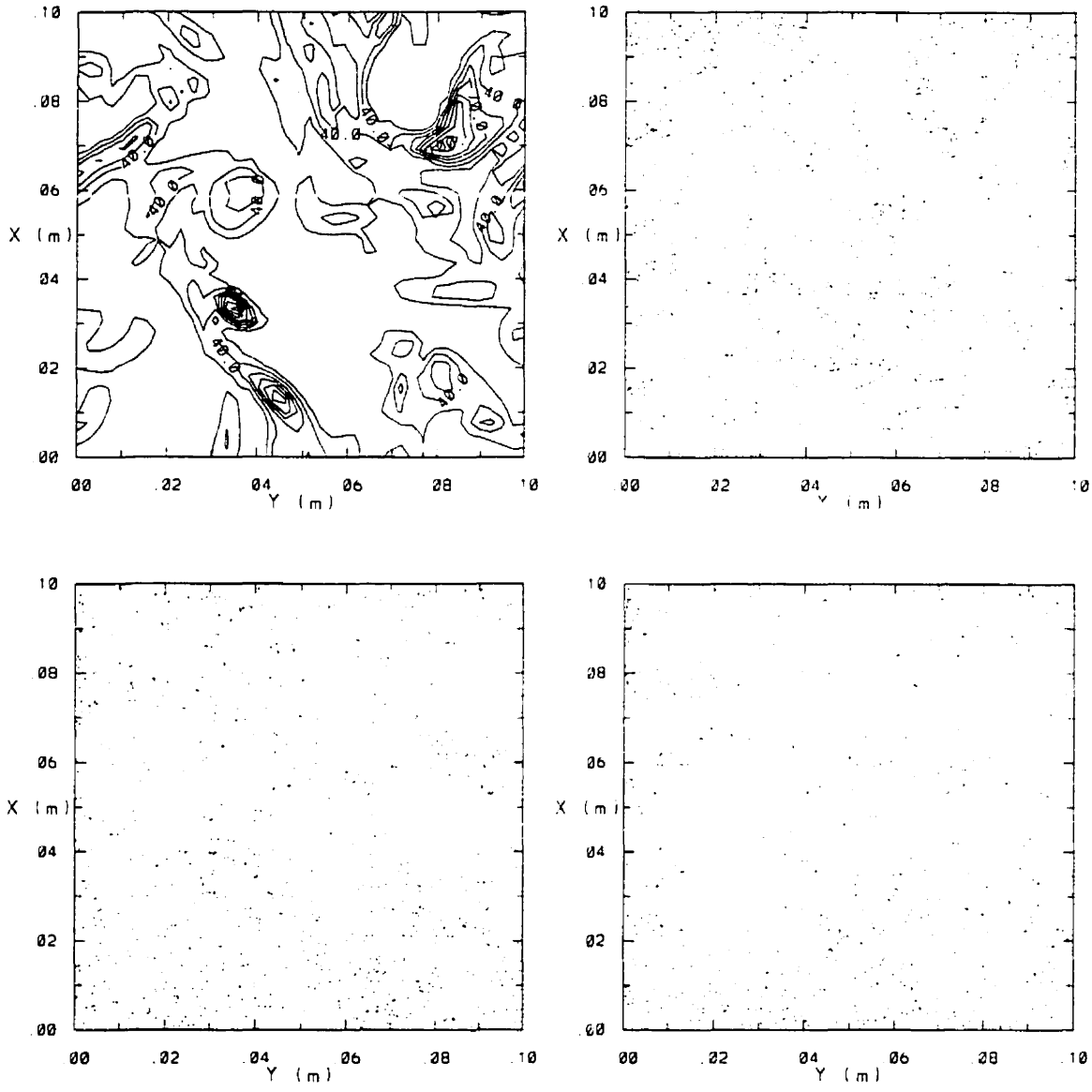

Figure 7.11: *iniCnosed*: Top left panel: cross section of field of vorticity magnitude. The minimum contour line is $25.s^{-1}$, which approximately corresponds to the spatial average of the vorticity magnitude, while the contour interval is $15.s^{-1}$, which approximately corresponds to its standard deviation. Top right panel: Position of each $20\mu m$ droplet in same cross section. Bottom left panel is for $15\mu m$ droplets while bottom right is for $10\mu m$ droplets.

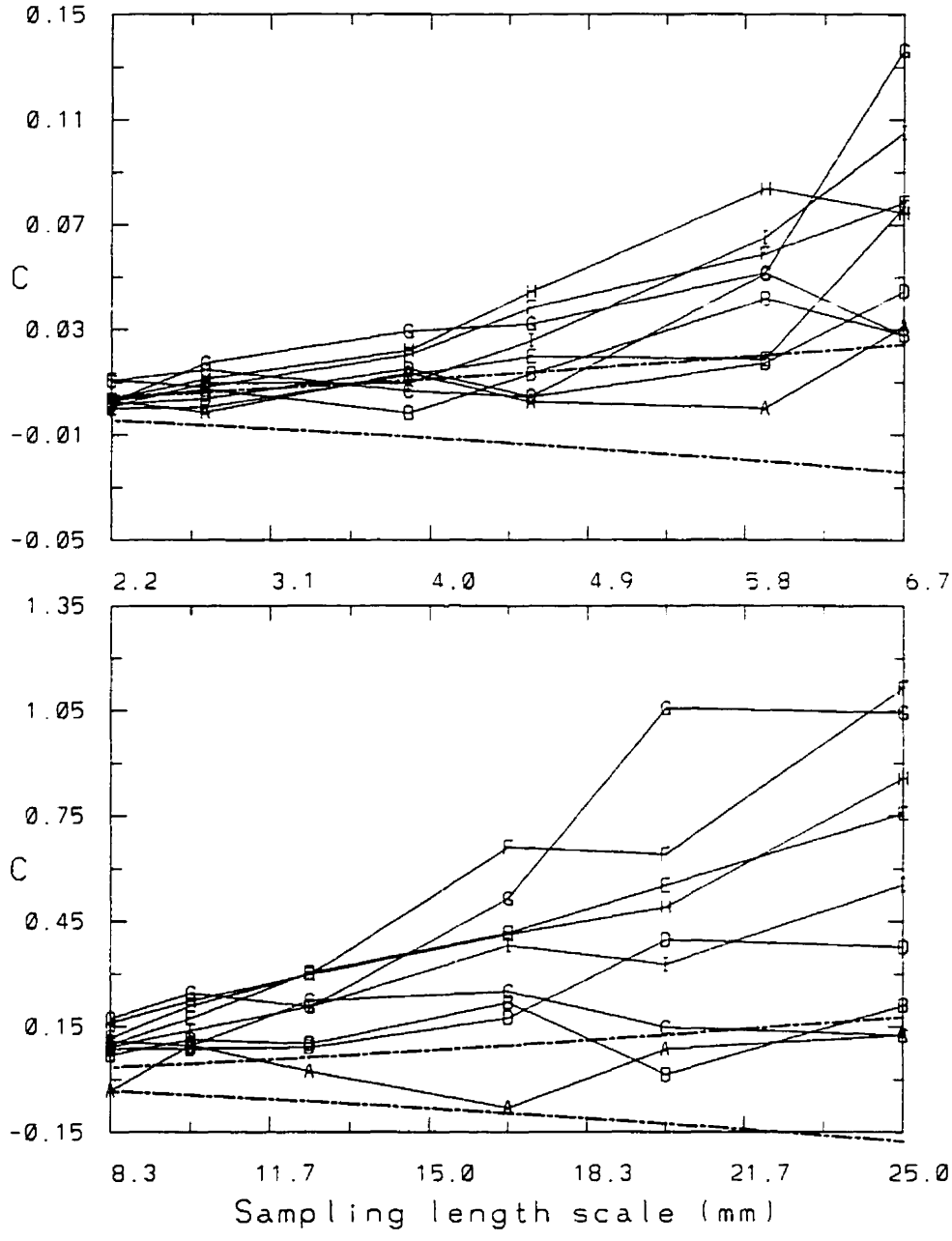

Figure 7.12: *iniAnosed*:Clustering index as a function of the sampling length scale . The length scale of the twelve sampling volume sizes used corresponds to the position of the letters along the abscissa. Curves are plotted at each $.5\tau_0$, from $t = .5\tau_0$ (curve A) to $t = 5\tau_0$ (curve J). The dashed lines correspond to $\pm\sqrt{2/N}$, the expected standard deviation of the statistical error on the clustering index related to the finite number of sampling volumes. N is the number of sampling volumes.

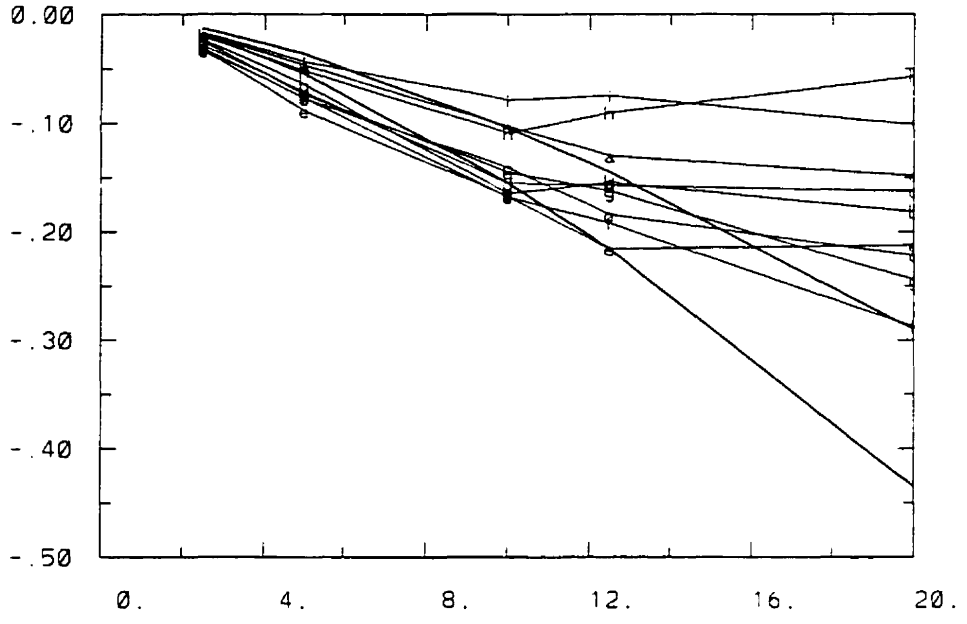

Figure 7.13: *iniAnosed*:Correlation between vorticity magnitude and number of droplets, $r(|\omega|, n)$, as a function of the length scale of the sampling volume. The length scale of the five sampling volume sizes used corresponds to the positions of the letters along the abscissa. Curves are plotted every $.5\tau_0$, from $t = .5\tau_0$ (curve a) to $t = 5\tau_0$ (curve i). The top dashed line links the correlations which have a probability of 10^{-3} of resulting from the correlation of two finite uncorrelated signals. The bottom dashed line is for a probability of 10^{-6}.

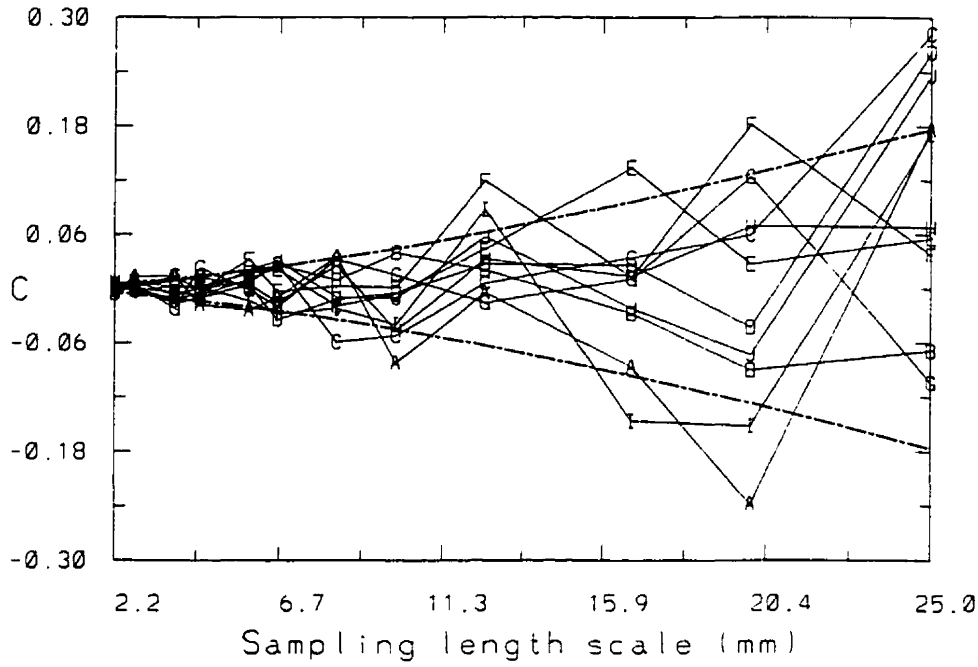

Figure 7.14: *iniAsed*:As in Fig. 7.12.

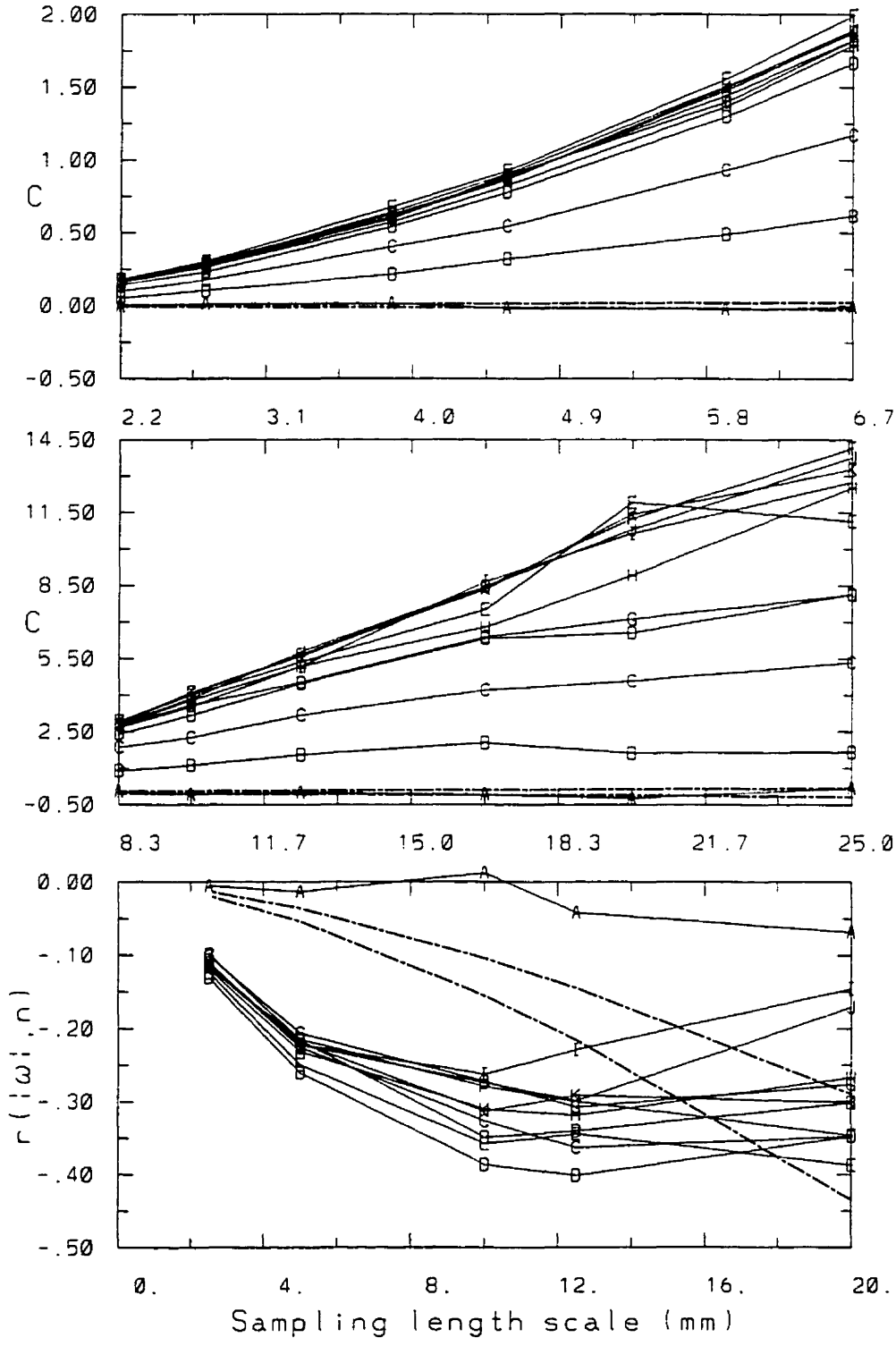

Figure 7.15: Top two panels: same as Fig. 7.12 for $20\mu m$ sedimenting droplets in *flowC*. Curve A is at $t = 0$. Bottom panel: same as 7.13 for $20\mu m$ sedimenting droplets in *flowC*.

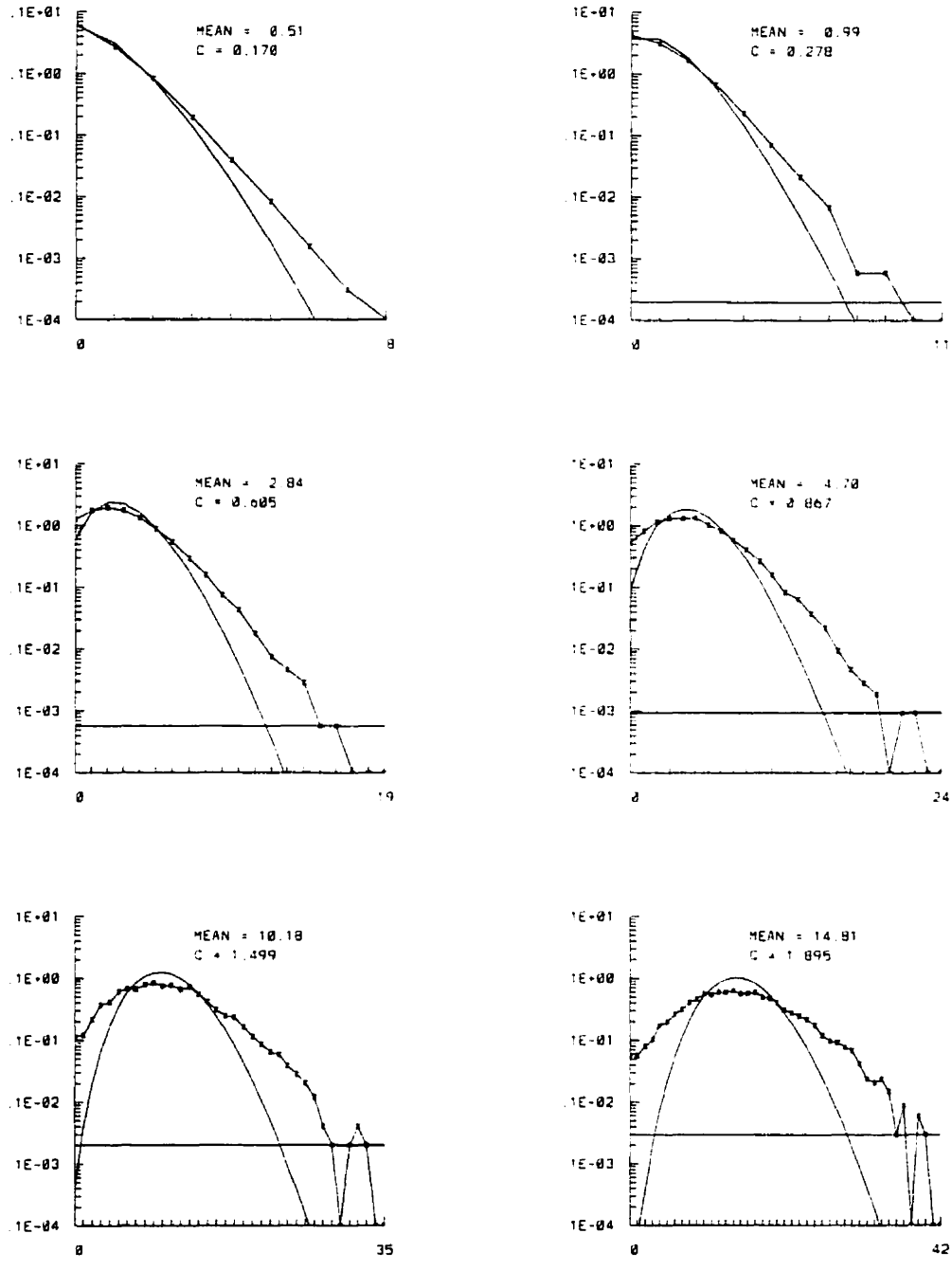

Figure 7.16: Histograms of fractions of sampling volumes (ordinate) containing a certain number of droplets (abscissa) for the six sampling length scales in the top panel of Fig. 7.15. Unmarked solid curves are the reference Poisson distribution with the same mean. The horizontal line represents the reciprocal of the total number of sampling volumes.

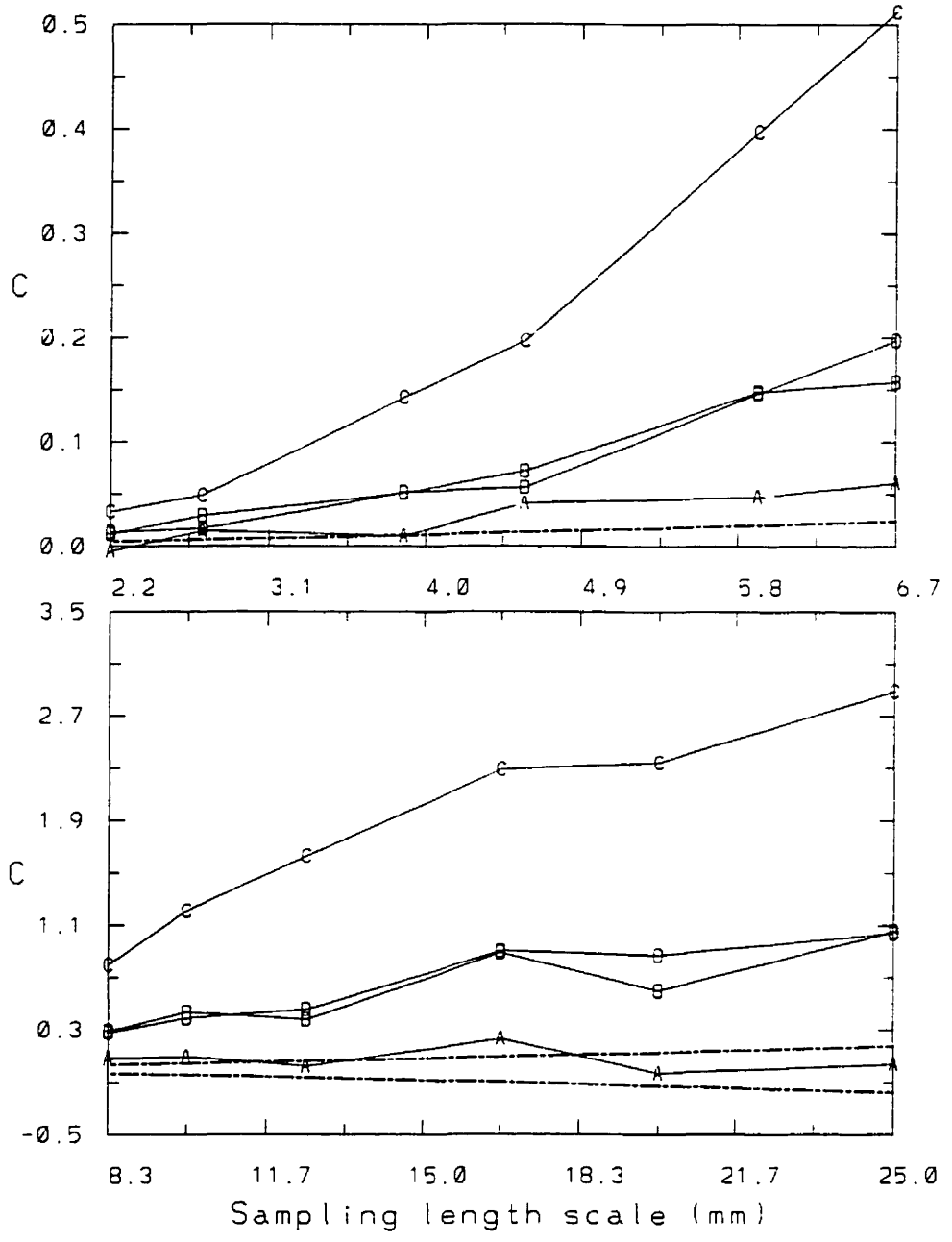

Figure 7.17: *iniBnosed*:Clustering index as a function of the sampling length scale at the final time (see caption of Fig. 7.12). Curves A,B and C are for the $10, 15$ and $20\mu m$ monodispersed size distributions while curve D is for the uniform size distribution.

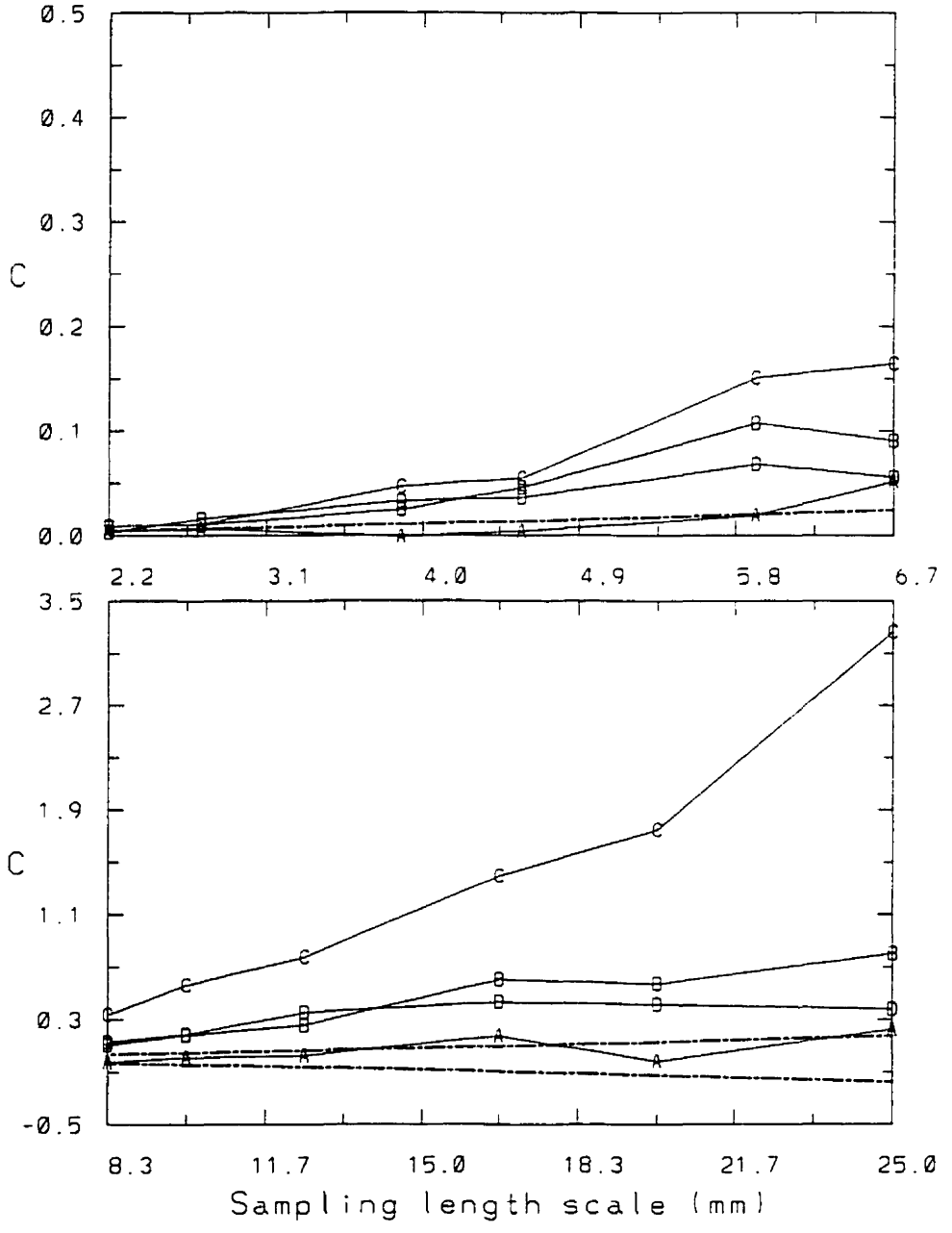

Figure 7.18: *iniBsed*: As in Fig. 7.17

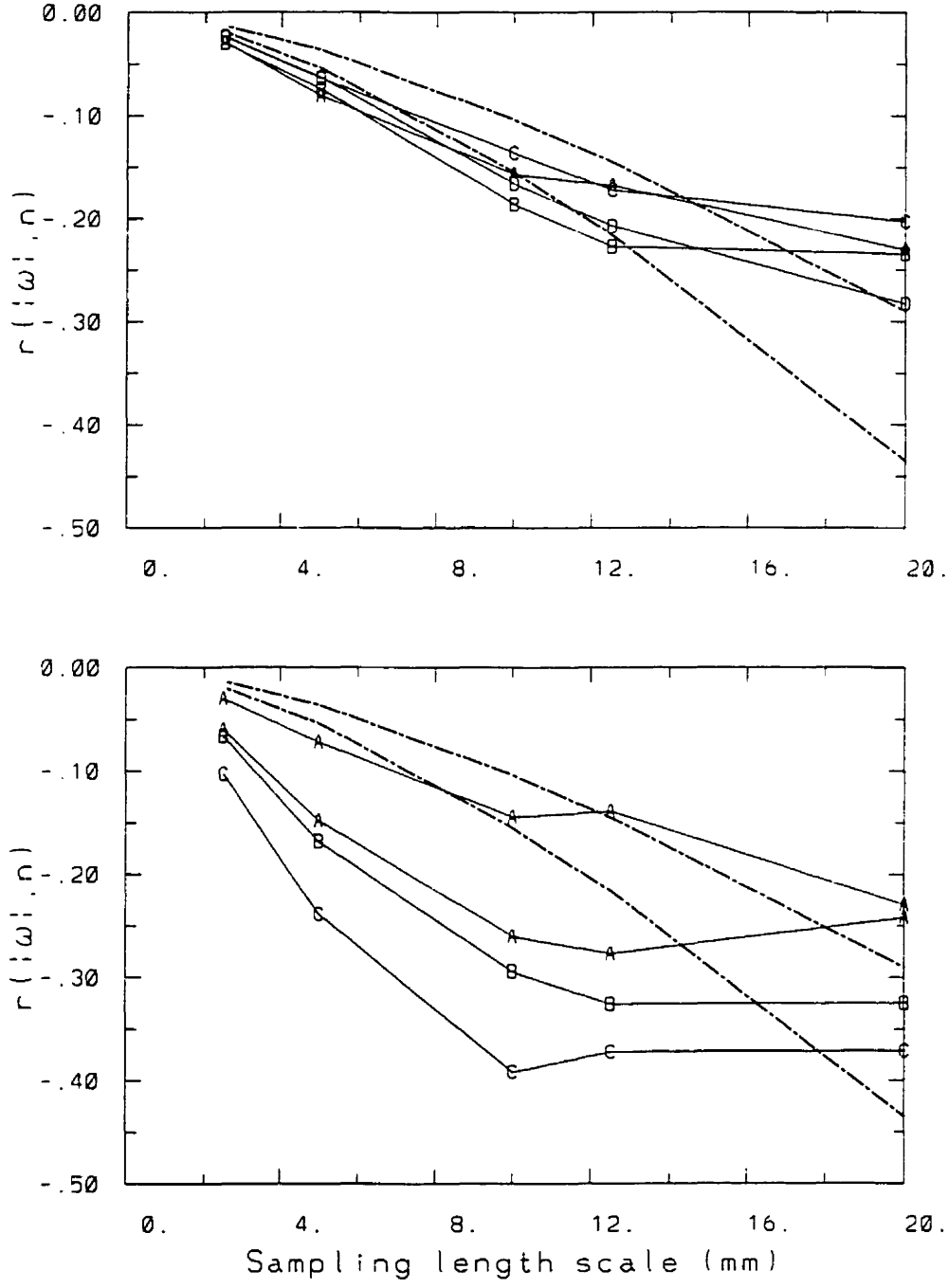

Figure 7.19: *iniBsed*(top panel)– *iniBnosed*(bottom panel): $r(|\omega|, n)$ at the final time (see caption of Fig. 7.13). Curves A,B and C are for the 10, 15 and 20μm monodispersed size distributions while curve D is for the uniform size distribution.

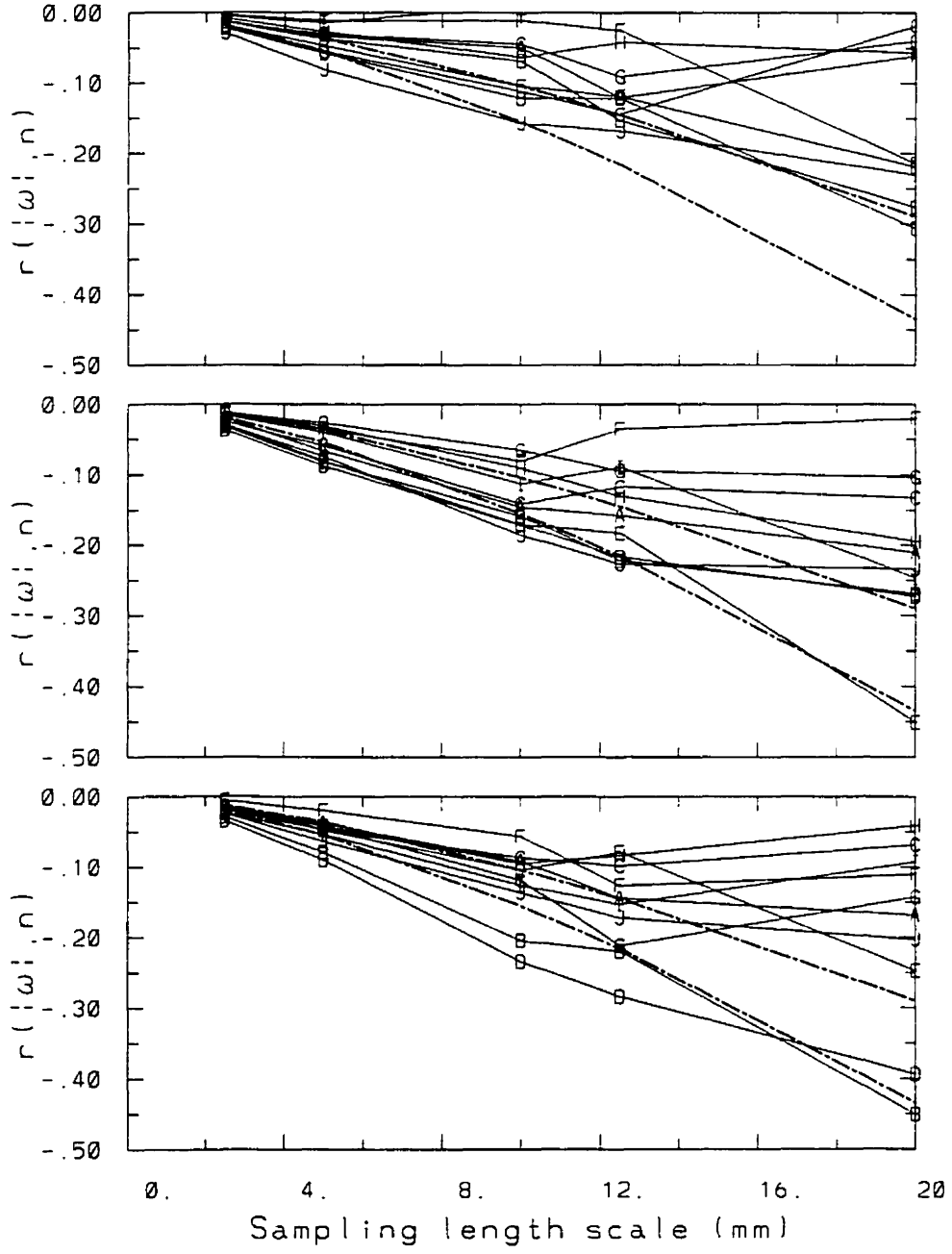

Figure 7.20: *iniBsed*: $r(|\omega|, n)$ as in Fig. 7.13, for the $10, 15$ and $20\mu m$ monodispersed size distributions(top, middle and bottom panels) from $t = 1.4\tau_0$(curve A) to $t = 14\tau_0$(curve J), at every $1.4\tau_0$.

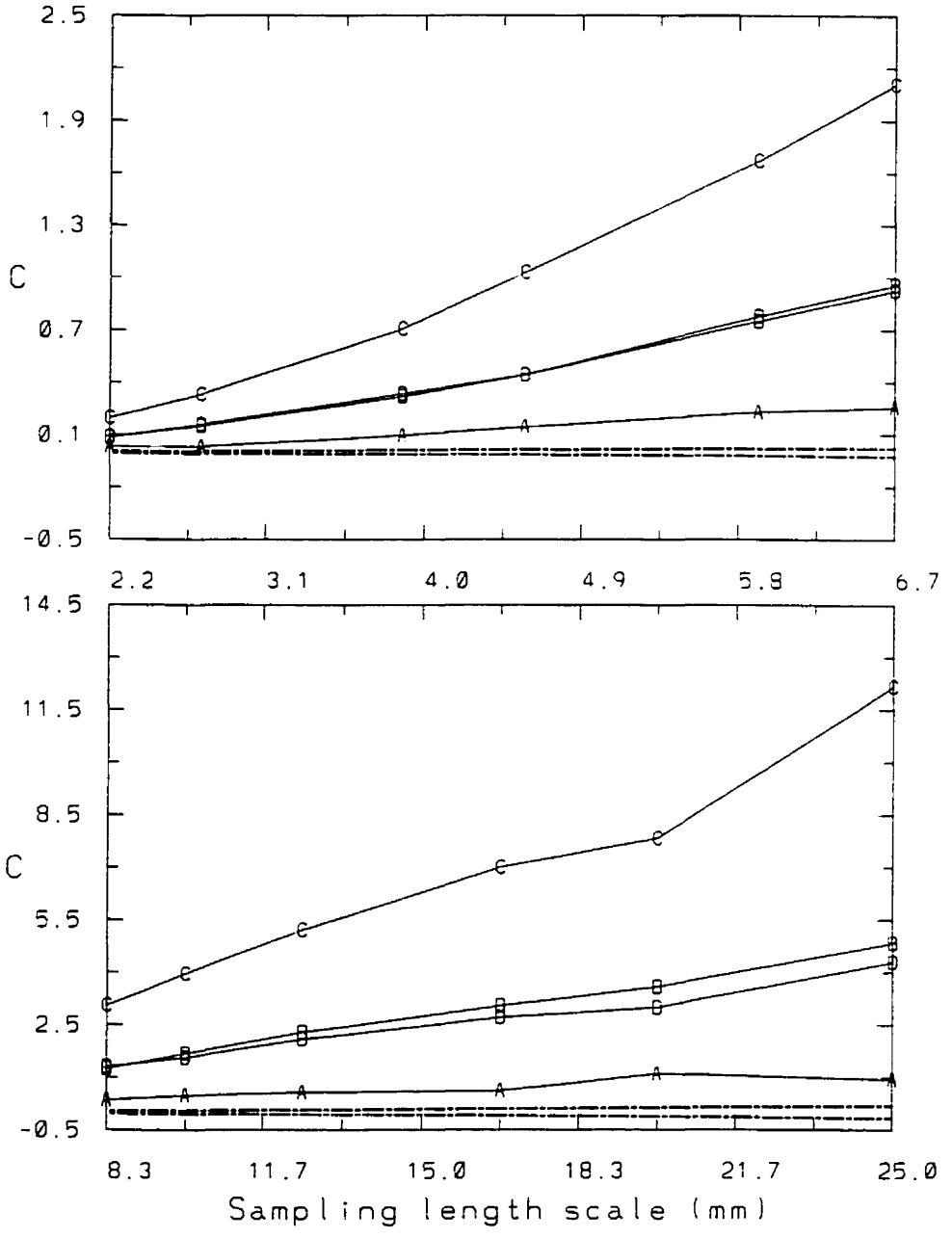

Figure 7.21: *iniCnosed*:As in Fig. 7.17.

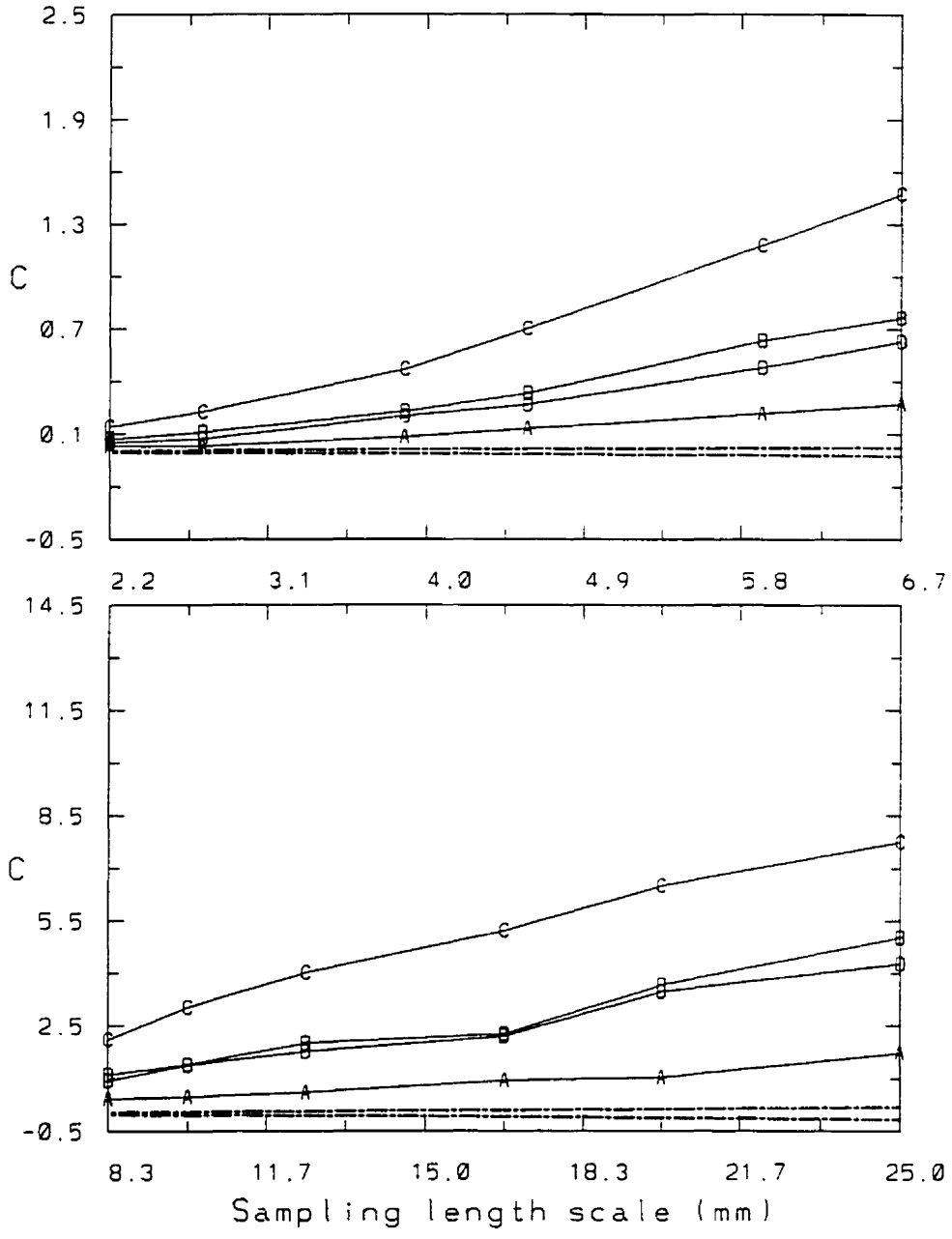

Figure 7.22: *iniCsed*:As in Fig. 7.17

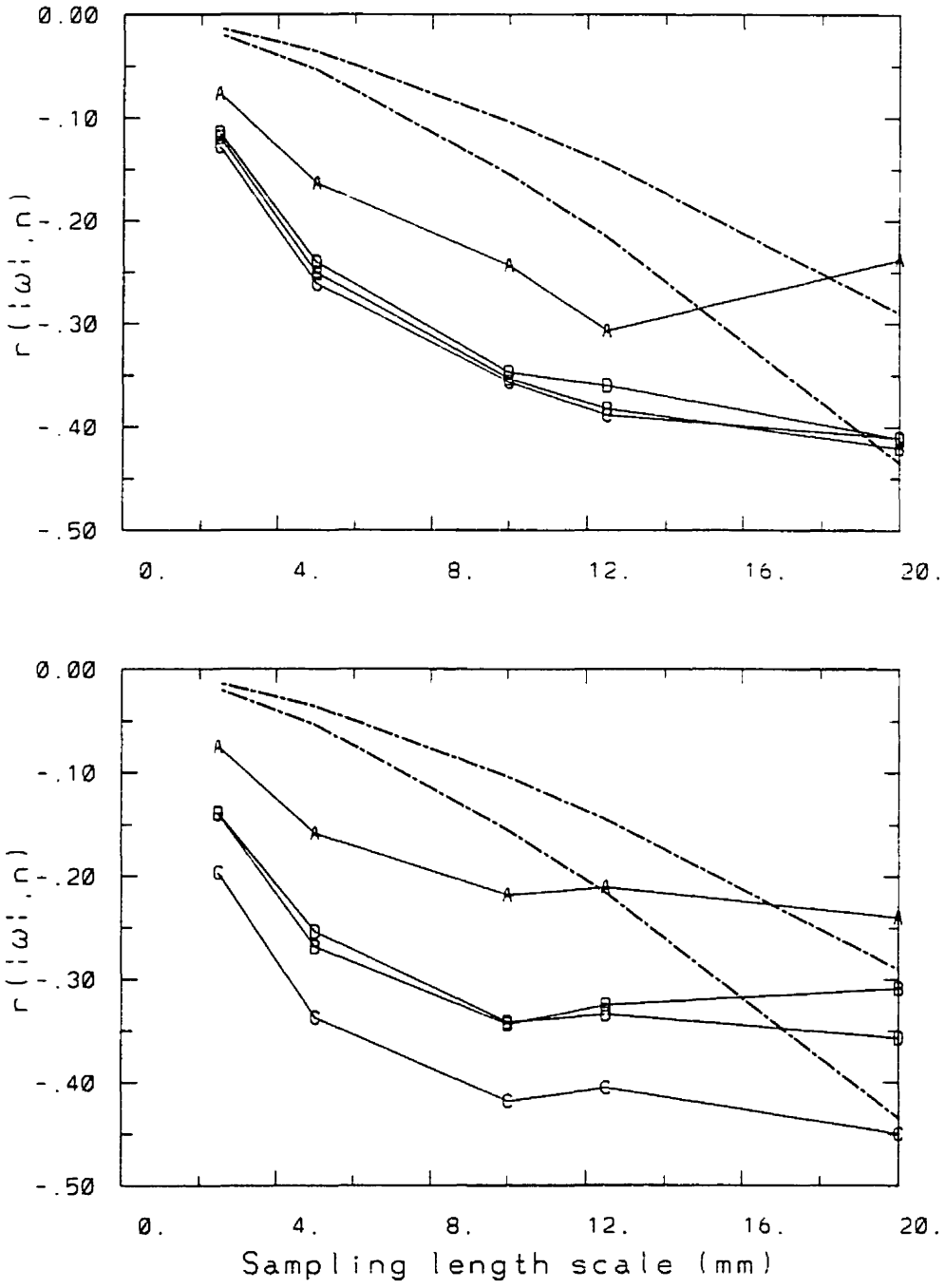

Figure 7.23: *iniCsed*(top panel)– *iniCnosed*(bottom panel):As in Fig. 7.19.

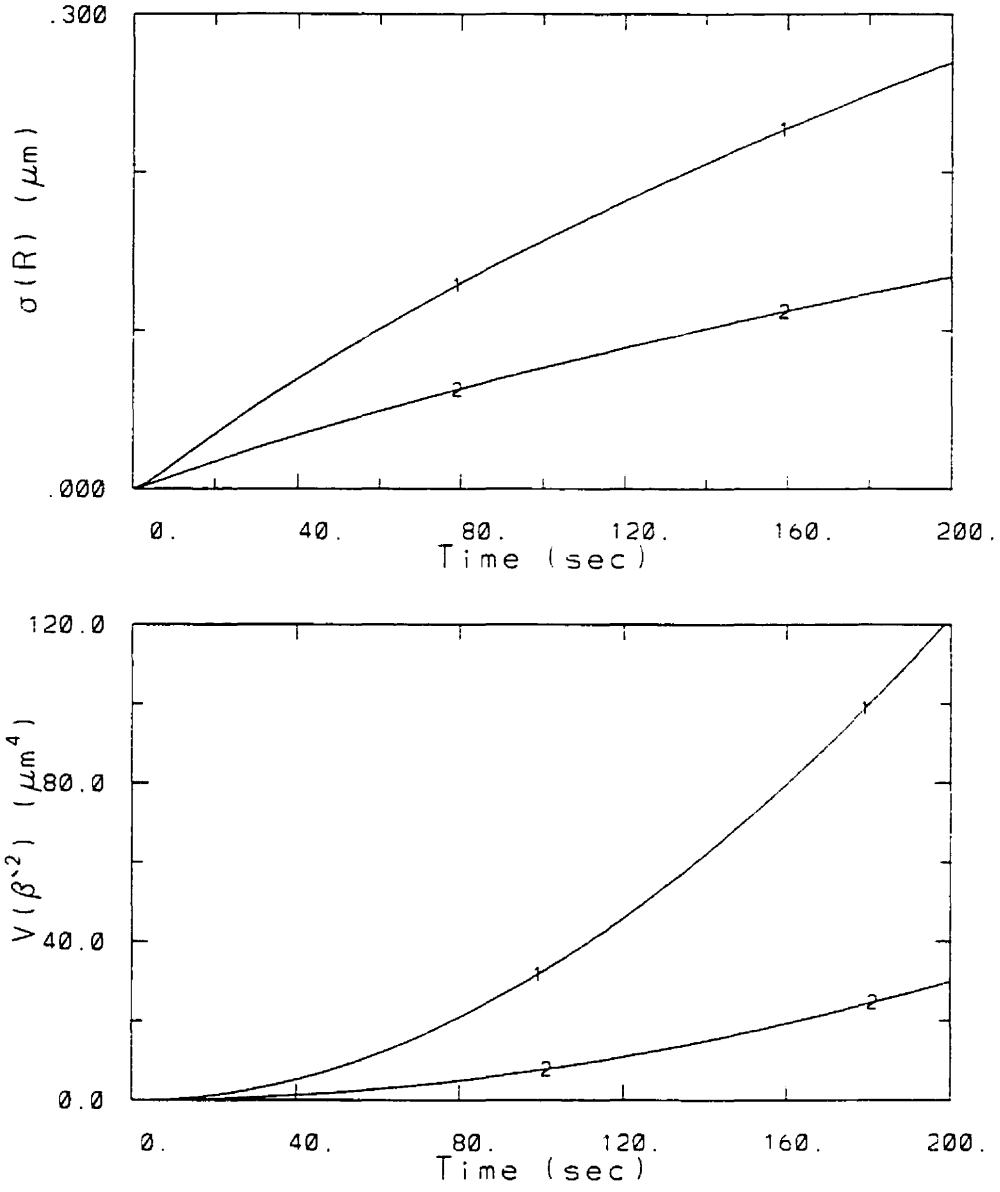

Figure 7.24: Time evolution of standard deviation of size distribution (top panel) and variance of perturbation degree of growth (bottom panel) for two reference experiments ($R1$ and $R2$) with no turbulence. Curve 1($R1$) uses the spatial distribution of the $15\mu m$ droplets produced in *iniCnosed*, while curve 2($R2$) results from a random spatial distribution of droplets

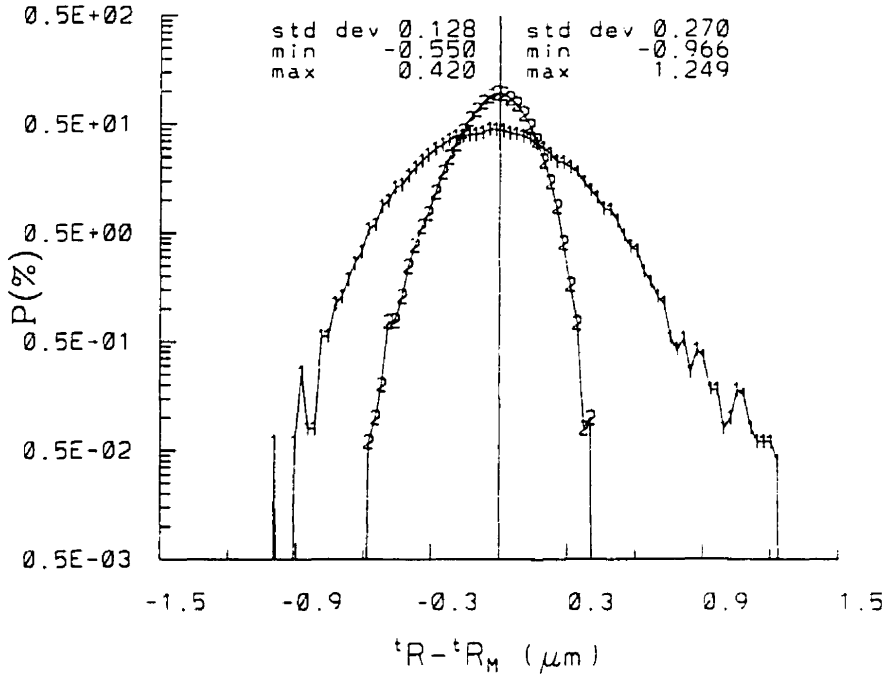

Figure 7.25: Probability distribution of ${}^tR - {}^tR_M$ for the two reference experiments ($R1$ and $R2$) with no turbulence. Curve 1($R1$) (statistics on top right) uses the spatial distribution of the $15\mu m$ droplets produced in *iniCnosed*, while curve 2($R2$) (statistics on top left) results from a random spatial distribution of droplets

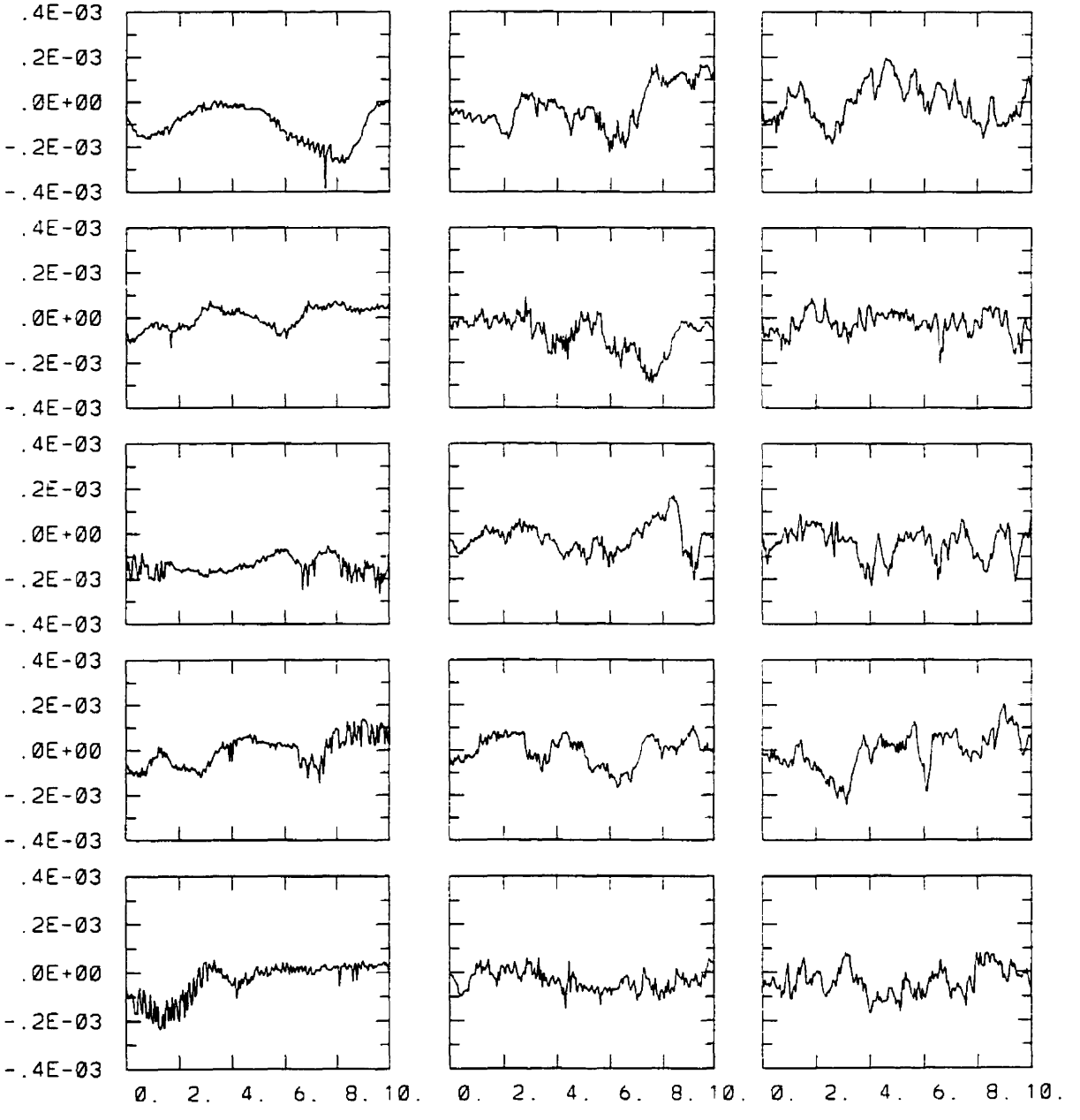

Figure 7.26: Temporal evolution over $10s$ of the supersaturation perturbation (S') for five droplets in Aa (left column), Bd (middle column) and Ch (right column).

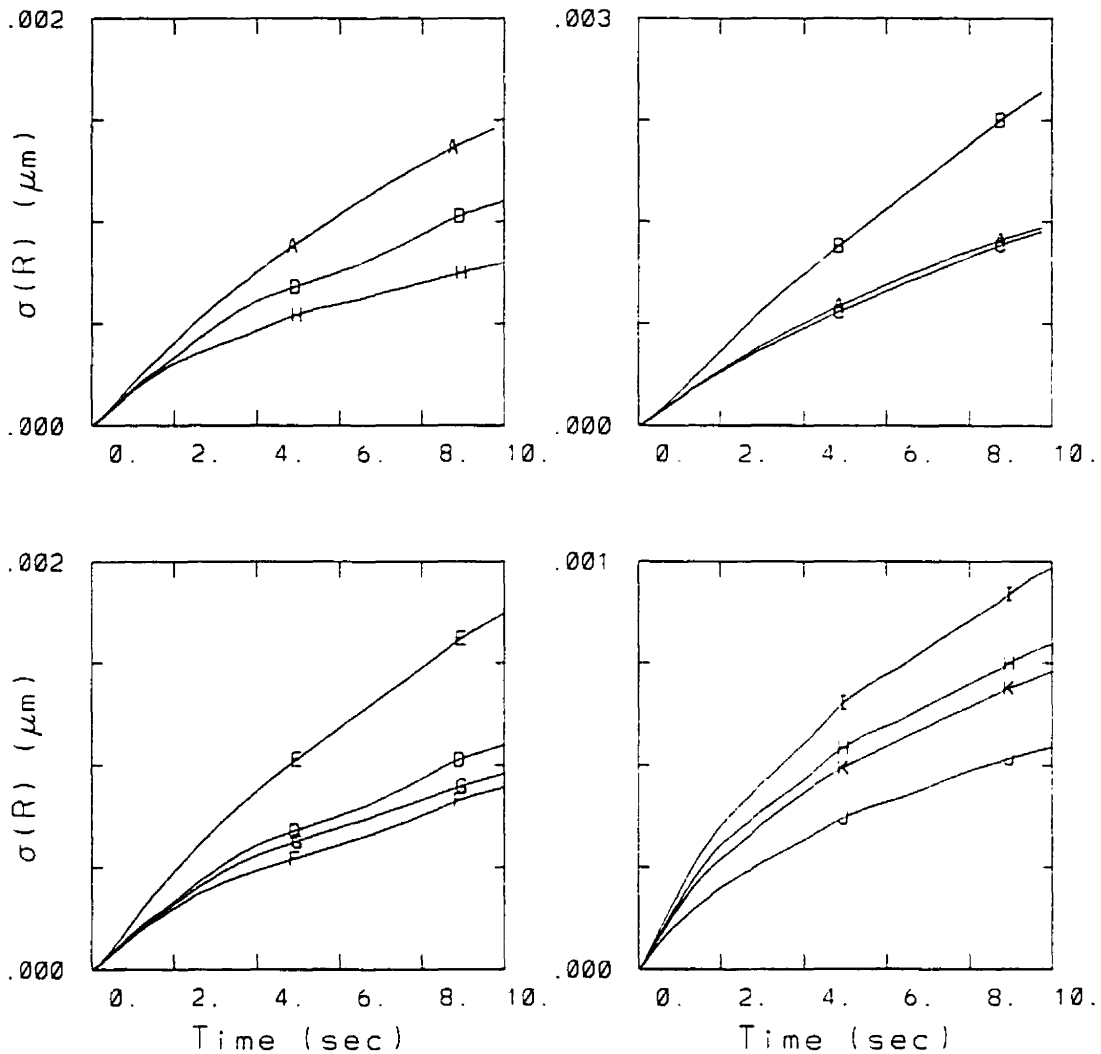

Figure 7.27: Temporal evolution of the standard deviation of the size distribution for all experiments with turbulence in Table 7.5. The letters identifying the curves correspond to the last letters of the name of the experiments. The top right panel shows experiments with *flowA*, the bottom left with *flowB* and the bottom right panel with *flowC*. The top left panel compares the results for experiments *Aa*, *Bd* and *Ch*. Note that the scales are different for the different panels.

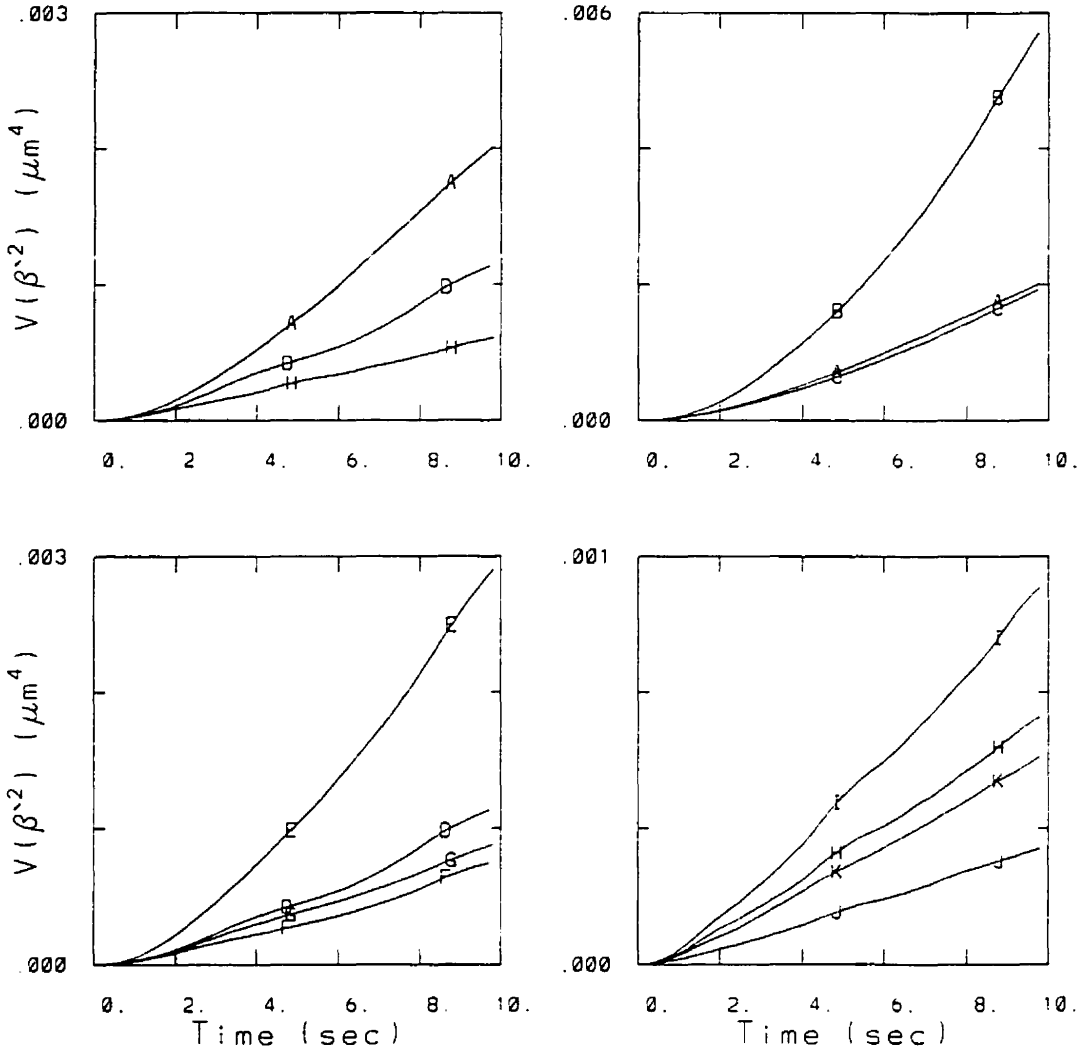

Figure 7.28: Temporal evolution of the variance of perturbation degree of growth for all experiments with turbulence in Table 7.5. The letters identifying the curves correspond to the last letters of the name of the experiments. The top right panel shows experiments with *flowA*, the bottom left with *flowB* and the bottom right panel with *flowC*. The top left panel compares the results of experiments *Aa*, *Bd* and *Ch*.Note that the scales are different for the different panels.

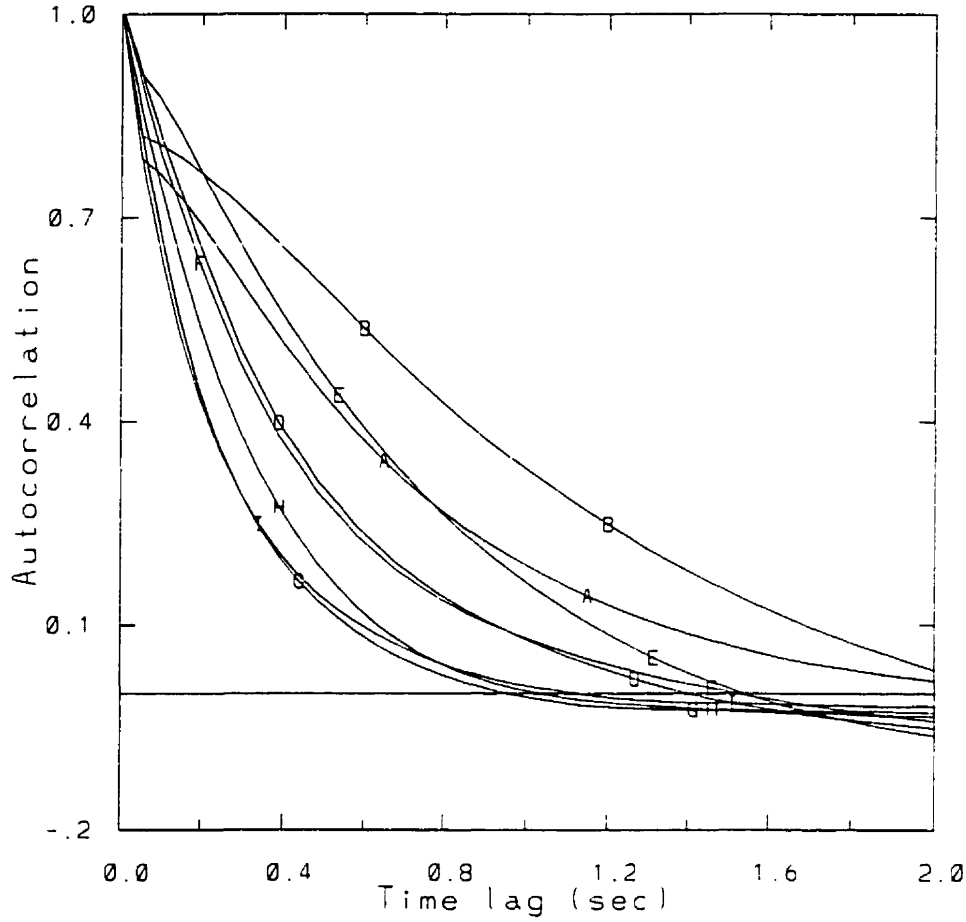

Figure 7.29: Autocorrelation, averaged over 2000 randomly chosen droplets, as a function of time lag (s) for for all experiments with turbulence in Table 7.5. The letters identifying the curves correspond to the last letters of the name of the experiments. The horizontal line represents zero autocorrelation.

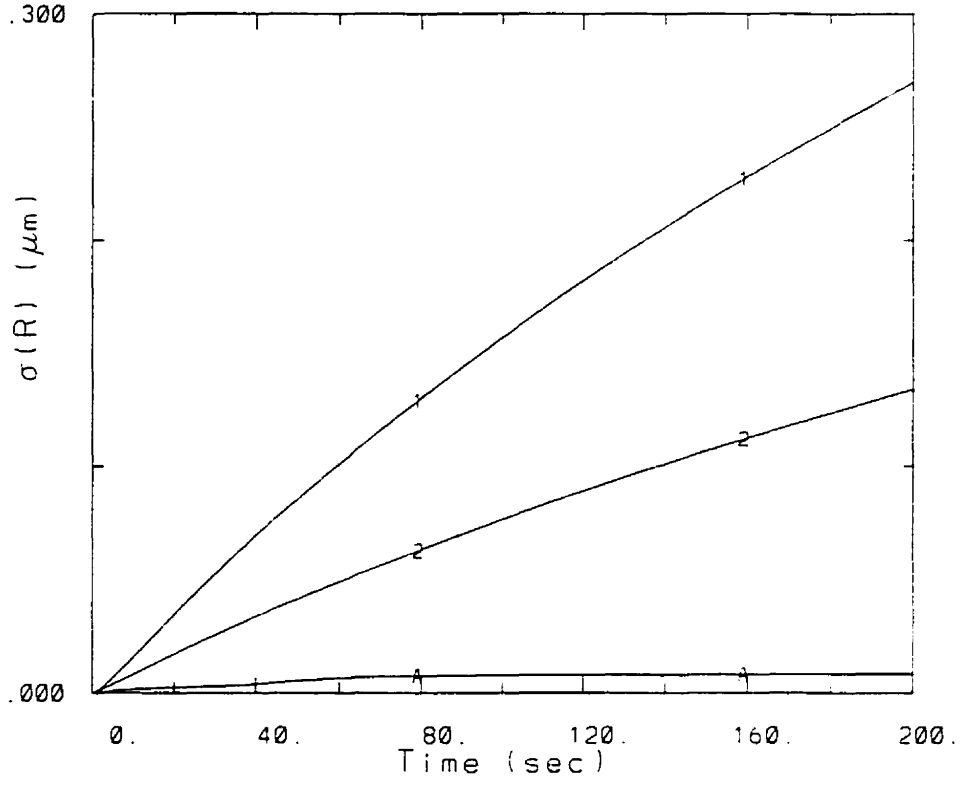

Figure 7.30: Temporal evolution of the standard deviation of the size distribution for the two reference experiments without turbulence, $R1$ (curve 1), $R2$ (curve 2) and for experiment Aa extended to 200 seconds (curve A).

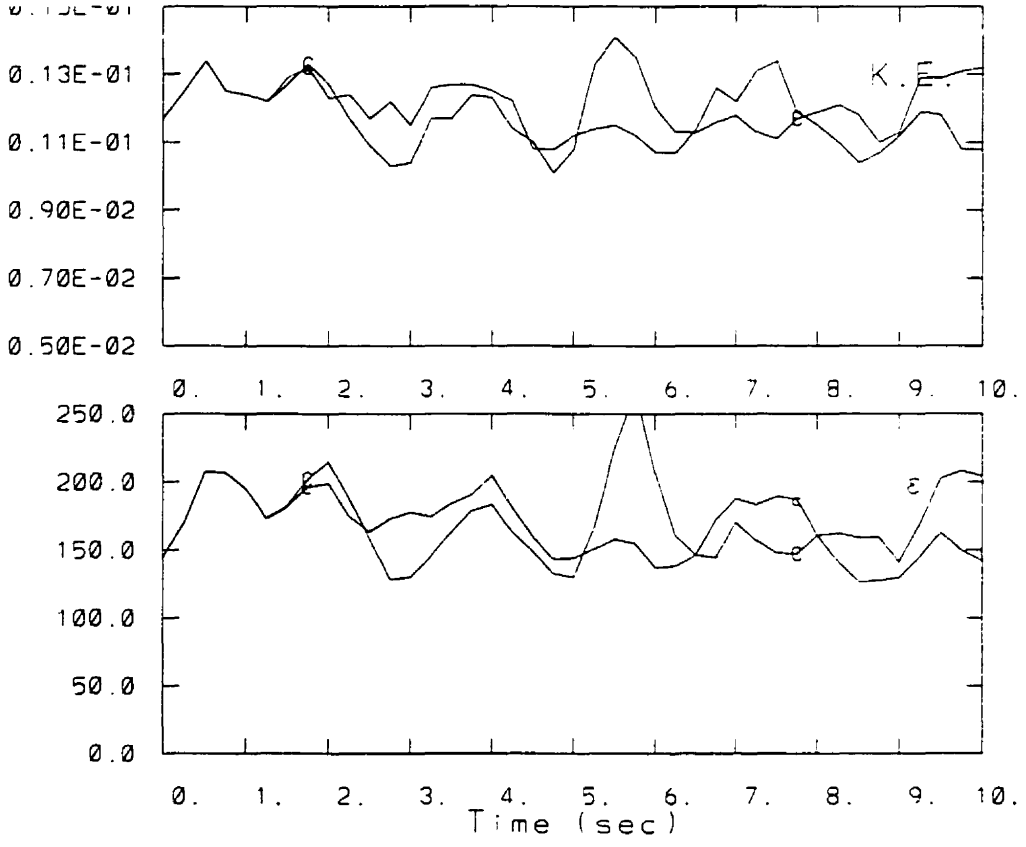

Figure 7.31: Temporal evolution of the mean kinetic energy per unit mass(K.E. in units of $m^2s^{-2}kg^{-1}$) and the mean eddy dissipation rate (ϵ in units of cm^2s^{-3}) for experiment Ch (curve C) and for the same experiment with inclusion of the buoyancy term in the flow equation (curve c).

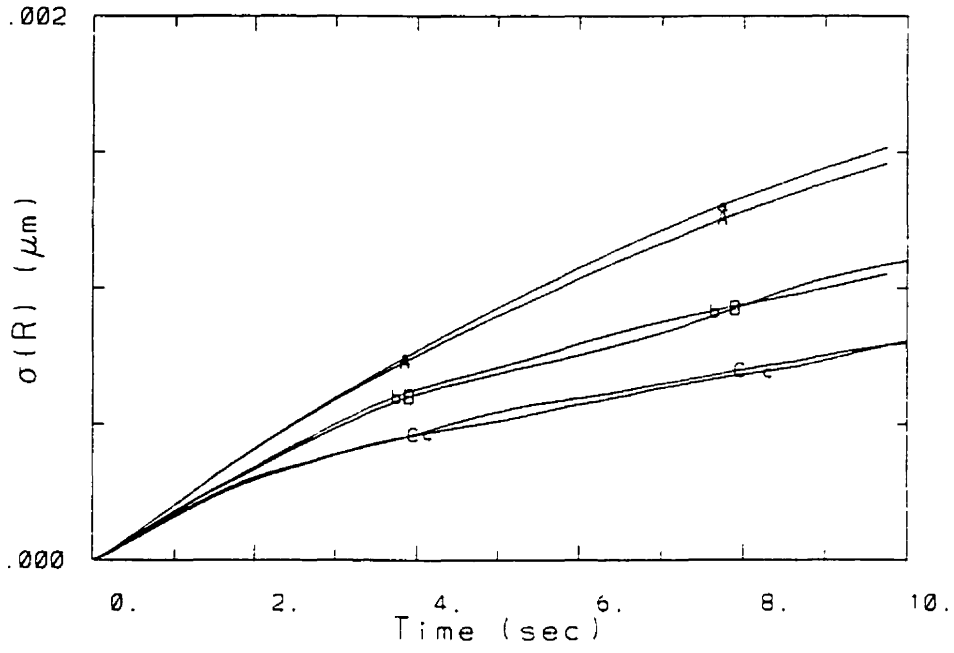

Figure 7.32: Temporal evolution of the standard deviation of the size distribution for experiments Aa, Bd and Ch (curves A, B and C) and for the same experiments with inclusion of the buoyancy term in the flow equation (curves a, b and c).

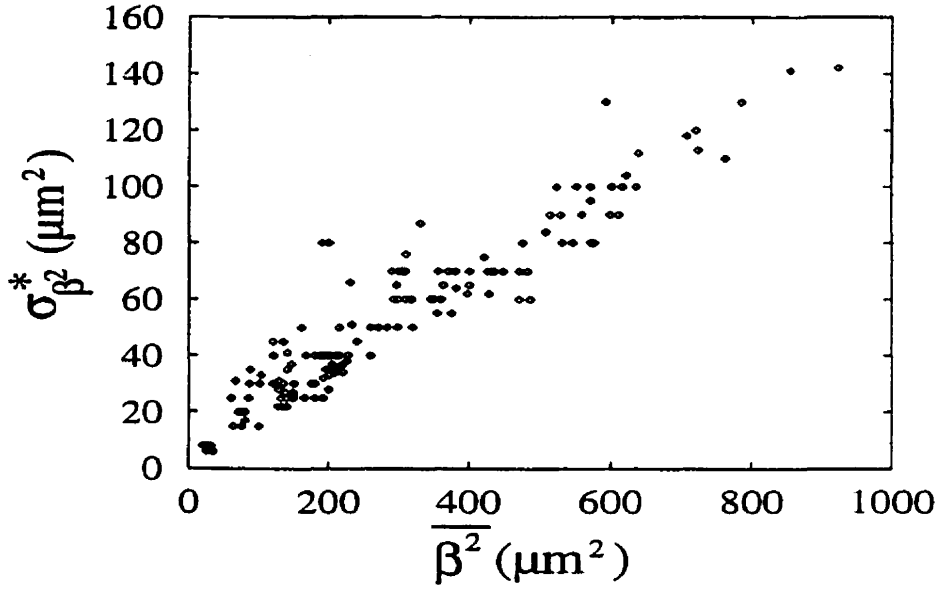

Figure 7.33: Spectrum broadening : $\sigma^*_{\beta^2}$ versus $\overline{\beta^2}$ for all selected spectra. Figure adapted from Brenguier and Chaumat (1996)

Chapter 8

Summary and conclusions

The goal of this thesis is to answer the following question.

> *Can non-uniformity in the spatial distribution of the size and position of droplets and/or variable vertical velocity in a turbulent medium contribute to the broadening of the droplet size distribution ?*

To answer this question, we adopted a numerical approach to simulate the growth and trajectory of several tens of thousands of cloud droplets in an environment whose properties vary from droplet to droplet. Based on a review of turbulence in cumulus clouds (Chapter 2) and a scale analysis of condensational growth of cloud droplets (Chapter 3), we demonstrated that the time and spatial scales related to the modification of the scalar fields by turbulence and the growth of the cloud droplets by diffusion of water vapor are sufficiently different. This scale separation permits us to parameterize the diffusional growth of the cloud droplets as a function of their ambient conditions (temperature and water vapor mixing ratio at a distance $\gg 20R$). Using a grid length of $\approx 1mm$ and droplet concentrations of $\approx 50cm^{-3}$, we designed experiments which, on the average, contains only one droplet in every 10 grid cells.

Under such a condition, the values of the temperature and water vapor mixing ratio in each grid cell represent the *microscopic* ambient conditions within which an individual droplet grows. Furthermore, the grid length chosen allows us to perform direct numerical simulations(DNS) of turbulent flow at low to moderate eddy dissipation rates which are typical to adiabatic cores of convective clouds. This detailed approach is termed the *microscopic* model. Results from this model are compared to the results from the *macroscopic* model which corresponds to a simple Lagrangian parcel experiment in which all droplets are exposed to the same supersaturation.

Our investigation begins with a series of simulations with no turbulent flow in Chapter 6. The focus of this chapter was to test the sensitivity of the *microscopic* results to the spatial distribution of the droplets as well as to various initial size distributions. We found that the random distribution of the position of droplets creates significant supersaturation perturbations with typical dispersions ($100. \times \sigma(S')/S_M$) of $\approx 3\%$. Whether the supersaturation perturbations result in an increase in the width of the *microscopic* size distribution relative to the *macroscopic* one depends on the width of the initial size spectrum.

In the *microscopic* approach we found a negative correlation between the perturbation degree of growth and the initial squared radius. Contrary to the *macroscopic* approach, the *microscopic* approach captures the fact that the release of the latent heat (or decrease in water vapor mixing ratio) is proportional to the size of the droplet, a drop which is smaller (larger) than the average size would develop in an immediate environment which is colder (warmer) and moister (drier) than that in the *macroscopic* approach. For very wide initial size distributions, we showed that this effect can lead to a narrowing of the *microscopic* size distribution relative to the *macroscopic* spectrum.

To examine the effect of the *microscopic* approach on individual droplets, we examined the distribution of ${}^tR - {}^tR_M$ at the end of the experiments ($200s$). The

standard deviation of this distribution is typically $\approx .15\mu m$ while the extrema are typically $\approx .8$ and $-.5\mu m$. These extrema represent upper bounds which delineate how much larger the largest droplet of the size distribution and how much smaller the smallest droplet of the size distribution can vary from the *microscopic* to the *macroscopic* approach. When the initial size distribution is not monodispersed, these upper bounds will decrease on account of the negative correlation discussed above.

In the no turbulence scenario, we performed an experiment including the sedimentation of the droplets at their terminal fall speeds. The initial size distribution for this experiment was uniform from 5 to $15\mu m$. The effect of the sedimentation of the droplets can be summarized as follows:

i)The droplets now grow in a variable environment where growth varies rapidly between favorable (positive perturbation) and unfavorable (negative perturbation) conditions. The average time that a droplet stays in similar conditions can be estimated from the decorrelation time, calculated from the autocorrelation coefficient of the supersaturation perturbation as a function of lag time. In the absence of sedimentation (and turbulence) the decorrelation time is very long (minutes), whereas when the droplets sediment this time is reduced to a few seconds.

ii) When droplets fall, their configuration changes. Consequently, regions void of droplets and regions of high droplet concentration, where significant perturbations in the scalar fields can develop, will exist only for a short time. This has the effect of decreasing the standard deviation of the perturbation scalar fields and subsequently the standard deviation (or dispersion) of the supersaturation perturbation distribution also decreases (by 35 to 50%).

As a result of these effects the dispersion of the degree of growth is significantly reduced from .025 to .008 (reduction of $\approx 65\%$).

We also compared our numerical results to the analytic estimates obtained by Srivastava (1989). The results are in qualitative agreement. However, the analytical

estimates over-predict the broadening potential of the *microscopic* approach.

Turbulence is introduced in Chapter 7. Three turbulent flow configurations, with increasing eddy dissipation rate are first described. They are well resolved low Reynolds number flows representing dissipation range dynamics, and, particularly for *flowC*, exhibit complex and intermittent behavior expected in turbulent flows.

An additional effect occurs when particles move in a turbulent fluid. As discussed in Section 2.4.2, particles tend to diverge from regions of high vorticity and converge preferentially in regions of low vorticity as a result of their inertia. Thus their spatial distribution is not random and does not follow a Poisson distribution. As a first step, we examined the inertia effect in the simpler situation of non-growing, sedimenting or non-sedimenting droplets. We initialized the experiments using four different size distributions, three of which were monodispersed spectra at 10, 15 and $20\mu m$ in radius and the fourth was a uniform size distribution from 10 to $20\mu m$ in radius. Three turbulent flows with eddy dissipation rates of 1.9, 14 and $161 cm^2 s^{-3}$ were used. The corresponding Stokes number vary between .004 and .16. We calculated the clustering index (see Appendix A), which represents the degree of deviation in the spatial distribution of the droplets from Poisson statistics, as a function of sampling length scale. We also examined the link between the vorticity of the fluid and the concentration of the droplets by calculating the correlation between the magnitude of the vorticity and the number of droplets($r(|\omega|, n)$), again as a function of sampling length scale.

It was found that in all experiments in which the droplets are not allowed to sediment there is a clear increase of the clustering index and the magnitude of the correlation between vorticity and number density as a function of increasing Stokes number for all sampling length scales. The lowest Stokes number at which some preferential concentration was found is .017. The corresponding radius of the droplets for preferential concentration turns out to be approximately $20\mu m$ in *flowA*, $12\mu m$ in *flowB* and $7\mu m$ in *flowC*. At Stokes number higher than .017 we found that the

deviation of the spatial distribution of the droplets from Poisson is statistically significant. The magnitude of the vorticity also correlates well with the concentration of droplets. The largest deviation from Poisson occurs in the case of $20\mu m$ droplets in *flowC*. The Stokes number for this case is .16, the highest Stokes number achieved in all our experiments.

The situation becomes more complicated when sedimentation of the droplets is allowed. In general, the sedimentation of droplets has the effect of reducing the clustering index and the correlation between the magnitude of vorticity and number density. However, these quantities are still statistically significant unless they were already borderline in the no sedimentation experiments. We also found that the difference between the results for droplets of different sizes is reduced and sometimes eliminated. Furthermore, we found that the impact of sedimentation on the spatial distribution of droplets or on the correlation between the magnitude of vorticity and number density of droplets decreases as the level of turbulence increases.

The reason for the complicated behavior when sedimentation is included is attributable to the fact that droplets acquire a mean velocity relative to the flow and the time of interaction between a droplet and an eddy is reduced. Sedimentation therefore introduces a new timescale which is the time it takes for a droplet to cross an eddy due to its terminal velocity. By calculating the ratio τ_V/τ_η, where τ_V is the time it takes for a droplet to cross an eddy of size equal to the Kolmogorov length scale and τ_η is the eddy turnover time for such eddies, it was found that an increase (decrease) in this ratio indicates a decreasing (increasing) importance of sedimentation.

We then performed a series of experiments with the full *microscopic* model including condensational growth of droplets. Using an initial monodispersed $15\mu m$ size distribution, we examined the spectral changes caused by the *microscopic* approach by including or excluding one of the following processes: i) sedimentation of droplets,

ii) clustering through the inertial term in the equation of motion of the droplets and iii) local cooling term due to turbulent vertical velocity for a given flow. We found that:

- $\sigma(R)$ and $\sigma(\beta'^2)/\beta_M^2$ increase if sedimentation is neglected.
- $\sigma(R)$ and $\sigma(\beta'^2)/\beta_M^2$ increase if clustering is present.
- $\sigma(R)$ and $\sigma(\beta'^2)/\beta_M^2$ increase if the cooling term is present.

However, when only the intensity of turbulence is varied but all effects are included, we found:

- $\sigma(R)$ decreases as a function of increasing ϵ
- $\sigma(\beta'^2)/\beta_M^2$ decreases as a function of increasing ϵ
- $\sigma(S')/S_M$ increases as a function of increasing ϵ
- $\sigma(T')$ increases as a function of increasing ϵ
- $\sigma(q_v')$ slightly increases as a function of increasing ϵ
- the decorrelation time of the supersaturation perturbation, averaged over 2000 randomly chosen droplets, decreases as a function of increasing ϵ

We interpreted the above results as a consequence of the decrease in decorrelation time and an increase in preferential concentration as the level of turbulence increases.

The full runs with turbulence were also compared with another run with no turbulence but otherwise identical initial conditions (N06 in Chapter 6). We concluded that the presence of the turbulent flow significantly decreases the dispersion of the instantaneous distribution of supersaturation perturbation $\sigma(S')/S_M$ (through similar decreases in $\sigma(T')$ and $\sigma(q_v')$. The reduction is even more significant in terms of the

dispersion of the degree of growth, $\sigma(\beta'^2)/\beta_M^2$. In the absence of turbulence and sedimentation these two dispersions are almost equal in magnitude, while in the presence of turbulence and/or sedimentation $\sigma(\beta'^2)/\beta_M^2$ is significantly smaller than $\sigma(S')/S_M$. The two inferences made earlier concerning the effect of sedimentation of droplets on the no turbulence results also apply when turbulence is present and the droplet configuration constantly changes. Furthermore, the difference between the dispersions $\sigma(S')/S_M$ and $\sigma(\beta'^2)/\beta_M^2$ increases as the intensity of turbulence increases. This is consistent with the decrease in decorrelation time of the supersaturation perturbation as the intensity of turbulence increases.

Our final task was to compare the values of $\sigma(\beta'^2)/\beta_M^2$ obtained from the numerical experiments in Chapters 6 and 7 to those inferred from observations in adiabatic cloud cores by Brenguier and Chaumat (1996). They found that the broadening of the spectra is proportional to the average degree of growth and that a broadening of $\frac{\sigma(\beta'^2)}{\beta_M^2} \times 100. \approx 21\%$ is a minimum. Referring to Table 7.5 we see that the minimal dispersion observed is much greater than the dispersions we found when turbulence and sedimentation are present. Referring to Table 6.2 we see that in the most favorable and perhaps unrealistic experimental conditions of no flow and no sedimentation the dispersion obtained is of the same order of magnitude but still much smaller than the observed minimal dispersion.

Based on the results obtained in this thesis, we now answer the central question posed in the following way:

> *The microscopic approach, which takes into account non-uniformity in the spatial distribution of the size and position of droplets and variable vertical velocity in a turbulent medium, does not lead to a broadening of the droplet size distribution. However, in the absence of sedimentation of the droplets and turbulence, the microscopic approach can lead to non-negligible broadening of the droplet size spectrum.*

Appendix A

A.1 $V({}^tR_M^2) = V({}^0R^2)$

From equation 5.8 we can easily derive the following equations:

$$\begin{aligned} \overline{{}^tR_M^2}^2 &= \overline{{}^0R^2}^2 + 2\,\overline{{}^0R^2}\,\beta_M^2 + \beta_M^4 \\ \overline{{}^tR_M^4} &= \overline{{}^0R^4} + 2\,\overline{{}^0R^2}\,\beta_M^2 + \beta_M^4. \end{aligned}$$

Using these two equations in the definition of variance, $V({}^tR_M^2) = \overline{{}^tR_M^4} - \overline{{}^tR_M^2}^2$, leads to the equality $V({}^tR_M^2) = V({}^0R^2)$.

A.2 $cov(\beta'^2, {}^tR_M^2) = cov(\beta'^2, {}^0R^2)$

By definition we have $cov(\beta'^2, {}^tR_M^2) = \overline{\beta'^2\,{}^tR_M^2} - \overline{\beta'^2}\,\overline{{}^tR_M^2}$. Replacing ${}^tR_M^2$ by its definition from equation 5.8 and simplifying we get:

$$\begin{aligned} cov(\beta'^2, {}^tR_M^2) &= \overline{\beta'^2({}^tR^2 + \beta_M^2)} - \overline{\beta'^2}(\overline{{}^0R^2} + \beta_M^2) \\ &= \overline{\beta'^2\,{}^0R^2 + \beta'^2\beta_M^2} - \overline{\beta'^2}\,\overline{{}^0R^2} - \overline{\beta'^2}\,\beta_M^2 \\ &= \overline{\beta'^2\,{}^0R^2} - \overline{\beta'^2}\,\overline{{}^0R^2} \\ &= cov(\beta'^2, {}^0R^2) \end{aligned}$$

A.3 The Poisson distribution, its moments, its estimators and how to quantify deviation from

In situations where the effect of the inertia of droplets on their spatial distribution is considered negligible, the probability of finding a droplet at a certain position is the same as finding the droplet at any other position. In that situation the spatial distribution of the droplets can be approximated by the Poisson distribution. Knowing the average concentration of droplets C, in a sampling volume v we expect to find a number of droplets given by $\lambda = Cv$. The probability of actually counting n droplets in that sample volume is given by the Poisson distribution:

$$P(n;\lambda) = \frac{exp^{-\lambda}\lambda^n}{n!} \tag{A.1}$$

For an infinite number of sampling volumes, the moments of the distribution of n are given by:

$$< n >= \lambda \tag{A.2}$$

$$V(n) = \lambda$$

$$skewness = \frac{1}{\sigma(n)^3} < (n-\lambda)^3 >= \lambda^{-1/2}$$

$$kurtosis = \frac{1}{\sigma(n)^4} < (n-\lambda)^4 > -3. = \lambda^{-1}$$

When the number of sampling volumes is finite, the measured moments(called estimators) of the distribution of n will deviate from their theoretical values. Only the average $< n >$ is exact since the total number of droplets is a fixed parameter. It is possible to estimate by how much the measured variance can be expected to deviate from the true value by calculating the variance of the estimator which is

given by (Barlow, page 78):

$$V(\widehat{V(n)}) = \frac{2\lambda^2}{N}.$$

where $\widehat{V(n)}$ is the measured variance and N is the number of sampling volumes. Note that this equation is only valid when λ is not too small and N is large enough. Therefore, we can expect the measured variance to deviate from the true variance by $\approx \pm\lambda\sqrt{2/N}$ for 68% of such measurements.

One simple method to quantify deviations from the Poisson distribution is to calculate the following ratio:

$$\frac{\widehat{V(n)}}{V(n)} - 1 = \frac{\widehat{V(n)}}{\lambda} - 1. \qquad (A.3)$$

This ratio is called the relative variance or the clustering index. To determine if the spatial distribution of droplets does indeed respect Poisson statistics, this ratio is calculated for various sampling volumes (corresponding to various λ's). If, for any λ, the ratio significantly departs from $\pm\sqrt{2/N}$, we can conclude that the spatial distribution of droplets does not follow a Poisson distribution.

Bibliography

ASSELIN, R. A. (1972). Frequency filter for time integrations. *Monthly Weather Review*, 100:487–490.

BAKER, B. A. (1992). Turbulent entrainment and mixing in clouds: A new observational approach. *Journal of the Atmospheric Sciences*, 49:387–404.

BARLOW, R. J. (1989). *Statistics: A guide to the use of statistical methods in the physical sciences*. John Wiley & Sons.

BARTELLO, P., METAIS, O., AND LESIEUR, M. (1994). Coherent structures in rotating three–dimensional turbulence. *J. Fluid Mech.*, 273:1–29.

BORRMANN, S., JAENICKE, R., AND NEUMANN, P. (1993). On spatial distributions and inter-droplet distances in stratus clouds with in-line holography. *J. Rech. Atmos.*, 29:229–245.

BRENGUIER, J.-L. (1991). Parameterization of the condensation process: A theoretical approach. *Journal of the Atmospheric Sciences*, 48:264–282.

BRENGUIER, J.-L., BOURRIANNE, T., COELHO, A. A., ISBERT, J., PEYTAVI, R., TREVARIN, D., AND WECHSLER, P. (1998). Improvements of the droplet size

distribution measurements with the fast-fssp. *Journal of Atmospheric and Ocean Technology*, 15(in press).

BRENGUIER, J.-L. AND CHAUMAT, L. (1996). Condensational droplet growth in cumulus clouds. In *Proc. of the 12th Int. Conference on Clouds and Precipitation*, pages 57–60, Zurich,Switzerland.

CARSTENS, J. C., WILLIAMS, A., AND ZUNG, J. T. (1970). Theory of droplet growth in clouds: Ii. diffusional interaction between two growing droplets. *Journal of the Atmospheric Sciences*, 27:798–803.

CHAMPAGNE, F. H., FRIEHE, C. A., LARUE, J. C., AND WYNGAARD, J. C. (1977). Flux measurements, flux estimation techniques, and fine-scale turbulence measurements in the unstable surface layer over land. *Journal of the Atmospheric Sciences*, 34:515–530.

CHEN, J.-P. (1994). Predictions of saturation ratio for cloud microphysical models. *Journal of the Atmospheric Sciences*, 51:1332–1338.

CLARK, T. L. (1973). Numerical modeling of the dynamics and microphysics of warm cumulus convection. *Journal of the Atmospheric Sciences*, 30:857–878.

COOPER, W. A. (1989). Effects of variable droplet growth histories on droplet size distributions. part i: Theory. *Journal of the Atmospheric Sciences*, 46:1301–1311.

COOPER, W. A. (1991). Research in cloud and precipitation physics: Review of the u.s. theoretical and observational studies. *Rev. of Geophys., suppl.*, pages 69–79.

EATON, J. K. AND R., F. J. (1994). Preferential concentration of particles by turbulence. *Int. J. Multiphase Flow*, 20:169–209.

ELGHOBASHI, S. AND TRUESDELL, G. C. (1993). On the two-way interaction between homogeneous turbulence and dispersed solid particles: I: Turbulence modification. *Phys. Fluids A*, 5:1790–1801.

ESWARAN, V. AND POPE, S. B. (1988). An examination of forcing in direct numerical simulations of turbulence. *Computers & Fluids*, 16(3):257–278.

FESSLER, J. R., KULICK, J. D., AND EATON, J. K. (1994). Preferential concentration of heavy particles in a turbulent channel flow. *Phys. Fluids*, 6(11):3742–3749.

GAGETT, A. E., OSBORN, T. R., AND NASMYTH, T. W. (1984). Local isotropy and the decay of turbulence in a stratified fluid. *J. Fluid Mech.*, 144:231–280.

GAGNE, Y. (1987). Etude éxperimentale de l'intermittence et des singularités dans le plan complexe en turbulence développée. *Thèse de Doctorat d'Etat.*

GORE, R. A. AND CROWE, C. T. (1989). Effect of particle size on modulating turbulent intensity. *Int. J. Multiphase flow*, 15(2):279–285.

GRABOWSKI, W. W. AND CLARK, T. L. (1993). Cloud-environment interface instability. part ii: Extension to three spatial dimensions. *Journal of the Atmospheric Sciences*, 50:555–573.

HALL, W. D. (1980). A detailed microphysical model within a two-dimensional dynamic framework: Model description and preliminary results. *Journal of the Atmospheric Sciences*, 37:2486–2507.

HARDALUPAS, Y., TAYLOR, K. P., AND H., W. J. (1989). Velocity and particle-flux characteristics of turbulent particle laden jets. *Proc. R. Soc. London Ser. A*, 426:31–.

HESTRONI, G. (1989). Particle-turbulence interaction. *Int. J. Multiphase Flow*, 15:315–327.

JENSEN, J. B., AUSTIN, P. H., BAKER, M. B., AND BLYTH, A. M. (1985). Turbulent mixing, spectral evolution and dynamics in a warm cumulus cloud. *Journal of the Atmospheric Sciences*, 42:173–192.

KERR, R. M. (1985). Higher order derivative correlations and the alignment of small scale structures in isotropic numerical turbulence. *J. Fluid Mech.*, 153:31–58.

KHAIN, A. P. AND PINSKY, M. B. (1995). Drop inertia and its contribution to turbulent coalescence in convective clouds. part i: Drop fall in the flow with random horizontal velocity. *Journal of the Atmospheric Sciences*, 52:196–206.

KINZER, G. D. AND GUNN, R. (1951). The evaporation, temperature and thermal relaxation time of freely falling waterdrops. *J. of Meteorology*, 8(2):71–83.

KOLMOGOROV, A. N. (1941). The local structure of turbulence in incompressible viscous fluid for very large reynolds numbers. *Dokl. Akad. Nauk SSSR*, 30:301–305.

KOZIKOWSKA, A., HAMAN, K., AND SUPRONOWICZ, J. (1984). Preliminary results of an investigaton of the spatial distribution of fog droplets by a holographic method. *Quart. J. R. Met. Soc.*, 110:65–73.

LESIEUR, M. (1990). *Turbulence in Fluids*. Kluwer Academic Publishers, second edition.

MACPHERSON, J. I. (1979). A comparison of turbulent characteristics of cumulus clouds measured near yellowknife and thunder bay. *DME/NAE Quart. Bull.*, (1979(1)):38.

MACPHERSON, J. I. AND ISAAC, G. A. (1977). Turbulent characteristics of some canadian cumulus clouds. *J. Applied Meteor.*, 16:81–90.

MANTON, M. J. (1979). On the broadening of a droplet distribution by turbulence near cloud base. *Quart. J. R. Met. Soc.*, 105:899–914.

MAXEY, M. R. (1987). The gravitational settling of aerosol particles in homogeneous turbulence and random flow fields. *J. Fluid Mech.*, 174:441–464.

MAXEY, M. R. AND RILEY, J. J. (1983). Equation of motion for a small rigid sphere in a nonuniform flow. *Phys. Fluids*, 26(4):883–889.

MCLAUGHLIN, J. B. (1994). Numerical computation of particles-turbulence interaction. *Int. J. Multiphase Flow*, 20:211–232.

ORSZAG, S. A. (1971). Numerical simulation of incompressible flows within simple boundaries. i galerkin (spectral) representations. *Studies in applied mathematics*, 50:293–327.

PINSKY, M. B., KHAIN, A. P., AND LEVIN, Z. (1996). The effect of turbulence on the broadening of the droplet spectrum in clouds at the initial stage of their evolution. In *Proc. of the 12th Int. Conference on Clouds and Precipitation*, pages 45–48, Zurich,Switzerland.

POLITOVICH, M. K. (1993). A study of the broadening of droplet size distributions in cumuli. *Journal of the Atmospheric Sciences*, 50:2230–2244.

POLITOVICH, M. K. AND COOPER, W. A. (1988). Variability of the supersaturation in cumulus clouds. *Journal of the Atmospheric Sciences*, 45:1651–1664.

PRESS, W. H., FLANNERY, B. P., TEUKOLSKY, S. A., AND VETTERLING, W. T. (1986). *Numerical recipes*. Cambridge University press, first edition.

PRUPPACHER, H. R. AND KLETT, J. D. (1978). *Microphysics of clouds and precipitation*. D. Reidel.

RILEY, J. J., METCALFE, R. W., AND WEISSMAN, M. A. (1981). Direct numerical simulations of homogeneous turbulence in density stratified fluids. In WEST, B. J., editor, *Non linear properties of internal waves*, pages 79–112. La Jolla Institute.

ROBERT, A. J. (1966). The integration of a low order spectral form of the primitive meteorological equations. *J. Meteor. Soc. Japan*, 44:237–245.

ROGERS, R. R. AND YAU, M. K. (1989). *A short course in cloud physics*. Pergamon press, third edition.

SEDUNOV, Y. S. (1974). *Physics of the drop formation in the atmosphere*. John Wiley & Sons.

SHAW, R. A., READE, W. C., COLLINS, L. R., AND VERLINDE, J. (1998). Preferential concentration of clouds droplets by turbulence: effects on early evolution of cumulus cloud droplet spectra. *Journal of the Atmospheric Sciences*, (Accepted for publication).

SHE, Z.-S., JACKSON, E., AND ORSZAG, S. A. (1990). Intermittent vortex structures in homogeneous isotropic turbulence. *Nature*, 344:226–228.

SHE, Z.-S., JACKSON, E., AND ORSZAG, S. A. (1991). Structure and dynamics of homogeneous turbulence: models and simulations. *Proc. R. Soc. Lond. A*, 434:101–124.

SIGGIA, E. D. (1981). Numerical study of small scale intermittency in three-dimensional turbulence. *J. Fluid Mech.*, 107:375–406.

SQUIRES, K. D. AND EATON, J. K. (1990). Particle response and turbulence modification in isotropic turbulence. *Phys. Fluids A*, 2(7):1191–1203.

SQUIRES, K. D. AND EATON, J. K. (1991a). Preferential concentration of particles by turbulence. *Phys. Fluids A*, 3(5):1169–1178.

SQUIRES, K. D. AND EATON, J. K. (1991b). Measurements of particle dispersion obtained from direct numerical simulations of isotropic turbulence. *J. Fluid Mech.*, 226:1–35.

SRIVASTAVA, R. C. (1989). Growth of cloud droplets by condensation: A criticism of currently accepted theory and a new approach. *Journal of the Atmospheric Sciences*, 46:869–887.

STOCK, D. E. (1996). Particle dispersion in flowing gases. *ASME J. of Fluids Engineering*, 118:4–17.

SULLIVAN, N. P., MAHALINGAM, S., AND KERR, R. M. (1994). Deterministic forcing of homogeneous, isotropic turbulence. *Phys. Fluids*, 6(4):1612–1614.

UHLIG, E.-M., BORRMANN, S., AND JAENICKE, R. (1998). Inter-droplet distances of cloud droplets measured with the ground based holographic system hodar. *Tellus*, (Accepted for publication).

UNDERWOOD, E. E. (1970). *Quantitative Stereology*. Addison Wesley.

VINCENT, A. AND MENEGUZZI, M. (1991). The spatial structures and statistical properties of homogeneous turbulence. *J. Fluid Mech.*, 225:1–20.

WANG, L. P. AND MAXEY, M. R. (1993). Settling velocity and concentration distribution of heavy particles in homogeneous isotropic turbulence. *J. Fluid Mech.*, 256:27–68.

WARNER, J. (1969). The microstructure of cumulus cloud. part i: General features of the droplet spectrum. *Journal of the Atmospheric Sciences*, 26:1049–1059.

WATTS, R. G. AND FARHI, I. (1975). Relaxation times for stationary evaporating liquid droplets. *Journal of the Atmospheric Sciences*, 32:1864–1867.

WEIL, J. C., LAWSON, R. P., AND RODI, A. R. (1993). Relative dispersion of ice crystals in seeded cumuli. *J. Applied Meteor.*, 32:1055–1073.

YEUNG, P. K. AND POPE, S. B. (1988). An algorithm for tracking fluid particles in numerical simulations of homogeneous turbulence. *J. Comput. Phys.*, 79:373–416.